Innovative solutions and applications for polymer light-emitting diodes

Francesco Bausi

London Centre for Nanotechnology

and Department of Physics and Astronomy

University College London

Dissertation submitted for the degree of Doctor of Philosophy

August 2015

I, Francesco Bausi, confirm that the work presented in this thesis is my own. Where information has been derived from other sources and work which has formed part of jointly-authored publications has been used I confirm that this has been indicated in the thesis.

Acknowledgements

I wish first to thank my supervisor Professor Franco Cacialli for the support and guidance throughout all these years. I would also like to thank my secondary supervisor Professor Neal Skipper for the helpful discussions. My gratitude goes also to my collaborators without whose support this work would not have been possible, in particular Paul Haigh, Giulia Privitera, Andrea Schlierf, Giulia Tregnago, Giuseppe Paternó, Ludovica Intilla, Iannis Papakonstantinou, Francesco Bonaccorso, Matthias Schwab, Vincenzo Palermo and all the people involved in the GENIUS project. Finally, a big thanks goes to the members of the Organic Semiconductors and Nanostructures group for their help and friendly support during these years.

Abstract

This work focuses on the development of new technical solutions for polymer light-emitting diodes (PLEDs). Treatments were developed to use innovative materials, such as graphene and carbon nanotubes, as hole-transporting layers and surface modifiers on top of ITO. A processing treatment for the preparation of the polymeric emissive layer of PLEDs was also investigated which allowed the improvement of the on/off switching speed of the devices thus enabling their employment in novel applications for visible light communications.

Graphene-based transparent thin films obtained via the exfoliation of graphite in the liquid phase were produced with a view of using them as surface modifiers of indium tin oxide (ITO) or as transparent electrodes in organic optoelectronic devices. As-deposited films are relatively resistive, but the sheet resistance was decreased by up to three orders of magnitude by thermal treatment down to values of $\sim 10^5 \; \Omega/\square$. The films were also chemically doped via the physisorption of the electron-withdrawing molecule $(CF_3SO_2)_2NH$. This resulted in an increase of the work function by up to $0.5 \; eV$, to yield a value of $\sim 5.3 \; eV$ comparable to what can be achieved with poly(3,4-ethylene dioxythiophene):poly(styrene sulfonate) (PEDOT:PSS).

Thin films of liquid-phase exfoliated graphene and sorted single-walled

carbon nanotubes (SWNTs) were deposited on thin ITO layers ($\sim 100\ nm$). The work function values of these films measured in air using the Kelvin probe were compared with the work function values measured via electroabsorption when the film is inside a device and in contact with the emissive polymer of the device's active layer. The data shows that the latter appear to be 0.1/0.2 eV higher than those measured in air, whereas this difference is not present for ITO alone. This suggests a charge transfer at the interface of graphene films with the polymer layer.

Finally, the thermal processing of the active layer of PLEDs was reported to increase the on/off speed of encapsulated devices by more than double to reach a cut-off frequency of approximately 260 kHz. The underlying mechanism was investigated. Unexpectedly, the increased speed of the device corresponds to the formation of crystalline domains that decrease the thin-film transistor mobility. The data suggest suggests an increase in the charge injection inside the active layer via a trap-assisted injection mechanism. Thanks to such optimisation processing a maximum data rate up to 55 $Mbit/s$ can be envisaged by employing wavelength multiplexing with a high-performance artificial neural network (ANN) equalizer [1].

Contents

List of Figures

19

22

24

List of Abbreviations

AC	Alternate Coupling
AFG	Arbitrary Function Generator
AFM	Atomic Force Microscopy (Microscope)
CNT	Carbon Nanotubes
c.p.d.	Contact Potential Difference
CVD	Chemical Vapour Deposition
DC	Direct Coupling
DCB	Dichlorobenzene
DMF	Dimethylformammide
DOS	Density of States
EA	Electroabsorption
EBL	Electron-Blocking Layer
EL	Electroluminescence
EQE	External Quantum Efficiency
F8BT	Poly(9,9-dioctylfluorene-alt-benzothiadiazole)
FC	Franck-Condon
FLG	Few-Layer Graphene
FRET	Foster Resonance Energy Transfer
FWHM	Full Width Half Maximum
GO	Graphene Oxide
HOMO	Highest Occupied Molecular Orbital
HOPG	Highly Oriented Pyrolytic Graphite
IPA	Isopropanol

IQE	Internal Quantum Efficiency
ITO	Indium Tin Oxide
ITS	Intelligent Transport System
JLV	current density-luminance-voltage
KP	Kelvin Probe
LED	Light Emitting Diode
LPE	Liquid-Phase Exfoliated
LPF	Low-Pass Filter
LUMO	Lowest Unoccupied Molecular Orbital
MDMO:PPV	Poly[2-methoxy-5-(3,7-dimethyloctyloxy)-1,4-phenylenevinylene]
NIR	Near-Infrared
NMP	N-Methylpyrrolidone
NW	Nano Wires
OFET	Organic Field-Effect Transistor
OLED	Organic Light-Emitting Diode
OOK	On/Off Keying
OPD	Organic Photo Detector
PDI	Perylene diimide
PEDOT:PSS	Poly(3,4-ethylenedioxythiophene)-poly(styrenesulfonate)
PL	Photoluminescence

PLED   Polymer Light-Emitting Diode

PMMA   Poly(methyl methacrylate)

PPV   Poly(p-phenylene vinylene)

PTFE   Poly(tetrafluoroethylene)

PVD   Photovoltaic Device

RF   Radio Frequencies

rms   Root Mean Square

SCL   Space Charge Limited

SWCNT   Single-Walled Carbon Nanotubes

TCSPC   Time-Correlated Single Photon Counting

TFB   Poly(9,9-dioctyluorene-alt-N-(4-butylphenyl)diphenylamine)

TFSA   1,1,1 trifluoro-N-(trifluoromethyl)sulfonylmethanesulfonamide

TFT   Thin-Film Transistor

UV   Ultra Violet

vis   Visible

VLC   Visible Light Communication

WF   Work Function

XRD   X-ray Diffraction (Diffractometry)

Introduction

Polymer light-emitting diodes (PLEDs) are one of the most promising technologies for novel applications in optoelectronic devices. Since 1989, when, at the Cavendish Laboratories in Cambridge (UK), high efficiency PLEDs were demonstrated for the first time such devices have been intensively investigated and progressively optimised[8]. A vast range of new electroluminescent polymers have been obtained via the development of tailored organic synthesis approaches. On the other hand, the device structure has been improved in terms of the energy level matching between the different layers with the introduction of polymeric interlayers, via electrodes engineering and in terms of light out coupling with the accurate design of the optical path for the emitted light.

Lower production costs, large areas, lightweight robust devices, increased colour contrast, flexible devices are among the main strengths of PLEDs. The most promising applications are both as a new display technology thanks to a higher color contrast, a lower consumption and a larger viewing angle or in the field of innovative lighting devices such as large area light emitting tiles, wearable flexible lights and printable LEDs to give just a few examples.

This work focuses on the development of new technical solutions for PLEDs. The use of innovative materials is explored, such as graphene or

carbon nanotubes for the preparation transparent hole-transporting layers. Graphene layers could be used as surface modifiers on top the transparent electrode made of indium tin oxide (ITO) to reduce the acidic degradation caused by PEDOT:PSS.

In chapter 2 graphene-based transparent films are used as indium tin oxide (ITO) modifiers for application in optoelectronic devices. A thermal annealing treatment of the films to increase their conductivity is described and a chemical processing to tune their work function. In particular the work focuses on graphene-based films obtained via deposition from liquid dispersions. This approach for the production of graphene films still presents some limitations, particularly in terms of electrical conductivity, but is a very promising as an economic and easily scalable method of graphene film production. The work function of the films can be conveniently tuned via chemical surface doping via the deposition of an electron-withdrawing molecule.

Chapter 3 investigates the variation of the work function of graphene films and single-walled carbon nanotubes (SWNTs) films upon the interaction with the electroluminescent polymer poly[(9,9-di-n-octylfluorenyl-2,7-diyl)-alt-(benzo[2,1,3]thiadiazol-4,8-diyl)] (F8BT). The formation of an interface between the graphene films or the CNT films and the conjugated polymer film results in an increase of the work function of the carbon-based film. This effect is not present at the interface between bare ITO and the luminescent polymer. To the best of our knowledge, this effect is not even reported at the interface between PEDOT:PSS and F8BT. This result is of particular interest for the use of graphene and SWNT based films as transparent hole-injection layer in optoelectronic devices.

Chapter 4 reports on an innovative application of PLEDs as trasmitters in visible light communication technology (VLC). VLC is a communication technology that employs radiation in the visible range opposed to the commonly used radio frequencies. This approach has the advantage of increasing the available frequencies for use in communications (bandwidth) by using screens, monitors or illumination sources as signal transmitting devices. The use of PLEDs in VLC have been demonstrated for the first time in several recent publications [9, 10, 11, 12, 13, 14, 15, 16]. A data rate up to 20 Mb/s has been obtained and the possibility for 55 Mb/s using a wavelength-multiplexed system with a high-performance artificial neural network (ANN) equalizer has been described [1]. This work will demonstrate and investigate a processing treatment to increase the on/off switch speed of the devices by more than twice from $\sim 116~kHz$ up to $\sim 260~kHz$.

Chapter 1

Organic electronics

This chapter gives a brief introduction on the physics of organic semiconductors, and in particular of polymer semiconductors. These materials have now started to be employed in high-end commercial products mainly flatscreen TVs and monitors. Polymer semiconductors have the potential to revolutionise the world of opto-electronic devices thanks to their low-cost, wide colour tunability, high colour contrast, flexibility and the ease of processing over large areas. Here the structure and functioning of polymer light-emitting diodes (PLEDs) are also described. In the end of this chapter the main physical properties of graphene are presented: the single-atom thin material entirely based on carbon atoms which has been obtained and characterised for the first time by Novoselov and Geim in 2004. It has revealed to be the first of a whole new class of bi-dimensional materials whose peculiar characteristics are particularly appealing for innovative applications in the field of organic electronics and optoelectronics.

1.1 Organic semiconductors

It is only in the last half of the twentieth century that a semiconductor behaviour was demonstrated for certain types of organic small molecules and polymers. In 1955, electroluminescence from organic materials was observed by André Bernanose [17]. Pope and Kallmann at New York University in 1960 demonstrated the ohmic dark-injection of holes inside a crystal of anthracene, setting the basis for organic semiconductor devices [18, 19]. In 1962, then, Pope and collegues observed electroluminescence from anthracene single crystals using silver paste electrodes and applying voltages of the order of 400 V [20].

In 1963 Bolto, McNeill and Weiss measured the conductivity of polypyrrole polymerised at different temperatures and explained it as due to a semiconductor character of the molecule. Both n- and p-doping were also obtained adding electron donating or electron accepting groups such as iodine and ethylene to form charge-transfer complexes [21]. In 1965 Pope and collegues described the electroluminescence in anthracene as due to the recombination of exciton at an energy lower than the band gap [22].

In 1965 Helfrich and Schneider obtained electroluminescence from anthracene single crystals via injection of both holes and electrons, only hole injection had been obtained until then. They used liquid anode and cathode electrodes made of solutions of positive and negative anthracene ions respectively [23].

Electroluminescence from a non-conjugated (namely PVK, or polyvinylcarbazole) polymer films was observed for the first time by Roger Partridge at the National Physical Laboratory (UK) who filed a patent in 1975 [24].

The poor results were probably due to the relatively small conductivity of PVK. It was in 1977 that Shirakawa, MacDiarmid and Heeger reported the synthesis of polyacetylene with the addition of halogens vapour. Such doping increased the polymer conductivity by over seven orders of magnitude up to about $10^5\ S\ m^{-1}$, where silver is $10^8\ S\ m^{-1}$ and teflon has a conductivity of $10^{-16}\ S\ m^{-1}$ [25].

In 1987 Tang and Van Slyke at Eastman Kodak produced the first organic light-emitting diode (OLED) with an innovative multi-layer structure, reporting an efficiency of 1%. With their work, they started the era of OLEDs and organics optoelectronic devices [26]. In the same year, for the first time, a polymer semiconductor, polythiophene, was used by Koezuka as the active layer in field-effect transistors, in what is now called an OFET [27].

In 1989 Jeremy Burroughes, Donal Bradley and Richard Friend at the Cavendish Laboratory in Cambridge produced the first high-efficiency green polymer light-emitting diode (PLED) using a thin film (100 nm) of poly(p-phenylene vinylene) (PPV) [8]. In the 2000 the Nobel Prize in Chemistry was awarded to Alan J. Heeger, Alan G. MacDiarmid, and Hideki Shirakawa for their work on conductive polymers [28].

In the last years, the number of companies that develop and sell commercial organic opto-electronic devices is growing at fast pace. Organic semiconductors can be designed via chemical synthesis to tune their electronic and optical characteristics. Small-molecules organic light-emitting diodes (OLEDs) are already used in a large range of innovative commercial products mainly for displays, screens and lighting. Polymer light-emitting diodes products are also developing rapidly thanks to the appealing possibility of

processing the semiconductor materials using printing methods from liquid polymer solutions.

1.1.1   Electronic properties

Conjugated systems

The electronic properties of organic semiconductor molecules arise from the particular disposition of the carbon atoms. Carbon's electronic structure is $1s^2 2s^2 2p^2$ meaning that, in the atomic valence shell ($n = 2$), four electrons are shared between four orbitals: one s orbital and three p orbitals.

In particular, the chemistry of carbon is based on the hybridisation of the valence shell atomic orbitals. A linear combination of the $2s$ orbital and the $2p$ orbitals gives rise to an equal number of new hybridised orbitals. Depending on the number of p orbitals involved, three different hybridisation geometries are possible: sp^1, sp^2 and sp^3.

The optical and electrical properties of organic molecules are mainly due to sp^2 hybridised carbon atoms [29]. The resulting three orbitals lie on a plane and are oriented at 120° to each other (see Fig. 1.1). The one p orbital that is not involved in the hybridisation is conventionally referred to as the p_z orbital.

The hybridisation can explain the bonding geometry of carbon atoms in organic molecules. Two sp^2 carbons can form a covalent bond by overlapping their hybridised orbitals and thus forming two new orbitals: one σ-orbital and one σ^*-orbital. Such orbitals are extended over the two carbon atoms and hence are called molecular orbitals. The σ-orbital is more stable than the two original atomic orbitals and therefore is called the bonding molecular

orbital. On the contrary, the σ^*-orbital is unstable as its energy is higher than the separated atoms and is called the anti-bonding molecular orbital.

Since only two electrons are involved in this process, they are both contained in the σ-orbital forming a stable single covalent bond. The two p_z orbitals on each atom lie now very close to each other and their overlap gives rise to two so called π-orbitals: one bonding (π) and one anti-bonding (π^*). The two p_z electrons are both contained in the lower energy π-orbital forming a stable double bond (see Fig. 1.2).

Electronic structure

Portions of organic molecules constituted by adjacent sp^2 carbon atoms are referred to as conjugated systems. The p_z electrons are delocalised on the whole system (see Fig. 1.3).

All the p_z orbitals interact to form delocalised π-type molecular orbitals that extend across the entire conjugated system. The p_z atomic orbitals involved in the conjugated system give rise to an equal number of molecular orbitals and, therefore, since every p_z orbital contains only one electron, in the fundamental state only half of the molecular π-orbitals are filled with electrons. In particular, in the fundamental electronic state, only the bonding molecular orbitals are filled. The resulting electronic structure is analogous to a semiconductor where, at $0\ K$, the valence band (bonding orbitals in this case) is full and the conduction band (anti-bonding orbital) is empty.

The so-called frontier orbitals are of particular interest for the chemical and physical properties of a conjugated molecule, i.e. the highest occupied molecular orbital (HOMO) and the lowest unoccupied molecular orbital

41
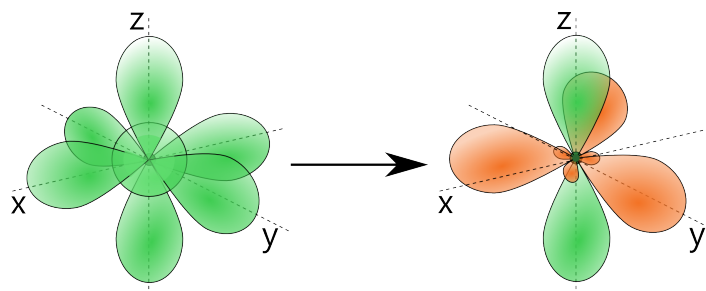
Figure 1.1: In the sp^2 hybridisation process one spherical $2s$ atomic orbital and two $2p$ orbitals in the valence shell of the carbon atom are combined to form three hybridised orbitals (orange). The sp^2 hybridised orbitals have cylindical axis that lie on a plane and point at 120° to each other. The one remaining non-hybridised $2p$ atomic orbital is conventionally referred to as the p_z orbital.
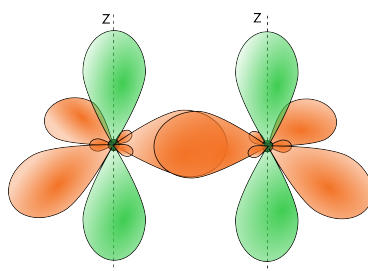
Figure 1.2: Two sp^2 hybridised carbon atoms can form double bond which is composed of a σ covalent bond by overlapping two sp^2 orbitals and a π covalent bond due to the interaction of the non-hybridised p_z orbitals.

(LUMO). For a typical conjugate polymer, the energy gap (E_g) between the HOMO and the LUMO is between $\sim 1.5 \; eV$ and $\sim 3.5 \; eV$. Such a gap falls in the range of the visible light hence polymer semiconductors can be used as active materials in opto-electronic devices. The E_g is inversely proportional
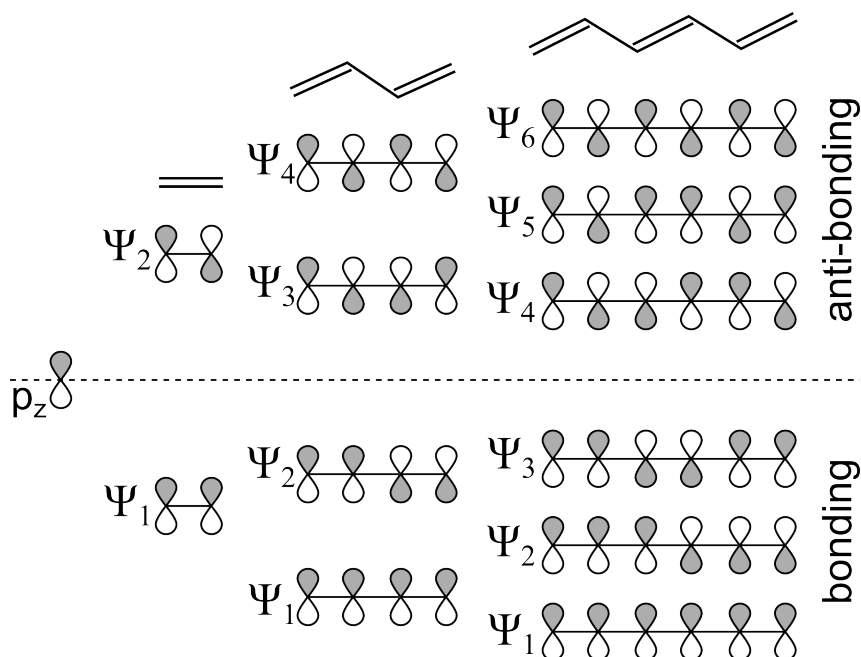
Figure 1.3: The p_z atomic orbitals of adjacent sp^2 hybridised carbon atoms can interact forming molecular orbitals that extend across the entire molecule or a large portion of it. The resulting number of molecular orbitals is equal to the number of the atomic orbitals that are involved. Depending on the relative phase of the constituting p_z orbitals a different number of nodes (i.e. points where the probability to find an electron is zero) are present in the molecular orbital. The energy of the orbital is proportional to the number of nodes.

to the size of the conjugated system.

Conjugated polymers have delocalised domains that can extend onto several monomeric units. Such domains are characterised by planar a structure due to the geometry of the sp^2 orbitals. Nevertheless, the strains due to molecular movements often tend to distort the planarity of larger conjugated

systems interrupting the delocalisation. This effect, together with the presence of localised defects on the molecules, reduces the size of the conjugation corresponding to a larger HOMO-LUMO gap thus affecting the optical and electrical properties [30].

Net charges

A net charge resulting by either charge injection or a chemical reaction, can be stabilised by delocalisation on a conjugated system. Organic molecules have a relatively low dielectric constant compared to inorganic compounds. Therefore, the excess of charge is poorly shielded and tends to polarise the surrounding atoms within a relatively long distance. This causes also a distortion of the molecular conformation to decrease the energy of the system resulting in the inter-band levels depicted in Fig. 1.4. The charge together

π* conduction band

positive
bipolaron

positive
polaron

exciton

negative
polaron

negative
bipolaron

π valence band
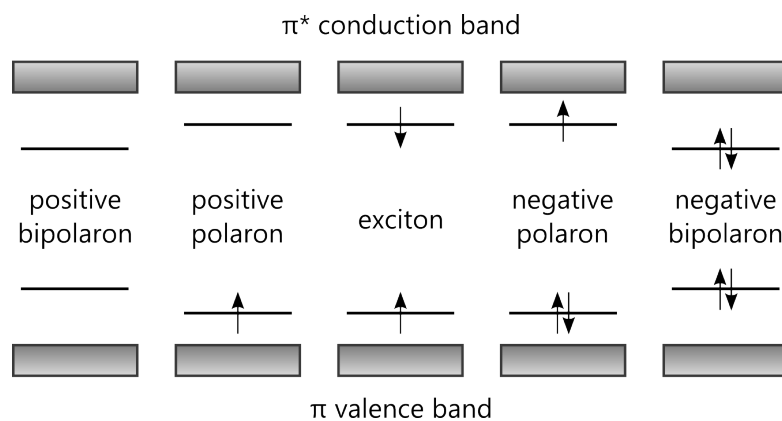
Figure 1.4: A net charge in organic semiconductors tends to polarise the surrounding molecules and distort their geometry to lower the energy of the system giving rise to inter-band states called polaron levels (adapted from [2]).

with the corresponding polarised surrounding can be described as a single

44

quasi-particle called *polaron*. Polarons can be either negative or positive. Bipolarons, instead, are formed when two polarons of the same sign interact via lattice deformation.

A net charge can be transferred between two different conjugated systems. The interaction between the donor and the acceptor leads to partial overlap of electronic molecular orbitals and the charge transport occurs via a hopping mechanism between localised states. This process is at the base of electrical conductivity in organic compounds [31]. This mechanism is much slower than the band-like transport mechanism in inorganic semiconductor crystals.

In a conjugated polymer matrix, opposite charged polarons can interact via a coulombic attraction and form a neutral quasi-particle called the Frenkel exciton. Such excitons can also form as the result of a photon absorption by a chromophore via the transition of an electron from the HOMO to the LUMO orbital.

Excitons are able to move between two different chromophores. In this process, the two chromophores are indicated as donor $D^\star$ and acceptor A, where the star index means that the molecules is in an excited state. The mechanism is referred to as energy transfer and it is generally described using the Föster model or the Dexter model. Both the models consider the transport as a non-radiative process, meaning that no emission and absorption of a photon is involved.

In the Föster model the energy transfer occurs via dipole-dipole resonance between the donor and the acceptor. The efficiency of this mechanism is proportional to the overlap between the emission spectrum of the donor and the absorption spectrum of the acceptor, is inversely proportional to the sixth

power of the distance between $D^\star$ and A and it is dependent on the relative orientation of the transition dipole moment vectors. This mechanism is also known as fluorescence resonance energy transfer (FRET) (see Fig. 1.5a). The Dexter energy transfer, instead, involves the exchange of two electrons
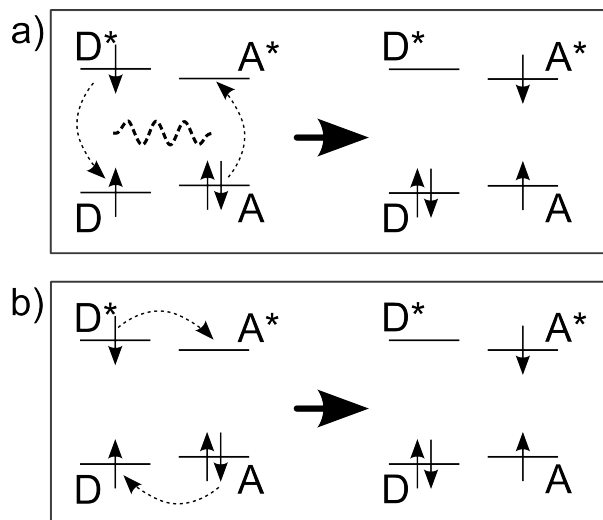
Figure 1.5: Föster resonance energy transfer mechanism (a) and Dexter energy transfer mechanism (b). The two models describe the diffusion of an excited state between adjacent molecules.

between the acceptor and the donor. In particular, an electron moves from the LUMO of the donor to the LUMO of the acceptor while another electron moves from the HOMO of the acceptor to the HOMO of the donor (see Fig. 1.5b). The efficiency of the process is proportional to the overlap between the wave functions of the orbitals involved and for this reason it decreases exponentially with the distance between the chromophores. It is also proportional to the spectral overlap between the emission of the donor and the absorption of the acceptor. Excited states can also be a transferred radiatively via emission of a photon from the donor and subsequent absorp-

tion by the acceptor. This process is proportional to the absorption-emission spectral overlap between the two species and, thus, it is not very efficient between molecules of the same species.

1.1.2 Interaction with light

Selection rules

Given the range of energies that separate the HOMO and the LUMO levels, organic semiconductors can interact with visible light via the absorption and emission of photons corresponding to transitions of electrons between the two energy levels. To understand the photo-physics of conjugated polymers the selection rules for the optical transitions need to be considered. Each quantum state is described by a wave function Ψ. The electromagnetic radiation interacts with the dipole moment of a chromophore and the transition probability $P_{\Psi' \to \Psi''}$ between an initial state Ψ' and a final state Ψ'' is proportional to the square of the transition dipole moment integral

$$P_{\Psi' \to \Psi''} \propto \langle \Psi'' | \vec{\mu} | \Psi' \rangle \tag{1.1}$$

where $\vec{\mu}$ is the transition dipole moment operator. In the Born-Oppenheimer approximation, the motion of electrons and that of the nuclei can be separated due to the large difference in their masses (the mass of a proton is about 1800 times larger than that of an electron). Consequently, both the

wave functions and the transition dipole moment can be factorised as follows

$$\langle \Psi_e'' \Psi_s'' \Psi_v'' | \vec{\mu}_e + \vec{\mu}_n | \Psi_e' \Psi_s' \Psi_v' \rangle =$$

$$\langle \Psi_e'' | \vec{\mu}_e | \Psi_e' \rangle \langle \Psi_s'' | \Psi_s' \rangle \langle \Psi_v'' | \Psi_v' \rangle + \langle \Psi_e'' | \Psi_e' \rangle \langle \Psi_s'' | \Psi_s' \rangle \langle \Psi_v'' | \vec{\mu}_n | \Psi_v' \rangle \qquad (1.2)$$

where Ψ_e is the electronic component, Ψ_v is the vibrational component and Ψ_s is the spin component of the wave function whereas $\vec{\mu}_e$ and $\vec{\mu}_n$ are the transition dipole moments for the electrons and for the nuclei respectively. Given the orthonormality of the electronic wave functions Ψ_e' and Ψ_e'' then $\langle \Psi_e'' | \Psi_e' \rangle = 0$ and hence the second term of the addition is zero. The probability of the transition from Ψ_e' to Ψ_e'' can be written as

$$\langle \Psi'' | \vec{\mu} | \Psi' \rangle = \langle \Psi_e'' | \vec{\mu}_e | \Psi_e' \rangle \langle \Psi_s'' | \Psi_s' \rangle \langle \Psi_v'' | \Psi_v' \rangle \qquad (1.3)$$

The equation 1.3 contains the conditions on the symmetry of the wave functions for an optical transition to occur between the two states. The first term is the electronic orbital selection rule and it is based exclusively on the symmetry of the two orbitals. The second term is the spin selection rule: electrons are characterised by two spin states $m_s = +1/2$ and $m_s = -1/2$ thus the probability of a transition is different from zero only if the spin does not change (conservation of spin). In general, spin forbidden transitions have little probability but can be normally observed in systems containing a heavy atom thanks to spin-orbit coupling. The last term in 1.3 is known as the Franck-Condon (FC) factor and sets a condition on the shape of vibrational wave functions. The transition probability is proportional to the squared overlap between the initial and the final wave functions. The FC integral

can assume a whole range of values as the two wave functions belong to different electronic states and the orthonormality condition does not apply.

Frank-Condon principle

Optical transitions such as absorption and emission involve the motion of an electron between two molecular orbitals and, according to the Born-Oppenheimer approximation, are much faster processes than the molecular vibrations which, instead, involve the motion the nuclei. The characteristic transition times are in the order of $10^{-15}/10^{-16}s$ for absorption and of $10^{-13}/10^{-14}s$ for emission. The Franck-Condon principle states that, since nuclei can be considered at rest during a transition, the probability of such transition is proportional to the overlap between the two vibrational wave functions of the initial and the final states. The mechanism is illustrated in Fig. 1.6. where transitions between the ground electronic state and the first excited electronic states are reported in function of the nuclei displacement coordinate. According to the Franck-Condon principle, all optical transitions occur vertically in this representation, i.e. without any variation in the nuclear positions.

The Franck-Condon principle explains the shape of electronic bands in the absorption or emission spectra. The excited electronic state is usually characterised by a larger mean distance between the nuclei due to the fact that one electron occupies an anti-bonding molecular orbital. For this reason, the $0-0$ transition (vibrational ground level to vibrational ground level) both for absorption and for emission generally is not the most intense peak. It is interesting to note that absorption and fluorescence emission involve
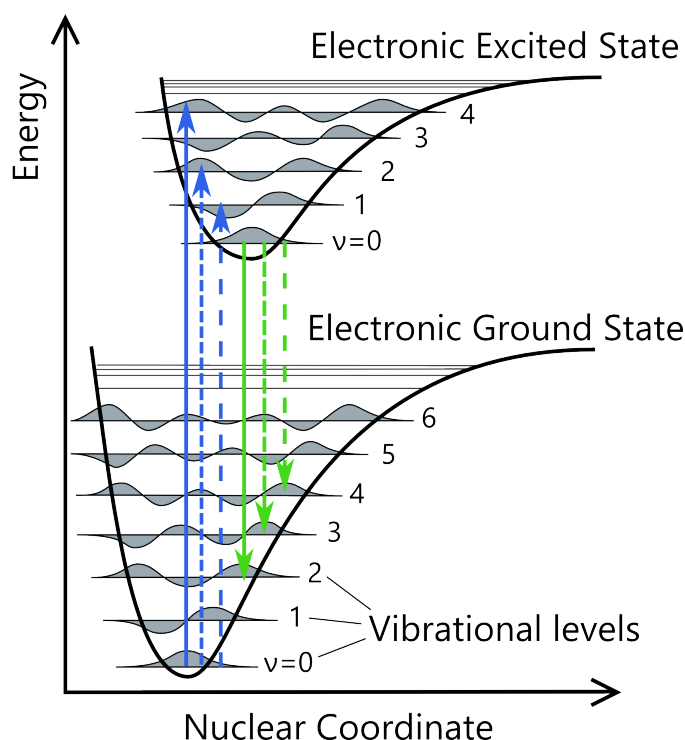
Figure 1.6: According to the Franck-Condon principle, optical transitions occur much faster than the motion of the nuclei of a molecule therefore are described by vertical lines in a diagram of the molecule energy versus the nuclear coordinates. For this reason the intensity of a peak for an electronic transition is proportional to the overlap between the two vibrational wave functions of the initial and final states.

the same energy levels hence, in principle, the two spectra are mirror images of each other. Nevertheless, some important differences are present. The absorption spectrum is usually featureless for conjugated polymers as the vibronic components are difficult to resolve. The reason is that, due to the intrinsic disorder of the polymer, a number of different chromophores con-

tribute to the absorption with a distribution of different sizes and hence with a distribution of slightly different energy for the electronic and vibrational levels. On the other hand, the emission spectra show more resolved vibronic peaks because, after the absorption, the excitons diffuse from shorter conjugated segments to longer conjugated segments with larger delocalisation and lower energy gap. This process is known as spectral diffusion. The result is that the fluorescence emission occurs from a narrower distribution of conjugation lengths and therefore the peaks are sharper and the spectral features more resolved. The energy difference between the $0 - 0$ transition peaks in the absorption and in the emission spectra is defined as the Stokes shift. This difference is caused by the conformational deformation of the molecules in the excited state to lower their energy before re-emitting a photon.

An exciton is constituted by two fermionic charged particles with spin quantum number $m_s = \pm 1/2$, thus the total spin of the system is $S = \Sigma m_s$ and it can either be 0, when the two spins are anti-parallel, or 1, when they are parallel. The spin multiplicity is defined as $2S + 1$ and it is respectively $2S + 1 = 1$ (singlet state) for anti-parallel spins or $2S + 1 = 3$ (triplet state) for parallel spins. The electronic ground state is a singlet state as all the electrons are paired. Excitons generated via absorption of a photon are mainly singlets given that the spin must be conserved in an optical transition. For the same reason, photon-generated excitons have a higher probability of decaying radiatively via emission of a photon to return to the single ground state. On the other hand, excitons generated by the mutual capture of polarons with opposite charge can give rise to either singlets or triplets states. In fact, triplets are statistically three times as favourite as singlets due to

the difference in spin multiplicity.

The Jablonski diagram

An exciton is an unstable state that can decay releasing energy either via the emission of a photon or via non radiative transitions. The Jablonski diagram is useful to describe all the possible transitions between the electronic states of a molecule (see Fig. 1.7). The fundamental and excited
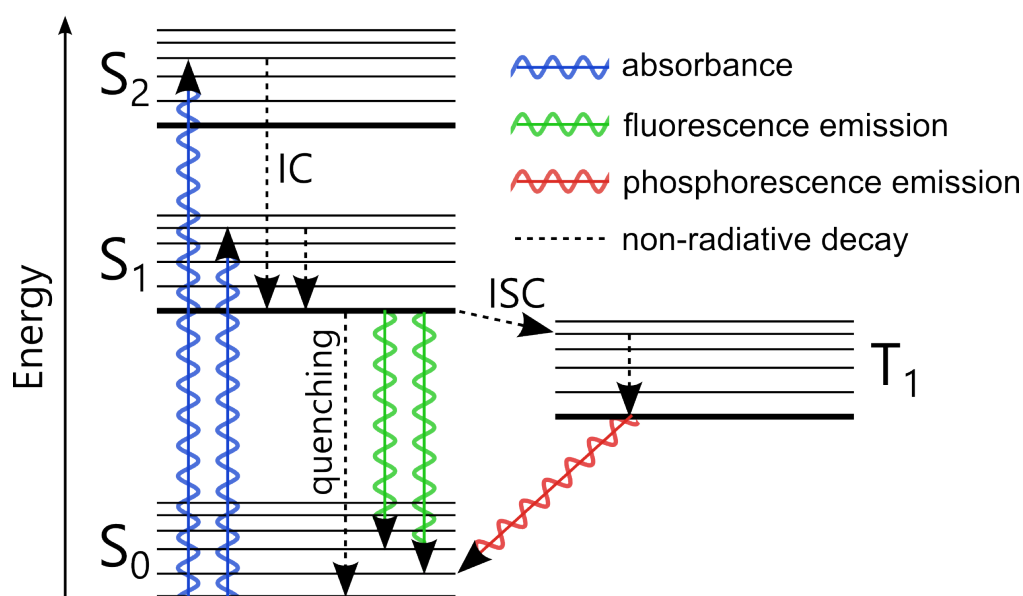
Figure 1.7: The Jablonski diagram is a summary of all the possible transitions between the electronic states of a molecule.

electronic singlet states and an excited triplet state are represented. A series of vibrational levels is also reported for each electronic state. For organic chromophores the vibrational quantum states are spaced by about $\sim 0.1\ eV$ At room temperature the thermal energy is $\sim 25\ meV$ and only the fundamental vibrational state is populated. Absorption of light occurs when the

chromophore is hit by a photon with an energy equal to the gap between the lowest vibrational state in the fundamental electronic state and a vibrational level in one of the excited electronic singlet states. The photon gets absorbed and the chromophore undergoes a vibronic (vibrational + electronic) transition in approximately $\sim 10^{-15}$ s. In $\sim 10^{-12}$ s such excited system decays via thermal relaxations (within an excited electronic state) and internal conversion (between two different excited electronic states) to the fundamental vibrational level of the excited electronic singlet state with the lowest energy, as described by the Kasha rule. At this point, the system decays to the fundamental electronic state either radiatively or non-radiatively depending on which of the two possible ways is faster. The radiative decays occurs generally after a time of few nanoseconds (photoluminescence life-time). In this process, called fluorescence, the system decays to one of the vibrational levels of the fundamental electronic state emitting a photon with an energy equal to the gap between the two quantum levels. Another possibility is the spin flipping of one of the unpaired electrons via a process called intersystem crossing. The system passes from the singlet excited state S_1 to the triplet excited state T_1. The energy of the triplet state is lower due to Hund's multiplicity rule. The radiative emission from T_1 to the fundamental single electronic state is a process called phosphorescence, it is a partially spin-forbidden transition that can occur only relatively slow with a life-time of $10^{-3}/10^2 s$.

Excited complexes

The interaction between two near chromophores can affect their physical and optical properties. It can be either an intra-molecular interaction, for adjacent chromophores along the polymer chain, or it can be an inter-molecular interaction, when the chromophores belong to different molecules. Interactions between chromophores on portions of a same polymer chain in a coiled conformation that are separated by a distance much longer than the size of the chromophores are also referred to as inter-molecular interactions.

The interaction at short distance between chromophores in the ground state is referred to as a ground-state aggregate. This interaction modifies the electronic structure of the two molecules giving rise to a modification in the absorption spectra. If the interaction occurs only when one of the chromophores is in the excited state the system is called an excimer (for excited dimer) or an exciplex (for excited complex) respectively when chromophores are of the same chemical species or when of different chemical species. Excimers and exciplexes are unstable species with a characteristic life-time.

The radiative emission from an excimer/exciplex state is characterised by a lower energy with respect to each of the two separated chromophores. Such spectral shift is proportional to the difference between the energy stabilisation of the coupled system and the repulsion of the molecules in their ground states.

1.2 Polymer light-emitting diodes

Polymer light-emitting diodes (PLEDs) are optoelectronic devices based on the electroluminescence from a thin film of a conjugated polymer. Such devices have a sandwich structure composed of a number of layers and have a relatively large photo-active area (up to several cm^2). Differently from organic LEDs (OLEDs), where the active layer is produced by thermal evaporation of small organic molecules in vacuum, in PLEDs conjugated polymers thin films are obtained via a number of deposition methods from liquid solutions.

1.2.1 Structure of a PLED

The emissive layer and other polymer inter-layers are sandwiched between the two electrodes: a transparent electrode and a back-reflecting metallic electrode. The most widespread material for the transparent electrode is indium tin oxide (ITO). It is a highly degenerate n-type semiconductor formed by a solid solution of indium oxide (In_2O_3) and tin oxide (SnO_2) as a dopant in a concentration of about 10% in mass. ITO has a wide band gap ($\sim 3.5 - 4.3 \ eV$) and that is why it shows a high transmission of visible and near-IR light [32]. The high level of doping to a carrier density of up to $\sim 10^{20} \ cm^{-3}$ confers the material a relatively low electrical resistivity of $\sim 2/4 \times 10^{-4} \ \Omega \ cm$ [33]. A $\sim 100 \ nm$ thick layer of ITO is deposited on a transparent inert substrate (glass) via a sputtering process. A hole-injecting layer of $\sim 30 \ nm$ is usually employed on top of ITO. The common hole-injection layer is constituted by the polymer poly(3,4-ethylenedioxythiophene) (PEDOT) doped with polystyrene sulfonate (PSS).

To avoid energy barriers for the charge carriers and thus improving the charge transport is important to match the energy levels at the interface between the different layers. The work function is the physical property of a surface that is most crucial in forming a good interface. The work function is defined as the energy required to extract an electron from the surface of a material and bring in to a point where it is still subject to the electrostatic potential of the surface.

In a metal, the occupation of the electronic levels is described by the Fermi-Dirac statistics

$$f(E) = \frac{1}{e^{(E-\mu)/kT} + 1} \tag{1.4}$$

where $f(E)$ is the probability of an electron to occupy the level at energy E, k is the Boltzman constant, T is the temperature in Kelvin and μ is the Fermi energy. At the thermodynamic equilibrium at 0 K the Fermi energy is equivalent (but opposite) to the work function whereas at $T > 0$ K the Fermi level has always a probability of occupation of 0.5.

PEDOT:PSS has a work function of ~ 5.2 eV which is close to the HOMO level of the typical fluorescent conjugated polymers used in PLEDs [34]. PEDOT:PSS is also characterised by a smoother surface compared to ITO and this is critical to increase the homogeneity of the device avoiding short circuit [35].

The emissive layer is usually deposited on top of PEDOT:PSS. In some cases an electron-blocking layer (EBL) is employed in between PEDOT:PSS and the emissive layer. The EBL has a large band gap with a HOMO close to PEDOT:PSS and a LUMO level higher than the LUMO of the emissive layer to create an energy barrier for electrons that are therefore confined

inside the active layer and not quenched on the anode. An example of EBL is the polymers poly(9,9'-dioctylfluorene-alt-N-(4-butylphenyl)-diphenylamine) (TFB).

A metallic cathode is deposited via thermal evaporation directly on top of the active layer. Metals such as calcium and lithium or compounds like molybdenum oxide (MoO_3) or lithium fluoride (LiF) have low enough work functions of $\sim 3\ eV$ to match very well the typical LUMO level of most of the conjugated fluorescent polymers. In many cases work function of the cathode is even lower compared to LUMO of the emissive polymer (as absolute value). In such situations, electrons transfer from the cathode to localised interface states of the polymer layer in a process known as the pinning of the work function that results in the equilibration between the work function of the cathode and the LUMO of the polymer [36, 37, 38, 39, 40].

1.2.2 Built-in voltage

When the device is assembled the Fermi levels of two metallic electrodes level up via charge transfer to localised states inside the polymer layer. A built-in voltage (V_{BI}) defined as

$$V_{BI} = (E_{anode} - E_{cathode})/e \tag{1.5}$$

where E_{anode} and $E_{cathode}$ are the work function of the anode and of the cathode respectively and e is the elementary charge. The V_{BI} is generated inside the device due to the difference between the work function of the anode and the cathode. Given the very low charge density and low level of doping by impurities, the resulting depletion region for polymer semiconductors is very large, of $\sim 1\ \mu m$, much larger than the thickness of the active layer.

As a consequence, the energy structure is characterised by rigid bands i.e. the electric field inside the polymer layer is constant. When a voltage of opposite sign is applied, the energy levels of the electrodes are shifted. When the applied voltage is equal to the V_{BI} a flat-band condition is reached where electric field inside the active layer is zero. When the voltage is further increased, charge can be injected from the electrodes and transported through the active layer.

1.2.3   Charge injection

The first step to the operation of a PLED is the injection of charge from the electrodes: holes from the anode and electrons from the cathode. The injection process depends strongly on the height of the Schottky barrier at the metal/semiconductor interface between the Fermi level of the metal and the distribution of states of the polymer semiconductor due to the amorphous disorder. The dependence of the injection current on the electric properties at the interface is described using models borrowed from inorganic semiconductor device physics.

The thermionic emission model is used when the Schottky barrier is lower or comparable with the thermal energy of the charges and for low electric fields. The current has the form

$$I = A^* \, T^2 \, e^{\frac{-\Phi_B^{eff}}{kT}} \tag{1.6}$$

where A^* is the effective Richardson constant and T is the temperature. The image charge potential reduces the barrier height and Φ_B^{eff} is the effective barrier that contains the dependence on the field. This model describes a thermally activated injection with an Arrhenius equation.

The Fowler-Nordheim quantum mechanical tunneling model considers the case of a triangular barrier higher than the thermal energy

$$I \propto E^2 \; e^{\frac{-\kappa \Phi_B^{3/2}}{E}} \qquad (1.7)$$

where E is the electric field and κ is a constant in terms of the carrier effective mass. The model provides a better description of the injection current at high electric fields and high energy barriers. A trap-assisted injection mechanism where the charge is injected to a localised states with a lower injection energy barrier which reflects in a reduced temperature dependence with respect to the classical thermionic injection [41].

1.2.4 Charge transport

Once the charges are inside the polymer active layer they migrate subject to the applied electric field via a hopping mechanism to the adjacent localised states. The distribution of energies is governed by the intrinsic disorder in the polymer bulk. Two main different conduction regimes can be observed in PLEDs: injection limited regime and space-charge limited regime.

When the Schottky energy barrier at the interface with contacts is large compared to the energy barrier for hopping between adjacent chromophores (i.e. relatively large polymer mobility) the current across the PLED is limited by the rate of carrier injection and thus it is strongly dependent on the height of the injection barrier.

When the injection barrier is lower and the energy barrier for hopping between adjacent chromophores is lower than or comparable with the thermal energy, the current is space-charge limited (SCL). The charge injection from the electrode is faster than the migration of charges away into the polymer

59

layer and the accumulation of space-charges disturbs the the local electric field limiting the current. When the metal-semiconductor contact is non-ohmic, i.e. a large Schottky barrier is present, the current regime can pass from injection limited to SCL by increasing the forward bias.

Polymer semiconductors differ drastically from their inorganic counterpart as no delocalised valence and conduction band are present due to their intrinsic lack of order. The models that describe better the current in PLED devices contain field dependent parameters analogous to that observed in trapped-charge limited current models for inorganic semiconductors.

When characterising the different conduction limiting regimes in PLEDs, usually single carrier diodes are used to take into consideration only unipolar current and reduce the complexity of the system. Nevertheless, efficient PLEDs are based on well balanced bipolar currents that show a strong reciprocal interaction that results in reduced the net space-charge and electron-hole recombination. In simple models these processes are taken into account introducing a Langevin recombination term to unipolar current equation.

1.2.5 Device efficiency

The External Quantum Efficiency (EQE) is one of the most common way to report the efficiency of an LED. Such value can be easily measured as it is given by the ratio between the number of charges injected (electrons or holes) and the number of photon emitted. A series of factors contribute to the EQE as described by the relation

$$EQE = IQE \cdot \eta_{out} = \eta_{PL} \cdot r_{st} \cdot \gamma \cdot \eta_{out} \tag{1.8}$$

where η_{PL} (photoluminescence quantum efficiency) is the probability of an exciton in the active layer to decay radiatively by emitting a photon. The r_{st} is the ratio between singlet excitons and triplet excitons which is equal to 0.25 due to spin multiplicity. The γ is the number of excitons formed per unitary charge injected in the active layer. The η_{out} is the light out-coupling efficiency: the link between the EQE and the Internal Quantum Efficiency (IQE) is given by the ratio between the number of photons generated inside the active layer and those that are emitted by the device. It depends on a large number of optical and geometrical parameters that make it very difficult to assess.

1.2.6   Indium tin oxide replacement

Indium Tin Oxide (ITO) is currently the material of choice for transparent electrodes. Thin film ITO is used as transparent electrode in displays and solar cells, surface heater film camera lenses, heat reflecting film for windows and many others [32]. Nevertheless, ITO shows some limitations for future applications mainly due to: indium growing costs for its scarcity [42]. ITO is also a brittle material not suitable for flexible devices [43]. In addition, the high temperatures needed for its deposition do not get along well with the use of plastic based flexible substrates [32, 44].

Even if ITO is still the most widespread transparent conductor, the research of a replacement material is seen as an inevitable way to go in the next decade. Thanks to its electronic properties, graphene is one of the most promising materials for this purpose as a very thin nanometric layers of it presents high electrical conductivities together with a high light transparency

and also great mechanical flexibility. Moreover, the ambipolar electric field effect in graphene allows to tune the Fermi level continuously in a wide range of values without compromising its properties.

1.3 Graphene

Graphene is a monoatomic sheet of carbon atoms hybridized sp^2 and arranged in a regular honeycomb hexagonal lattice as shown in Fig 1.9. Together with diamond, graphite, fullerenes and nanotubes graphene is one of the allotropes of carbon. It can be found in nature as the component of graphite where graphene sheets are piled on one another, bound through π-stacking supramolecular interactions. The stacking structures ABA and ABC (see Fig.1.8) are present in graphite.

Graphene's electronic structure was predicted for the first time by P.R. Wallace in 1947 whose aim was to describe graphite starting from a single layer graphene as its basic component [45]. The electronic properties of graphene also revealed to be useful in later years to explain the physics of fullerene first and carbon nanotubes more recently [46]. Even if few reports are present on the isolation of single-layer graphene or thin graphite were published [47], very scarce experimental work was done until 2004 when Novoselov, Geim and co-workers at the University of Manchester characterized the electronic properties of a monolayer of graphene obtained with a simple method they devised, now known as micro-mechanical exfoliation of graphite [48]. Their method consists in using a commercial scotch tape to peel off a small flake from a piece of HOPG and then by repeatedly pressing the tape on the flake and pulling apart in order to cleave it into thinner
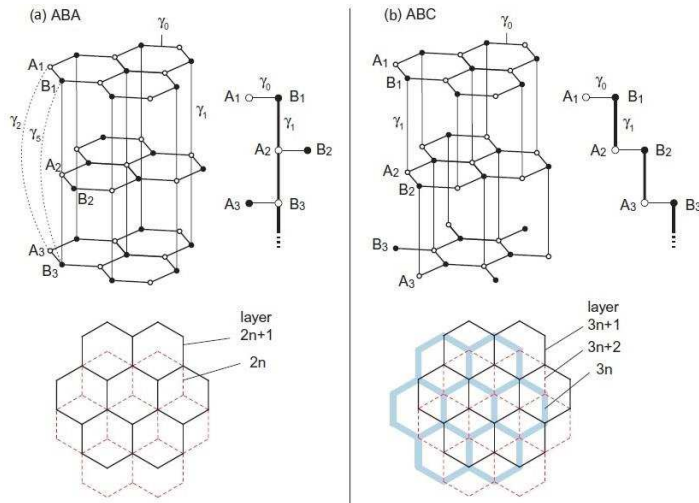
Figure 1.8: Lattice structure of (a) ABA-stacked multilayer graphene and (b) ABC-stacked multilayer graphene (adapted from [3]). All possible carbon-carbon interactions are depicted with indexes γ_i.

fragments until some of the cleaved flakes are actually monolayer graphene. Finally, the tape bearing the monolayers is stuck on a Si/SiO_2 substrate and pulled back off very slowly to leave some of the flakes on the surface. The monolayers need to be localized and this can be done using both optical microscopy and atomic force microscopy [49].
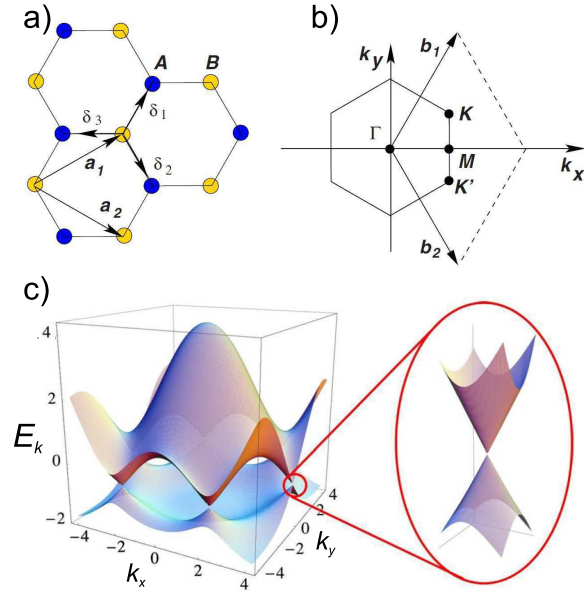
Figure 1.9: Graphene honeycomb lattice is formed by two rhomboid sublattices (blue and yellow atoms in (a)) with the same unit vectors a_1 and a_2. The δ_1, δ_2 and δ_3 are the nearest neighbors vectors. Next-nearest neighbors vectors point to atoms within the same sublattice. The first Brillouin zone in (b) shows the high symmetry points Γ, M, K and K'. The band structure for the π molecular orbitals in the first Brillouin zone is shown in (c) in the case of $t' \neq 0$. The conical structure at the Dirac point is zoomed-in in the inset. (adapted from [4])

1.3.1 The electronic properties of graphene

Crystallographic and electronic structure

The crystallographic structure of graphene can be described as constituted of two equivalent rhomboid Bravais sublattices as reported in Fig.1.9(a) [50, 4].

The unit vectors in the real space are given by:

$$\mathbf{a_1} = \left(\frac{3a}{2}, \frac{\sqrt{3}a}{2} \right) \quad \mathbf{a_2} = \left(\frac{3a}{2}, -\frac{\sqrt{3}a}{2} \right), \tag{1.9}$$

where $a = 1.42$ Åis the bond length in graphene. In the reciprocal lattice the unit vectors are:

$$\mathbf{b_1} = \left(\frac{2\pi}{3a}, \frac{2\pi}{3\sqrt{3}a} \right) \quad \mathbf{b_2} = \left(\frac{2\pi}{3a}, -\frac{2\pi}{3\sqrt{3}a} \right). \tag{1.10}$$

The energy dispersion can be calculated with a tight binding model. The energy required for the electrons to "hop" between different carbon atoms is calculated with exchange integrals and it is $t = 2.8$ eV to hop to the nearest neighbor atoms whereas for the next-nearest neighbor atoms the energy is t' such that $0.02t \leq t' \leq 0.2t$ (see Fig. 1.9) [4, 45, 46]. The simplified band structure has the form

$$E_{\pm}(\mathbf{k}) = \pm t\sqrt{3 + f(\mathbf{k})} - t' f(\mathbf{k}) \tag{1.11}$$

$$f(\mathbf{k}) = 2 \cos\left(\sqrt{3}k_y a \right) + 4 \cos\left(\frac{\sqrt{3}}{2}k_y a \right) \cos\left(\frac{3}{2}k_x a \right) \tag{1.12}$$

where the negative sign applies to the valence band (π binding molecular orbital) and the positive sign to the conduction band (π^* antibonding molecular orbital). The symmetry between the two bands is broken when hopping within the same sublattice ($t' \neq 0$) is also taken into account.

The Dirac points

The Fermi level for pristine graphene is at the crossing point between the two bands in correspondence of the symmetry points K and K' in the Brillouin zone where valence and conductive bands meet forming the characteristic

cone shapes. They are commonly called Dirac points because if the energy dispersion next to K or K' is expanded we obtain

$$E_{\pm}(\mathbf{q}) \approx \pm \hbar v_F |\mathbf{q}| = \pm v_F |\mathbf{p}| \qquad (1.13)$$

where $q = k - K$ for $q \ll K$ is the momentum measured relatively to the points K or K' and v_F is the Fermi velocity, given by $v_F = 3ta/2$ whose value is calculated as $v_F = 1 \times 10^6 \ m/s$. This result was obtained by Wallace in 1947 [45]. Considering the relativistic nature of electrons in graphene near K and K' then the energy is given by

$$\epsilon = \sqrt{m^2 c^4 + c^2 \mathbf{p}^2} \qquad (1.14)$$

where m_0 is the electron mass at rest. By replacing c with $v_F = c/300$ and by setting $m_0 = 0$ the energy dispersion of graphene $\epsilon \approx v_F |\mathbf{p}|$ can be obtained. Due to the interaction with a honeycomb lattice potential, electrons near the points K and K' in graphene behave like relativistic quasi-particles which are described by the the Dirac equation. These quasi-particles are called massless Dirac fermions and can be seen either as electrons that have lost their rest mass m_0 or as neutrinos that acquired the electron charge e [5].

Another peculiar property of graphene near the Dirac points is that the Fermi velocity of electrons is constant $v_F = c/300$ and in first approximation does not depend on their energy. On the contrary, the energy dispersion for conventional metals and semiconductors is $\epsilon(\mathbf{k}) = \hbar^2 |\mathbf{k}|^2/(2m)$ which instead leads to a Fermi velocity $v_F = \sqrt{2E/m}$ that depends on the energy of the particle, being $v = k/m = \sqrt{2E/m}$.

The density of states

The density of states (DOS) is defined as the number of energy eigenstates in a unit energy interval and is reported in Fig. 1.10 either for the case in which next-nearest neighbor hopping is considered ($t' \neq 0$) or not ($t' = 0$). In particular, in the case of $t' = 0$ it is possible to obtain an analytical expression for the DOS [4]. Close to the Dirac point, in the approximation of linear dispersion $E(k) = \pm v_F \hbar |\mathbf{k}|$, the density of state is given by $g(E) \propto |E|/v_F^2$. Although the DOS is equal to zero at the Fermi energy, the conductivity of graphene does not disappear, thus showing a metallic behavior. For this reason graphene is defined as a zero-gap semiconductor.
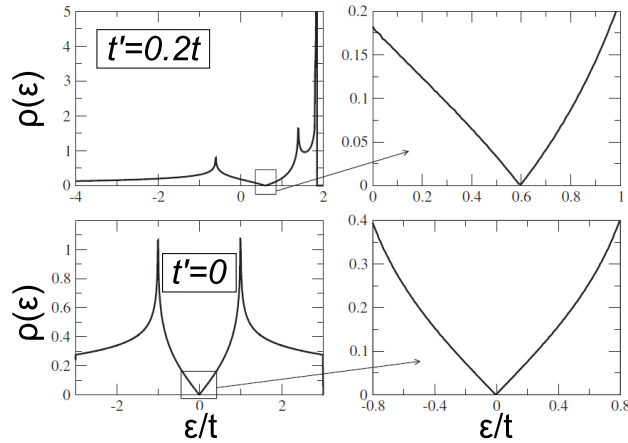
Figure 1.10: The density of states (DOS) for $t' \neq 0$ (top row) and for $t' = 0$ (bottom row). The DOS near the Dirac point is zoomed-in in the diagrams on the right column. (adapted from [4])

When single-layer graphene is used as the active layer of a field-effect transistor it shows a strong ambipolar electric field effect upon application

of a gate voltage bias. Either a concentration of electrons or holes can be induced continuously based on the the sign of the gate bias and in both cases it causes a rapid decrease in the resistivity (see Fig. 1.11) [5]. Charge carriers concentrations up to 10^{13} cm^{-2} can be obtained with mobilities higher than $15,000$ $cm^2V^{-1}s^{-1}$ even under ambient conditions. The mobility in graphene is weakly affected by the temperature and it remains high even for high doping levels with charge carrier concentrations higher than 10^{12} cm^{-2}, suggesting a ballistic transport at submicrometre scale.
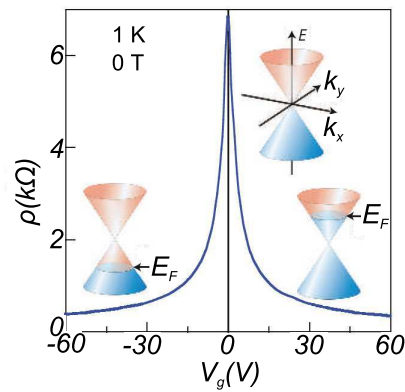
Figure 1.11: The resitivity of a monolayer of graphene as a function of gate voltage shows an ambipolar electric field effect. A variation in the gate voltage V_g can move the Fermi energy of graphene continuously around the neutrality point: positive (negative) V_g induce electrons (holes) concentration to increase according to the DOS. The conical low-energy dispersion is shown in the inset to indicate the position of the Fermi energy. (adapted from [5])

Optical conductivity

As a consequence of the linear dispersion at the Dirac point, optical conductance of graphene monolayer for electronic $\pi \to \pi^*$ interband transitions is not dependent on the frequency for a broad range of photon energies (theoretically from $0\ eV$ to $\sim 2\ eV$ where the energy dispersion begins to deviate from linearity) and it is equal to $G_0 = e^2/4\hbar \simeq 6.8 \times 10^{-5}\ \Omega^{-1}$ [51]. Based on Fresnel equations it is possible to derive the theoretical optical transmittance of a freestanding monolayer graphene

$$T = (1 + \frac{\pi\alpha}{2})^{-2} \simeq 1 - \pi\alpha \simeq 97.7\% \qquad (1.15)$$

where $\alpha = e^2/\hbar c = 1/137$ is called the 'fine structure constant' and it is a universal constant. Absorbance $A = 1 - T = \pi\alpha \simeq 2.3\%$ was confirmed experimentally for a monolayer and also for few layer graphene where absorption increases linearly according to the number of sheets [52]. This result shows that in few layer graphene (FLG) the single sheet can be considered as a two-dimensional electron gas almost non-interacting with the adjacent layers. In the range of visible light the reflectance of graphene was measured to be $< 0.1\%$, much lower than absorbance.

In the visible range, the absorbance starts to increase for increasing energy moving away from the Dirac points and hence from the linearity of the energy dispersion. The spectra show a peak at $\sim 4.6\ eV$ which is attributed to a van Hove singularity in the density of states (see Fig. 1.10) at the symmetry point M in the Brillouin zone where the electronic bands form a saddle point [53, 54]. Due to a strong excitonic interaction between the excited electron in the conduction band and a hole in the valence band, the peak in graphene UV-vis spectra is red-shifted with respect to the $\pi \to \pi^*$ transition at the M

point which is originally of $\sim 5.2\ eV$ [55].

Electrical conductivity

An important observation is that the conductivity of pristine graphene never disappears, even near 0 K at zero-field $V_g = 0$, where $g(E) \simeq 0$, it shows a conductivity equal to a quantum conductivity for each species of charge carriers $2G_0 = 2e^2/h \simeq 7.75 \times 10^{-5}\ \Omega^{-1}$ equivalent to a sheet resistance of $\sim 6\ k\Omega/\square$ for a single layer [5, 56]. Nevertheless, given that the charge-carriers mobility remains high even for a high concentration of carriers, the resistance can be reduced down to $\sim 50\ \Omega/\square$ by chemical doping [56]. Even unintentional doping due to the absorption of molecules (e.g. water) from the atmosphere can cause a carrier concentration of the order of $10^{12}\ cm^{-1}$ [48]. Considering a common value of $\mu = 10^5\ cm^2s^{-1}V^{-1}$ for carrier mobility at a doping level of $n = 10^{12}\ cm^{-2}$, the sheet resistance can be expressed as

$$R_s = \frac{1}{e\mu nN} = \frac{62.4\ \Omega}{N} \tag{1.16}$$

where N is the number of graphene sheets [57]. Electrical conductivity is strongly hampered by the presence of lattice defects which cause a decrease of the mobility[58].

Multilayer graphene

The interplane coupling in multilayer graphene is weak compared to the C-C bonding energy such that the optical absorption is not altered significantly. However, the interaction between the different graphene layers leads to some key modification in the band structure. The change in the electronic properties of bilayer graphene stacked in an AB (Bernal) configuration (which

corresponds to a relative rotation of $\theta = 60°$ between the two honeycomb lattices, see Fig.1.12a) is due to the inter-layer interactions between carbon atoms which break the symmetry between the two sublattices in each of the two sheets. To account for the different possible interactions between atoms from the two layers a number of terms are added to the Hamiltonian of the system, each one with a weighting factor. In a first approximation, if only interactions up to γ_1 are considered, the band structure of graphene Bernal stacking bilayer results in four parabolic-shaped bands (see Fig.1.12b), two of which touch at $E = 0$ while the other two are equally distant from $E = 0$ in the symmetric bands case $t' = 0$, when the in-plane next-nearest neighbours hopping is neglected [4]. The parabolic shape determines a drastic reduction in the Fermi velocity of electrons at the Dirac point. In addition to this, the application of a bias between the two layers is able to open a band-gap which is extremely interesting for electronic applications of graphene [4]. If a further out-of-plane interaction γ_3 is considered, a trigonal distortion (warping) of the bands, at much lower energies than parabolic distortion, gives rise to the formation of a set of three Dirac-like linear bands at finite momentum (see Fig.1.12c) [7].

This approach where hopping terms between different atoms from different layers are added to the Hamiltonian in the tight-binding model can be extended to calculate the energy structure with an infinite number of layers in a Bernal stacking configuration. The addition of layers to the system increases the complexity of the energy structure as each new layer introduces 2 more bands for the π/π^* orbitals [6].

The relative orientation (θ) between any couple of consecutive layers has
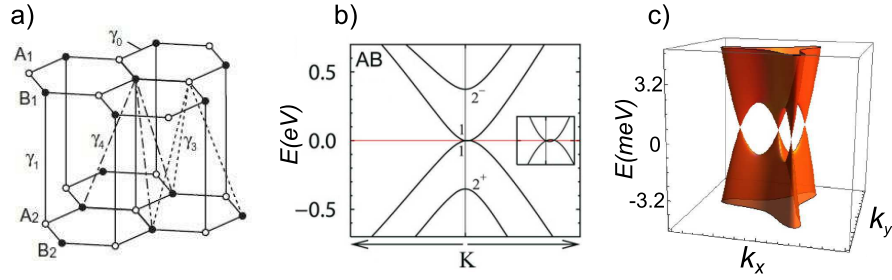
Figure 1.12: A regular AB (Bernal) stacking graphene bilayer is shown in (a) where the most important possible hoppings between the two layers are indicated with γ_i indices. In panel (b) I report the band structure obtained by considering interactions up to γ_1 in the tight binding Hamiltonian. If also γ_3 is considered a trigonal warping results at very low energies at the touching point between two of the bands, restoring conical structures. (Adapted from [3, 6, 7])

a strong effect on the electronic structure of the system due to the modulation of the electronic density for the formation of a Moireé pattern. Bilayer graphene where the rotation angle is different from the ordered Bernal AB stacking ($\theta \neq 60°$) are referred to twisted bilayer graphene. The effect of this relative rotation is to decouple preferential interaction between certain atoms from the two sheets partially restoring the broken symmetry of a monolayer graphene and its properties [59].

Chemical doping

The strong ambipolar field effect of graphene allows to control the doping continuously from p-type to n-type by varying the charge carriers concentration. Therefore, electrical conductivity and Fermi energy of graphene can

be finely tuned. Chemical doping reduces the effects of unwanted doping due to contamination and is a powerful method to tune the electrical properties of graphene [60]. Chemical doping of graphene can be done either via surface transfer between graphene and adsorbed molecules or via substitutional doping where carbon atoms in graphene lattice are replaced with species with different number of valence electrons [60]. The factor that determines the doping level via the surface charge transfer is the relative position of the Fermi level of graphene with the highest occupied molecular orbital (HOMO) and the lowest unoccupied molecular orbital (LUMO) of the dopant molecule. The dopant acts as a donor (n-type doping) if the HOMO level is above the Fermi energy of graphene whereas a p-type doping is obtained if the LUMO level of the dopant is below the Fermi energy of graphene and a charge transfer of electrons occurs from graphene to the dopant molecule.

1.3.2 Methods of production

Since graphene was first isolated with the Scotch-tape method a variety of different synthetic routes have been developed to obtain ever larger sheets with high quality and high throughput. This is important target especially to extend the potential of graphene and its application to the market. Each of these preparation methods results in a material with slightly different properties that can be appropriate for different applications [61]. There is a number of methods that differentiate on the basis of sheet size, number of layers, quality, processability, the possibility to implement the method for mass production or for large-area applications and their cost and ease of fabrication [62]. In the rest of the chapter I will present briefly some of the

most important and used methods.

Mechanical exfoliation

Mechanical exfoliation is a very intuitive method that was used to obtain monolayer graphene on Si/SiO_2 for the first time by Novoselov and Geim in 2004. Nevertheless, this procedure is impossible to scale to mass production and large area applications. Only a small percentage of high quality monolayer or few layer graphene is present among multilayer and graphite like chunks on the substrate surface. The localisation of mono-atomic sheets of graphene on Si/SiO_2 is a time-consuming step and is made possible thanks to the fact that, with a SiO_2 layer of 300 nm, they add to the optical path of the reflected light and change the contrast with respect to an empty surface up to about 12%, sufficiently enough to be detectable with an optical microscope [48, 49].

Liquid-phase exfoliation

Liquid-phase exfoliation (LPE) is based on the separation of single and few layer graphene layers from HOPG by the use of an ultrasonic treatment in an appropriate solvent such as N-methyl-2-pyrrolidone (NMP), dimethylformamide (DMF) and others. The matching of the surface energies between graphene and the solvent is a key factor to obtain a stable dispersion of thin layers. Dispersions of graphene can be obtained also in water or relatively polar organic solvent with the use of a suitable surfactant which stabilizes the graphene flakes [63, 64, 65, 66].

Graphene sheets obtained by ultrasonication are limited in lateral size as

the energetic exfoliation process causes them to break in smaller flakes. Also the crystal quality of a single flake is much lower compared to mechanically exfoliated graphene as many defects are produced during the sonication. On the other hand LPE is a very economic method and one of the most promising for large area applications. In fact graphene liquid dispersions can be easily handled and deposited on a number of different substrates using printing technologies.

Graphene oxide

Graphene oxide is obtained by the chemical oxidation of graphite with the insertion on the graphene lattice of oxygen groups such as hydroxyl (C-OH), carbonyl (C=O), carboxyl (O-C=O) and epoxy (C-O-C) groups [67]. These functional groups are characterised by the presence of a electric dipole that make the surface much more hydrophilic than pristine graphene and hence the flakes are readily soluble in water. Graphene oxide forms very stable dispersion of monolayers in water which are also very easy to deposit on hydrophilic substrates such as glass, quartz or silicon oxide as single flakes [68]. Nevertheless the introduction of oxygen atoms together with a high number of structural defects generated by the strong oxidation reaction causes a drastic reduction of the charge carrier mobility. Graphene-like domains with different size and shape are enclosed by oxidized regions and it makes graphene oxide flakes much less electrically conductive proportionally to the degree of oxidation [69]. The partial reduction of graphene oxide with the removal of oxygen groups can be achieved with different methods to improve electrical conductivity and partially restore the band structure of pristine

graphene [70, 71, 72].

Chemical vapour deposition

Chemical vapour deposition (CVD) is maybe the most promising method to obtain large area graphene with good electrical conductivity [73]. In a basic form of CVD, a flux of methane is fed on a thin foil of copper at high temperatures of about 1000 $°C$. The hydrocarbon decomposes and domains of monoatomic layers of carbon grow and eventually coalesce generating a poly crystalline thin film of mono and multi layer graphene [74]. The film so obtained needs to be transferred on the desired substrates by depositing a thin layer of PMMA and chemically etching the copper foil. After the deposition on the substrate the PMMA is removed. Sheet resistances as low as few hundreds of $\Omega/\square$ can be obtained with multilayer CVD graphene and the use of chemical doping methods on large area films [75].

Epitaxial graphene

Epitaxial graphene can be obtained through segregation from silicon carbide (SiC) by thermal annealing between 1250 $°C$ and 1450 $°C$ [76]. This type of graphene is believed to retain the physical properties of mechanically exfoliated flakes especially when electronically decoupled from the SiC substrates via hydrogen treatment [77].

Chapter 2

Thermal treatment and chemical doping of semi-transparent graphene films

Graphene transparent conductive films have been proposed as indium tin oxide (ITO) modifiers for application in optoelectronic devices. Here thermal and chemical treatments of graphene-based transparent films are systematically investigated with a view to increasing their conductivity and tuning their work function. Two different types of graphene layers are investigated, obtained either via spin-coating of graphene oxide (GO) aqueous dispersions or vacuum filtration and transfer of liquid-phase exfoliated (LPE) graphene in highly volatile, non-toxic solvents such as isopropanol and ethanol. As-deposited films are relatively resistive, but their sheet resistance was decreased

by up to three orders of magnitude for both LPE and GO, so as to reach values of $\sim 10^5$ $\Omega/\square$ via thermal treatments at temperatures of $\sim 350/400$ °C at pressures of $\sim 10^6/10^4$ mbar. Most importantly, the physisorption of the molecule $(CF_3SO_2)_2NH$ (trifluoromethanesulfonimide) results in an increase of the films work function by up to 0.5 eV, to yield a value of ~ 5.3 eV. This is comparable or slightly better than what can be achieved with poly(3,4-ethylenedioxythiophene) doped with poly(styrenesulphonate) (PEDOT:PSS), depending on PSS concentration, thereby confirming the potentially beneficial role of chemical doping of liquid dispersions of graphene-derivatives for application to organic electronics.

2.1   Introduction

Graphene is one of the most interesting candidate materials for the production of transparent conductive films for flexible optoelectronic applications such as light-emitting diodes (LEDs) or photovoltaics. Graphene is a monoatomic layer of carbon atoms arranged in a honeycomb lattice. It combines a good transparency (2.3 % transmittance for a single layer for wavelengths higher than ~ 400 nm [52]), good charge carrier mobility [78] ($\sim 10^5$ cm^2 s^{-1} V^{-1}) and promising mechanical properties [79].

Thanks to a strong ambipolar field-effect, the tuning of the Fermi energy of either sign causes a variation in the charge carrier concentration and hence of the electrical conductivity of graphene [5]. As a consequence of this, for a single layer of graphene the sheet resistance can be reduced from ~ 6 $k\Omega/\square$ for the undoped graphene to few hundreds of $\Omega/\square$ via intentional or serendipitous chemical doping with molecules such as H_2O, NO_2

and NH_3, or by applying a gate voltage of $\sim 100\ V$ or so [56, 48].

Since it was first isolated in 2004, different production methods have been developed for graphene. They all result in products with slightly different physical properties depending on the size of the graphene flakes, the integrity of the honeycomb lattice and the presence of chemical defects [80, 61]. The application of graphene in optoelectronic devices requires films with areas up to several cm^2 and a production method that can be scaled-up for massive production. Only few of the existing synthetic approaches meet these requirements.

The chemical vapour deposition (CVD) method is generally reported to produce multi crystalline films of graphene, with domains of up to 50 μm or larger [74, 81]. In a basic configuration methane and hydrogen gas are passed through a reactor at high temperature ($\sim 1000\ ^\circ C$) to activate the growth of graphene domains on a thin copper foil (25 μm) as a catalytic substrate [82]. A polymer layer is then deposited on the film and the copper foil is etched in a $FeCl_3$ solution. The graphene is transferred onto the final substrate and the polymer layer is washed away. Large-area films with a sheet resistance as low as $\sim 200\ \Omega/\square$ have been obtained with a roll-to-roll adaptation of this method [73]. The use of high temperatures reactors, an ignitable gas and the dependence on an expensive metal as copper are the main shortcomings of this method that need to be considered when upscaling the process towards industrial production.

Less expensive and highly-scalable methods for the production of graphene are based on the exfoliation of graphite powder in a solvent to obtain liquid dispersions of mono and multi layer graphene flakes [63, 83, 84]. The

exfoliation process is based on the surface energy matching between the graphene sheets and the solvent [63]. Interestingly, the range of suitable solvents can be usefully extended by using a variety of surfactants, also with a view to using water as a dispersant [85, 65, 66].

In the liquid-phase exfoliation approach, a low power bath sonication provides enough energy to intercalate solvent molecules between the graphene planes and to exfoliate them mechanically. Alternatively, exfoliation can also be achieved after chemical modification of graphite via extensive oxidation to separate the graphene sheets [86, 72]. The formation of oxygen functional groups on the graphene lattice increases drastically the affinity of the flakes for polar solvents such as water. Liquid-phase exfoliated (LPE) graphene and graphene oxide (GO) are characterized by flakes with sizes up to several microns [63, 86].

Crucially, and differently from CVD graphene, LPE and GO dispersions can be obtained in large quantities (easily up to kilograms) via scalable processes and relatively low costs. This is of enormous technological significance, because the liquid dispersions can be used as conductive inks with already existing ink-jet and roll-to-roll printing technology for printable electronics [87, 88]. Nevertheless, although technologically very appealing, films obtained by deposition of either LPE or GO are constituted by a number of overlapping flakes. The charge transport in such films occurs via hopping between consecutive flakes and constitutes one of the main limits to the conductivity. In addition, oxidation of graphite typically introduces a number of lattice defects, leading to a lower quality graphene in terms of charge mobility and thus conductivity, also in relation to the need of charge to hop

82

between conjugated domains [63, 83, 84, 85, 65, 66, 86, 72, 87, 88, 70].

Several methods have been proposed to reduce the amount of such defects and restore the properties of graphene, at least partially. They generally involve either high temperatures annealing (typically > 1000 °C for few hours), lower temperatures but extremely long times (e.g. several days at 80 °C), electrochemical treatments or even chemical reduction of GO with hydrazine [70, 68, 89, 90, 91, 92].
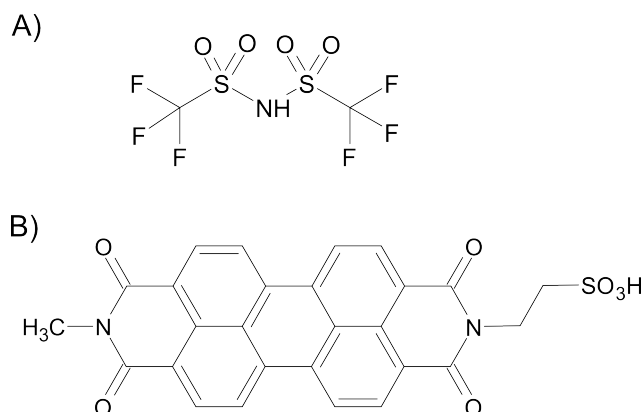
Figure 2.1: (A) Molecular formula of bis(trifluoromethanesulfonyl)amide (TFSA) used as p doping agent. (B) Molecular formula of the sulphonated perylene diimmide derivative (PDI) used as surfactant for the exfoliation of graphite in ethanol.

In this work, the tuning of the work function of thin transparent films of LPE and GO is reported after thermal treatments at relatively mild temperature (350/400 °C) for only few hours, which also significantly increase their conductivity. The ability to control the work function of thin films is of paramount importance for applications as components of electronics devices [93, 34].

The effect of chemical p-type doping on LPE and reduced GO films was studied for the tuning of the electrical properties. In particular, the electron-withdrawing molecule 1,1,1 trifluoro-N-(trifluoromethyl)sulfonylme-thanesulfonamide (TFSA, see Fig.2.1 panel A) was used as a p doping agent on graphene [94, 95, 96]. By decreasing the electron density of graphene, TFSA shifts the Fermi level towards lower energies where the density of states (DOS) is higher, thereby increasing the conductivity of the material. Interestingly, via the deposition of TFSA an increase in the work function of the films by 0.5 eV was achieved to a final value of about 5.3 eV.

2.2 Experimental details

2.2.1 Preparation of the dispersions

A GO water dispersion was prepared via a modified Hummers method [86] obtaining a final concentration of about 1 $g\ L^{-1}$. Two LPE graphene dispersions were prepared via low power ($\sim 50\ W$) bath sonication of graphite flakes (Sigma Aldrich 332461) in low boiling point organic solvents such as isopropanol and ethanol. For the preparation of the dispersion LPE(1), graphite was added to isopropanol at a concentration of 3 $g\ L^{-1}$.

A second dispersion, LPE(2), was prepared with the same concentration of graphite in ethanol and with the addition of 0.1 $g\ L^{-1}$ of a sulphonated perylene diimide derivative (PDI, see Fig.2.1 panel B) as a surfactant and exfoliation agent provided by BASF SE. The molecules of PDI interact with the surface of graphene thanks to their polyaromatic molecular structure. For this type of surfactants, lateral functionalisation with electron withdrawing

84

or electron accepting groups are used to increase their solubility in more polar organic solvents or even in water [85, 97]. Both imide and sulfonic lateral groups are present and the exfoliation of graphite is carried out in ethanol, a rather polar organic solvent.

For both dispersions the mixture was sonicated for 4.5 h and then centrifuged at 2200 rpm for 20 minutes to precipitate and remove the bigger aggregates and the non-exfoliated grains. The absorption spectra of the final dispersions are reported in Fig.2.2. The concentration of LPE graphene was estimated using the absorption coefficient $\epsilon = 2460$ L g^{-1} m^{-1} at 660 nm [63] obtaining values of $\sim 2 \times 10^2$ g L^{-1} for LPE(1) and $\sim 2 \times 10^1$ g L^{-1} for LPE(2). Since ethanol and isopropanol have similar surface tension, the hugely different concentration of the dispersions (over 10 times) suggests that PDI is an effective surfactant at increasing the exfoliation of graphite and the stabilization of the suspended graphene flakes, in agreement with corroborating literature [63, 65, 66].

2.2.2   Preparation of the thin films

Thin transparent films of LPE graphene were deposited on fused silica substrates. LPE(1) and LPE(2) films were obtained with a vacuum filtration and transfer method [98] of the two corresponding dispersions. A defined volume of the dispersion was vacuum filtrated through a mixed cellulose esters filter (Millipore) with a pore size of 0.025 μm. Before the filtration the cellulose filter was immersed in deionized water for few minutes for hydration and then was placed on a glass fibre funnel for the filtration. A volume of 3 mL of the lower concentration LPE(1) dispersion and 1 mL of the higher
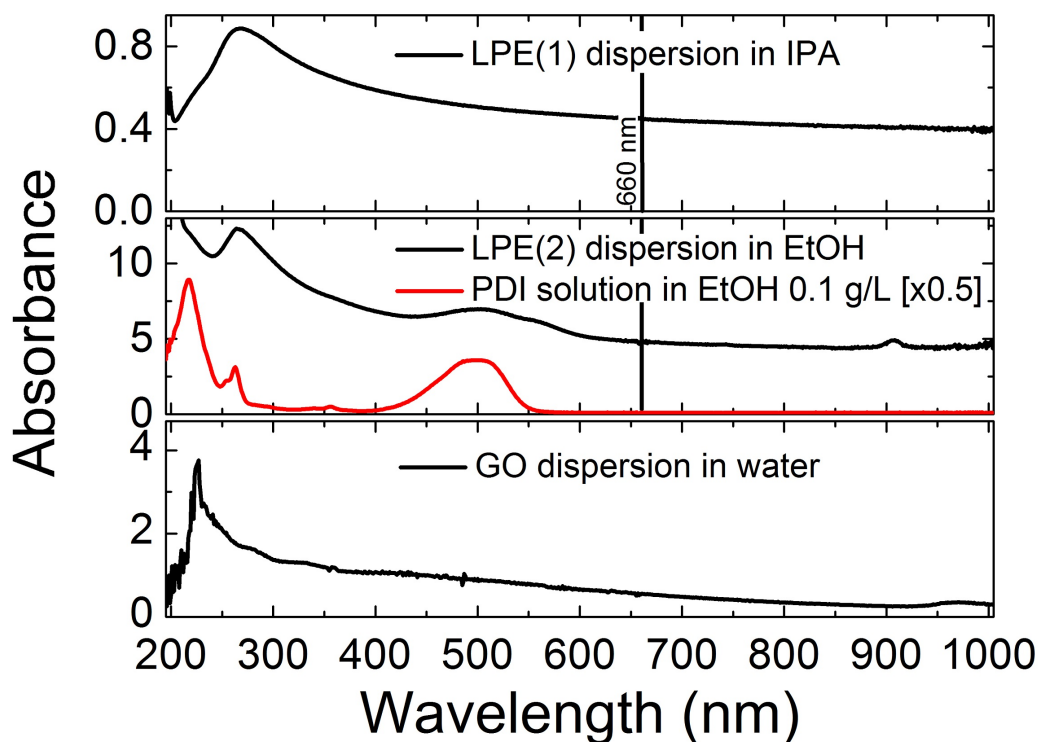
Figure 2.2: UV-vis absorption spectra of liquid phase exfoliated graphene (LPE) and graphene oxide (GO) dispersions. The spectra are reported as $-log$ of the optical transmittance assuming reflectance and scattering to be negligible. The concentration of LPE dispersions was estimated using the absorption coefficient at 660 nm, a guide to the eye is reported to show that the absorption contribution of the surfactant is negligible at that wavelength.

concentration LPE(2) dispersion were vacuum-filtrated. During the filtration the pump was left on for approximately two hours until the filter-cake is fully dry. In the case of LPE(2), after the solvent passed through the filter, 2 mL of deionized water were gently added to help dissolve and remove the remaining surfactant molecules from the graphene layer.

For the transfer step, the filter was cut in smaller pieces with the desired size and shape (~ 1 cm^2). The filter was wet with a drop (~ 5 μL) of dichlorobenzene (DCB), positioned it (graphene side down) on the fused quartz substrate (Spectrosil, UQG) substrate and pressed gently to remove any air bubbles and to make it adhere. Just before the DCB is completely evaporated, the sample was immersed in acetone gently and left it overnight to let the cellulose dissolve. The sample was washed again in fresh acetone and in isopropanol to remove filter residues. In the case of LPE(2) the sample was also washed in deionized water to help removing the remaining surfactant molecules and dried in a vacuum chamber at 10^2 $mbar$ at room temperature for one hour.

Thanks to a stronger interaction of the oxidized graphene flakes with the silica substrates, the GO films were prepared by repeated spin coated depositions of the dispersion on the Spectrosil substrates (1800 rpm for 60 seconds). Three different samples GO(1), GO(2) and GO(3) were prepared with increasing thickness by repeating the spin-coating procedure 1, 2 and 4 times respectively.

2.2.3   Treatments and characterization of the thin films

The surface morphology of the as cast films was characterised by using an atomic force microscope (AFM) Veeco Dimension 3100. The sheet resistance was measured using a collinear four-point probe with contacts spaced 2 mm from each other and controlled with a Keithley 2400 multimeter. The full scale sheet resistance is $\sim 10^9$ $\Omega/\square$. An error of 10% associated to the sheet resistance measurements was estimated based on their variability.

For the thermal treatment of the films the samples were divided in two groups and two different conditions with different pressure, temperature and time duration were tested. The samples LPE(1) and GO(1) were annealed at an air pressure of $\sim 10^{-4} \ mbar$ and a temperature of $350 \ °C$ for 3 hours (ramp of $10 \ °C \ min^{-1}$ starting from room temperature). For the samples LPE(2), GO(2) and GO(3), a lower pressure of $\sim 10^{-6} \ mbar$ and a temperature of $400 \ °C$ for 18 hours (ramp of $1 \ °C \ min^{-1}$ starting from room temperature) were set.

The annealed thin films were chemically doped via spin-coating deposition of the molecule TFSA (Sigma-Aldrich 464635) from a solution in nitromethane (1500 rpm for 60 s). Two solutions of TFSA were prepared with concentrations of 20 mM and 90 mM. For the samples LPE(1) and GO(1) (thermally treated at higher pressure $10^{-4} \ mbar$) two consecutive depositions of TFSA were done with increasing concentration: 20 mM and 90 mM. For the second set of annealed samples LPE(2), GO(2) and GO(3) (lower pressure $10^{-6} \ mbar$ thermal treatment) the TFSA was deposited three times consecutively: 20 mM, 20 mM and 90 mM. The solutions were prepared, kept and deposited under nitrogen atmosphere to preserve TFSA from any contact with oxygen and water. The work function was measured using a macroscopic environmental Kelvin probe with a gold probe with a diameter of 2 mm.
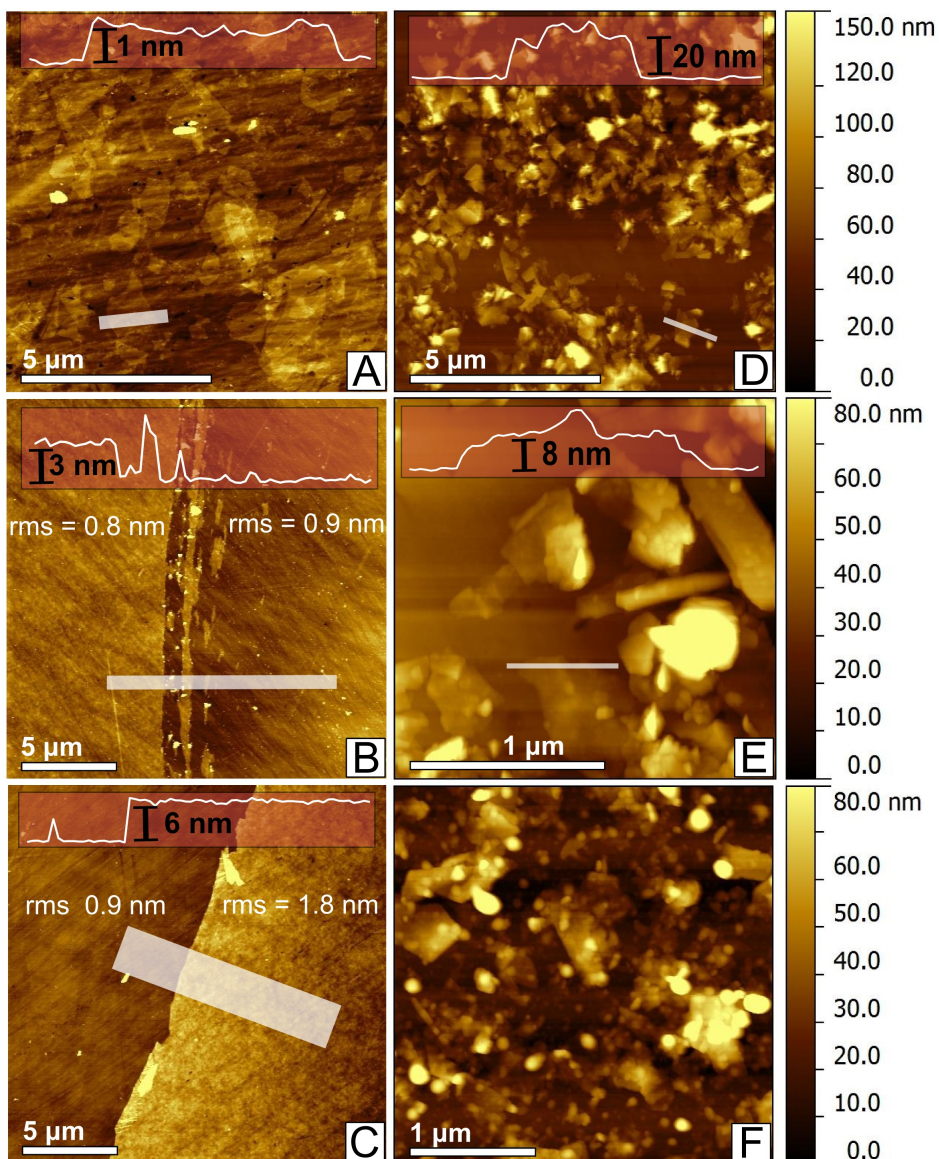
Figure 2.3: Tapping mode AFM height images of graphene oxide (GO) and liquid phase exfoliated graphene (LPE) thin films after the deposition on fused silica substrates (Spectrosil UQG): (A) GO(1), (B) GO(2), (C) GO(3), (D)(E) LPE(1), (F) LPE(2). The false-colour scale bars are relative to the images (D-F) only.

2.3   Results and discussion

2.3.1   Thin films preparation

In Fig.2.3 the AFM morphology of the films are reported. Panel A of Fig.2.3 shows the morphology of GO(1) where a large number of monolayer flakes (thickness ~ 1 nm [86], see the height profile in the inset) are present with a lateral size up to several microns and a surface coverage of about 85%. Larger flakes reduce the number of charge carrier hopping steps and are crucial to achieve higher conductivity [99] which is essential for the application of thin films as charge injection and extraction from the active layer of flexible and stretchable devices.

The GO(2) and GO(3) films have a 100% surface coverage with a roughness very similar to that of the substrate, as shown in Fig.2.3 panels B and C respectively. The thickness of the layers increases with the number of spin-coating depositions: from 3 nm for two depositions to 6 nm for four depositions. The thickness of the GO films was successfully controlled while still maintaining a relatively low root-mean-square (rms) roughness of 0.8 nm for GO(2) and of 1.8 nm for GO(3). The LPE films shown in panels D-F of Fig.2.3 are formed by multi layer flakes and larger aggregates of different sizes. Aggregation is likely to take place during the vacuum filtration when the dispersed graphene is concentrated and compacted onto the filter.

The UV-vis absorption spectra of the films are reported in Fig.2.4. The spectra are reported as $-log$ of the optical transmittance, uncorrected for reflectance (note that the reflectance of graphene is 0.001% of the transmittance [52]). The spectra of LPE graphene films show the typical structure

due to graphene's electronic transitions between the π and the π^* molecular orbitals [54]. The broad and nearly constant absorption tail in the long wavelength range ($>$ 50 nm) derives from the linear energy dispersion around the Dirac point in the electronic structure of graphene [51], whereas the main peak at 267 nm is due to a Van Hove singularity in graphene's density of states [55]. In the case of LPE(2), the absorption features of PDI are visible at $\sim$ 500 nm, thus indicating that surfactant molecules are still present within the film even after the thermal annealing. Note that the relatively roughness of the LPE films (10 nm or so) prevents a meaningful analysis of the correlation between absorption and AFM-measured thickness.
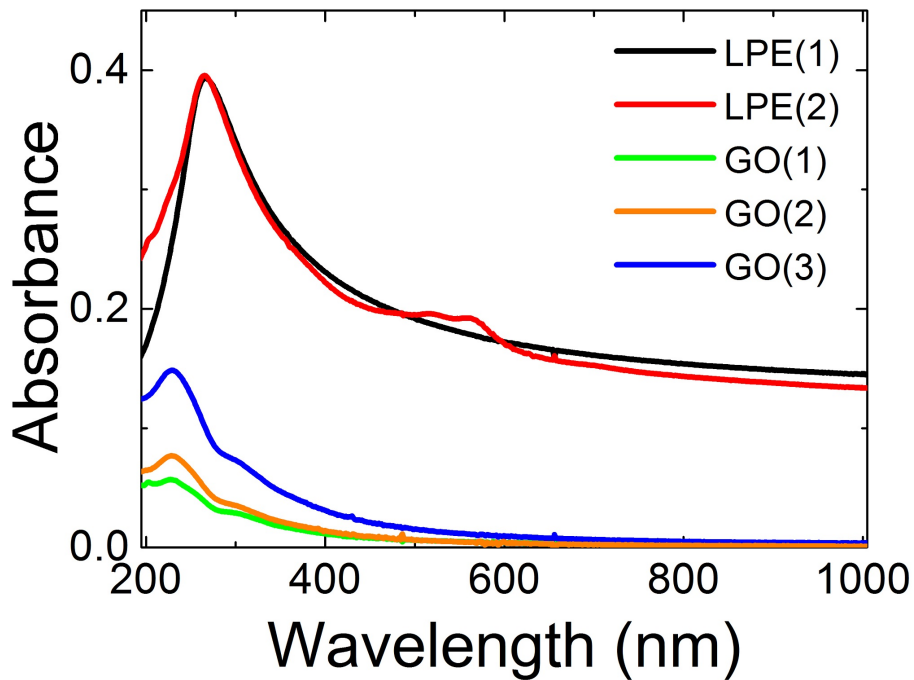
Figure 2.4: UV-vis absorption spectra (as $-log$ of the optical transmittance) of graphene oxide (GO) and liquid-phase exfoliated graphene (LPE) thin films as deposited.

91

The optical transmittance spectra of the GO thin films show a main peak at 228 nm with a shoulder at 300 nm. These features can be assigned to a $C{=}C$ ($\pi \to \pi^*$) transition and a $C{=}O$ ($n \to \pi^*$) transition, respectively [100, 71]. Graphene oxide is composed of pristine graphene domains spatially confined by lattice defects and oxidized regions [101]. The confinement of the pristine domains increases the energy of the π^* transition with respect to larger conjugated domains in LPE graphene [29]. The sheet resistance of the as-deposited films and after every treatment step is reported in Fig.2.5. The values measured for LPE films as cast are 90.7 $M\Omega/\square$ for LPE(1) and 4.4 $M\Omega/\square$ for LPE(2). The as cast GO films have a sheet resistance which is higher than the full scale limit of the system (10^9 $\Omega/\square$), in agreement with the literature [68].

2.3.2   Thermal treatment

To improve the conductivity of the films all the samples were thermally annealed at low pressure. In the case of GO the annealing induces a partial chemical reduction consisting in the removal of oxygen functional groups [102]. The enhancement of the electrical conductivity via annealing of LPE films is instead mainly due to the removal of the solvent residues and to the desorption of the surfactant molecules which improve the electric contact between the flakes [63].

The samples were divided in two sets to test different annealing conditions in terms of pressure, temperature and time duration. The samples LPE(1) and GO(1) were annealed at an air pressure of $\sim 10^{-4}$ $mbar$ and a temperature of 350 $°C$ for 3 hours (ramp of 10 $°C$ min^{-1} starting from
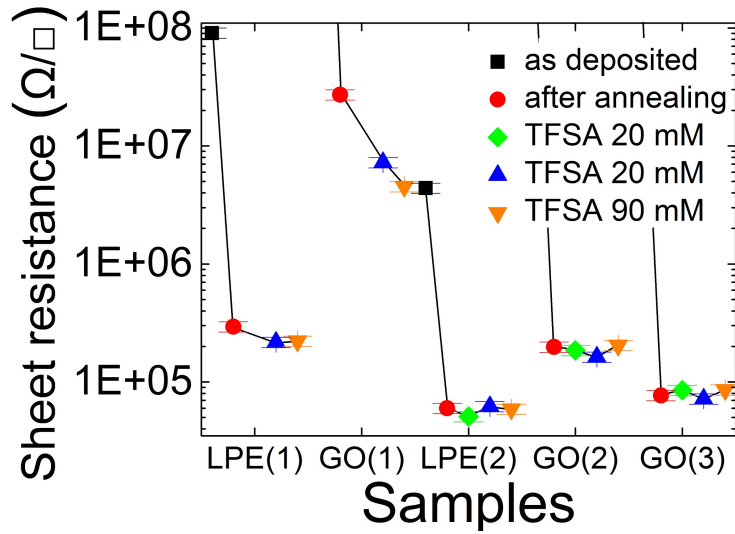
Figure 2.5: Comparison of the sheet resistance values measured before and after the annealing and upon every deposition of TFSA of the films. The sheet resistance of the GO films before the annealing treatment was higher than 10^9 $\Omega/\square$ and over the full-scale of the set-up used. A significant decrease is shown in the case of monolayer graphene oxide GO(1) upon deposition of TFSA suggesting the doping of the material.

room temperature). Instead, the samples LPE(2), GO(2) and GO(3) were annealed at an air pressure of $\sim 10^{-6}$ $mbar$ and a temperature of 400 $^\circ C$ for 18 hours (ramp of 1 $^\circ C$ min^{-1} starting from room temperature). Simulations by Acik and collaborators show that by annealing above 350 $^\circ C$ at low pressure ($\sim 10^{-3}/10^{-4}$ $mbar$) almost all of the oxygen functional groups in GO should be removed, except for hydroxyl groups and cyclic-edge-ethers (ether groups located at the edge of defective areas) [102]. In Fig.2.6 the UV-vis absorption spectra of samples before and after the annealing are compared.
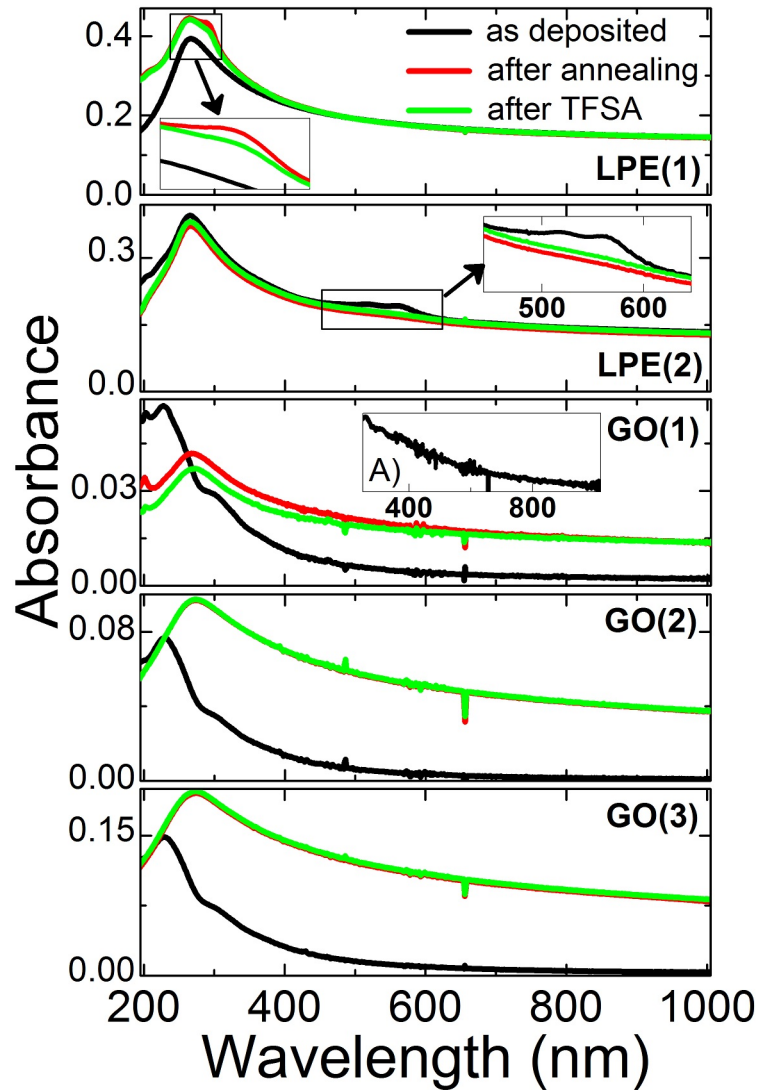
Figure 2.6: UV-vis absorption spectra (as $-log$ of the optical transmittance) of the films as deposited, after annealing and after the deposition of TFSA. The inset (A) depicts the difference between the spectra after annealing and after TFSA with respect to the wavelength for the film GO(1).

The annealing of LPE(1) at 350 $°C$ and 10^{-4} $mbar$ causes the formation of a peak at about 300 nm (see inset in Fig.2.6 for LPE(1)) which could

be attributed to the $n \to \pi^*$ transition of $C=O$ groups indicating a partial oxidation of the film. The oxidation peak is absent in LPE(2) where a much lower pressure (10^{-6} $mbar$) was used for annealing, even if at a higher temperature (400 °C). The inset in Fig.2.6 for LPE(2) shows that the thermal treatment causes a drastic decrease of the absorption features around 500 nm as an evidence of the desorption or degradation of the low-molecular weight surfactant molecules [103]. The annealing results in the chemical reduction of graphene oxide. The removal of oxygen groups leads to larger domains with restored conjugation and a consequent bathochromic shift of λ_{max} from 228 nm to 270 nm as for pristine graphene [54, 71]. Also the increase of absorption across a wide range of wavelengths ($>$ 300 nm) indicates the reduction of graphene oxide with the formation of a linear dispersion of energy characteristic of the electronics structure at the Dirac point in graphene. The thermal treatment causes a drastic decrease ($>$ 2 orders of magnitude) in the sheet resistance of both LPE and GO films as shown in Fig.2.5.

2.3.3 Chemical doping

The annealed thin films were chemically doped via repeated spin-coating depositions of TFSA in nitromethane with increasing concentrations. Fig.2.5 shows the variation of the sheet resistance after every deposition of TFSA. As expected for the doping of graphene, a significant decrease of the sheet resistance for GO(1) by more than 80% was measured. This is even more than what previously reported for CVD graphene [94]. On the contrary, all the other films show a very little change in the sheet resistance, generally within the error bar. This indicates that the effect of chemical doping with

TFSA is limited to the first graphene layer and that the molecules do not diffuse into the films.

In Fig.2.6 the UV-vis absorption spectra of the films before and after the depositions of TFSA are compared. The spectra of LPE(1) differ for the decrease of the oxidation peak at $\sim 300\ nm$ (see inset in Fig.2.6 for LPE(1)) suggesting an interaction between TFSA and oxygen electron rich defects on graphene. On the other hand, the spectrum of LPE(2) (annealed at low pressure $10^{-6}\ mbar$) is unchanged after the deposition of TFSA.

As for GO films, only the spectrum of GO(1) presents a variation upon chemical doping confirming that the effect is limited to the first layer of graphene. Even in this case the decrease of the peak's intensity in GO(1) could be explained as due the interaction of TFSA with the oxygen groups on the surface of the film. Nevertheless, differently from LPE(1), the spectrum of GO(1) decreases across a range of wavelengths which is larger than the width expected for the $n \rightarrow \pi^*$ transition of $C{=}O$. To explain this it must be considered that graphene oxide is constituted by a wide range of conjugated domains with different sizes [101].

For each conjugated domain the energy of the absorption peak depends on the band gap which in turns decreases with the width of the domain, similarly to what reported for ad-hoc synthesized nanographenes [104]. Only domains that are "large enough "(at least $>\ 3.4\ nm$ based on ref. [104]) show a Dirac point with a zero band gap. Since the spectra are given by the sum of the contributions from every different conjugated domain, the absorption peak of reduced GO is somewhat broader than that of the LPE films as shown in Fig.2.6. In other words, the absorption peak is given by both the Van Hove

singularity of the larger (graphene like) domains and the band gap peaks of the smaller ones. To explain the effect of TFSA it must be considered that the smaller the domain the more it will be affected by the surrounding oxygen atoms. Since TFSA withdraws electron density from oxygen groups at the boundaries of conjugated domains, the smaller domains will be more impoverished of electrons, resulting in a stronger reduction of the absorption contributions at lower wavelengths as shown in inset (A) of Fig.2.6 for GO(1).

The absence of any significant variation in the GO(2) and GO(3) spectra suggests that TFSA involves only the free oxygen groups at the very surface of the film so that the UV-vis absorption is determined by the bulk. It is interesting to note that this also indicates the absence of percolation of the doping agent between the GO layers. A very low affinity between the highly polar TFSA and the graphene flakes is probably the reason for it.

Next, the evolution of the work function (reported in Fig.2.7) was discussed for the highest conductive samples of each type: LPE(2) and GO(3). The work function was measured after every step of the film preparation. The work function obtained for the LPE(2) film after the deposition (5.1 eV) is higher than expected for pristine graphene or graphite (4.4/4.6 eV) based on previous literature and on the calibration of the Kelvin probe that use such references [105, 106]. This was interpreted as caused by the presence of PDI residues in the as deposited film [107] To confirm this it can be considered that both the work function and the UV vis feature of the surfactant (see Fig.2.6 for LPE(2)) decrease drastically after the annealing. The high sheet resistance of the GO films as cast makes it impossible to carry out Kelvin probe measurements before the thermal annealing.
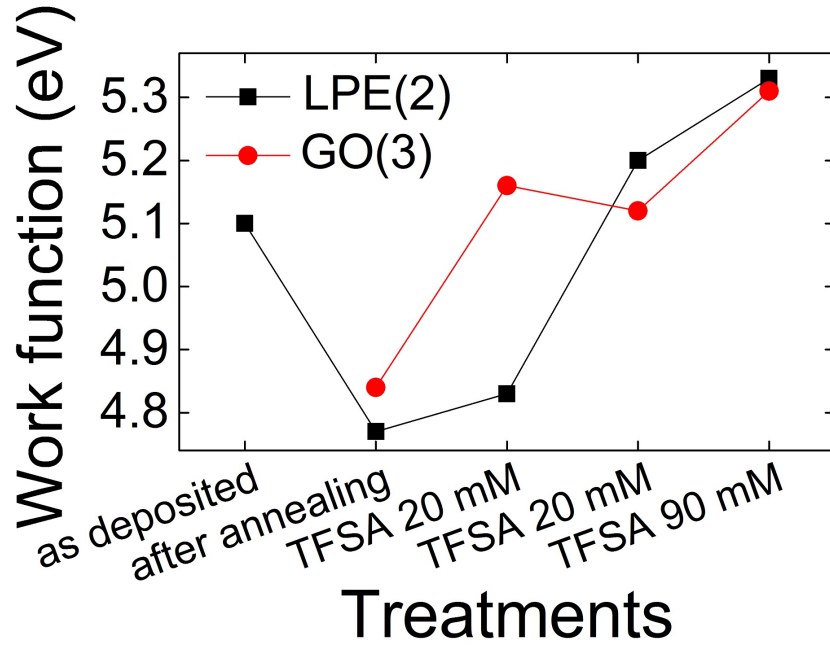
Figure 2.7: Work function values measured after every prepara-
tion step of the samples that showed the highest conductivity.

After the annealing, the two samples show a similar work function around
4.8 eV, slightly higher than the usual range for pristine graphene or graphite
[96, 108]. The presence of oxygen groups in GO and of surfactant residues
in LPE(2) can account for this difference. It is noteworthy that the first
deposition of the less concentrated solution of TFSA (20 mM) raises the
work function of GO(3) film to about 5.1 eV while the value for LPE(2)
remains virtually unchanged. This suggests that the interaction of TFSA
with electron rich oxygen atoms could lead to the deposition of a larger
amount of doping agent. A second deposition (20 mM) brings the work
function of both the samples to a level of $\sim 5.2\ eV$. Then a third deposition
of TFSA (80 mM) increases the work function further to approximately
5.3 eV. The ageing of the doping treatment is reported in Fig.2.8.

98
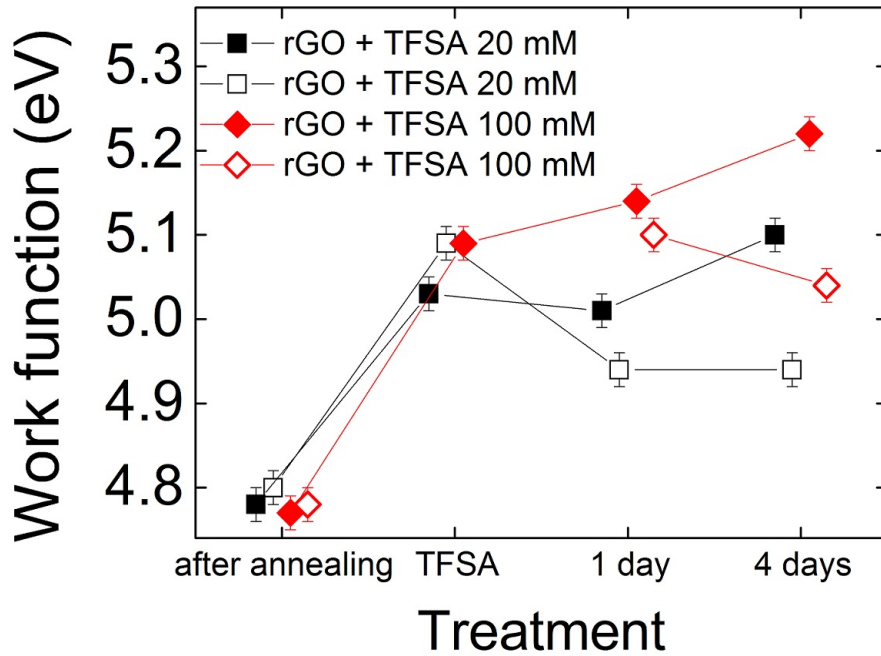
Figure 2.8: Ageing of the doping treatment effect over a period of 4 days after the deposition on samples of reduced graphene oxide with different amounts of TFSA. The samples were kept in nitrogen atmosphere and the work function measurement was carried out in air. Some fluctuations are present in the work function probably due also to the contact with air. However, surprisingly, the general doping effect persists after days even after the samples were exposed to air.

This shows that the work function variation is less than 2 meV over several days of exposure to air. This is extremely encouraging as only a few minutes are required to allow the films to be coated with active layers, in a typical device fabrication process (for either light-emitting diodes (LEDs) or

99

photovoltaic diodes (PVDs)) since it can be expected that the work function will then be frozen in, to a large extent, after depositing the active layer on top of these films [34].

The obtained values are very interesting as they make the tested films good candidates as ITO modifiers possibly replacing PEDOT:PSS for hole injection in organic optoelectronic devices. They also compare well with other promising materials for thin transparent hole-transport films. In particular the values of work function obtained here are higher than those reported for carbon nanotubes both multi-walled and single-walled [109, 110]. The work function of PEDOT:PSS is generally reported to be $\sim 5.2\ eV$ which is also slightly lower than what measured here. Thin films made of silver nanowires (Ag NW) are recently attracting much interest as a promising material for transparent conductive layers as they usually show a sheet resistance of $\sim 7\ \Omega/\square$, comparable with that of ITO. Nevertheless, not only they show a characteristic roughness of several tens of nanometers (rms), but also the work function of silver is $\sim 4.7\ eV$ significantly lower than what obtained here. Ag NW are can be covered with a layer of PEDOT:PSS or graphene to tune the work function [111].

The conductivity of the films under test is still significantly lower compared to ITO. This makes it impossible, at this stage, to produce working devices using these graphene films as transparent electrodes as they give rise to a very high series resistance to the diode. In the case of LPE the investigation of different surfactants could lead to a better exfoliation and more uniform deposition with a lower sheet resistance [98]. As for GO instead a thicker (less transparent) film is needed to increase the conductivity.

2.4 Conclusion

In this work liquid-phase exfoliated (LPE) graphene and graphene oxide (GO) dispersions were prepared using facile and scalable processes. Starting from the liquid dispersions thin transparent films were depostied on fused silica substrates using different methods. The films were characterised in terms of morphology, optical transmission, electrical conductivity and work function. Uniform and continuous layers of GO were obtained with low roughness (rms) of approximately 1 nm by repeated spin-coating depositions from a water dispersion. The thickness of GO films was tuned by few nanometers by varying the number of depositions. Large area ($\sim 1\ cm^2$) thin LPE films were obtained with a continuous network of flakes that allows electrical conductivity via charge percolation.

A relatively low temperature thermal annealing (350/400 $°C$) at low pressure ($10^{-4}/10^{-6}\ mbar$) was proposed is an effective method to increase the conductivity of both GO and LPE films by several orders of magnitude. The sheet resistance in this work was decreased down to $\sim 10^5\ \Omega/\square$ which is comparable to GO reduced with hydrazine vapour and thermal annealing but without using such toxic reactants [70, 67]. The values of sheet resistance are also comparable with values reported in the literature for graphite exfoliated in water to give dispersions of mono- and few-layer graphene stabilized by surfactant [98].The conductivity of the LPE films could be further increased by investigating different surfactants. In the case of GO, the effect of the annealing is a partial restore of the conjugation corresponding to a red shift in the UV-vis spectra. Graphene films were chemically p-doped via the spin-coating deposition of the electron withdrawing molecule TFSA. The

101

effects of this treatment on the optical transmittance, electrical conductivity and the work function of the films were determined. A significant increase of conductivity is obtained only for the single-layer GO film indicating that the effect of the dopant is limited to the first layer of graphene in direct contact with it.

Surprisingly, the data suggest that the presence of oxygen groups on graphene improves the deposition of TFSA on the films without preventing the doping of the graphene lattice. The work function of both GO and LPE films was measured after every step of preparation. Interestingly, the work function of the films were increased by 0.5 eV via the deposition of TFSA, to up to about 5.3 eV which is higher than what reported in the literature for graphene and also for graphene doped with TFSA [105, 96]. This is very interesting also in the context of the use of graphene films as ITO modifier for a better hole-injection in optoelectronic devices. These results are published in the Organic Electronics journal[112].[1]

Chapter 3

Work function of graphene and single-walled carbon nanotubes films on indium tin oxide

In this chapter graphene layers and carbon nanotubes layers deposited from aqueous dispersions were characterised for applications in PLED devices as surface modifiers on top of indium tin oxide (ITO) as an alternative to PEDOT:PSS. The work function of the layers deposited on ITO substrates was measured in air with the Kelvin probe method. The values were than compared with the work function measured using electroabsorption spectroscopy when the layers are in contact with a film of luminescent polymer F8BT inside a working PLED device. The data show a clear difference between the two methods suggesting a reorganisation of the charge distribution at the interface. The results describe an important factor that must be taken into account in the design of opto-electronic devices.

3.1 Introduction

Poly(3,4-ethylenedioxythiophene):poly(styrene sulfonate) (PEDOT:PSS) is commonly used as a thin layer on top of ITO in PLEDs. The transparency and the processability from aqueous solution make PEDOT:PSS an excellent hole-injection layer [113]. Nevertheless, the presence of the acidic sulfonate groups in PSS is also responsible for the progressive degradation of ITO which revels to be detrimental for the life-time of the devices [114].

New materials such as graphene or carbon nanotubes can be processed to form thin layers that could be employed as a substitute of PEDOT:PSS layers thanks to their relatively high transmission of light in a wide range of the visible spectrum, ease of production and relative low reactivity.

The work presented in this chapter studies the electronic properties of such films and how they are affected by the formation of an interface with a conjugated polymer layer in a polymer LED. To this purpose, films of liquid-exfoliated graphene and films of sorted single-walled carbon nanotubes (SWNTs) were deposited on a thin layer of ITO on a glass substrate. In particular two different and complementary methods to measure the work function of the films have been used to compare the electronic properties of the films in different conditions. Both metallic and semiconductor nanotubes sorted via a density gradient ultracentrifugation method have been tested. Even if metallic nanotubes are a more intuitive solution for the production of conductive layers, we also tested semiconductor SWNTs as they can be a good hole transport layer via their valence band.

The work function is the energy of extraction of electrons from a material and it is a surface property. The measurement of this parameter is paramount

during the design of an electronic device as it determines the ability to transfer charge carriers at the interface between two different materials. The work function of the two materials at the interface should be ideally the same to reduce energy barriers.

The work function of the films was measured using both the Kelvin probe method and the electroabsorption spectroscopy. With the Kelvin probe the film is exposed to air whereas the electroabsorption technique measures the work function of the films when they are inside a PLED. The comparison of the two measurements allowed to study the effect of the formation of an interface between the buffer films and the active layer inside a polymer LED.

3.2 Experimental details

3.2.1 Preparation of the thin films

Liquid phase exfoliated graphene was prepared by sonicating graphite powder in water ($12 \ g \ L^{-1}$) after the addition of the surfactant sodium deoxycholate (SDC) at a concentration of $5 \ g \ L^{-1}$ for approximately 3 hours. The dispersion is decanted for 10 minunte after the sonication and the precipitate, composed of bigger aggregates, is removed. The dispersion is then centrifuged for an hour at $10,000 \ rpm$ ($17,000 \ g$) and the top 70% is used as the final dispersion.

Single-walled CNTs were sorted based on their size and chirality with density gradient ultracentrifugation (DGU) from water solutions of metallic and semiconducting single-walled carbon nanotubes using SDC as a surfactant [115, 116]. CoMoCAT SWNTs were added ($0.2 \ g \ L^{-1}$) to a water solution of

SDC (20 g L^{-1}). The mixture is treated in a 200 W, 20 kHz sonicator bath at 15 °C for 90 minutes. Large insoluble nanotubes bundles were removed via ultracentrifugation at 50,000 rpm (173,000 g) for 2 hours. The supernatant is then extracted and used for DGU.

The separation between metallic and semiconductor nanotubes is obtained using a mixture of two surfactants that adsorb differently on the two types of SWNTs. For this purpose, the dispersion obtained with the ultracentrifugation is diluted with a solution containing 0.4% w/w of sodium cholate and and 1.6% w/w of sodium dodecyl sufate. A linear density gradient was obtained using the density gradient medium Otiprep: a solution of iodixanol in water (60% w/w). Subsequent layers of progressively more diluted Otiprep were stacked to form a step gradient. The nanotubes dispersion is place in between two of the layers. Via diffusion of the different density layer and the dispersion of nanotubes to be sorted, a linear gradient is formed. The ultracentrifugation is carried out fo 12 hours at 40,000 rpm (250,000 g) at a temperature of 15 °C using a swinging rotor centrifuge. The aliquotes containing the different fractions are extracted using a syringe pump.

Both graphene and SWNTs water dispersions are deposited as thin layers on top of ITO covered glass substrates using the vacuum filtration and transfer method described in chapter 2 section 2.2.2. The dispersions are vacuum filtrated through cellulose filters to form a layer only few tens of nanometres thick. The surfactants are washed away with deionised water washes. After the filter and the film are dry, pieces of the desired shape are cut and transferred on top of the target substrate with the thin film facing on the substrate surface. The adhesion of between the two surfaces is improved using a drop

of dichlorobenzene. The samples are the immersed in acetone overnight to dissolve the cellulose filters followed by further washes in isopropanol and dionised water.

Four samples constituted of a graphene films deposited on ITO were prepared following an identical procedure. These samples are identified with the letters G1, G2, G3 and G4. Two identical films made of metallic SWNTs (m-CNT1 and m-CNT2) and two identical films made of semiconductor SWNTs (sc-CNT1 and sc-CNT2) were prepared. The carbon-based materials and the films were prepared by the Nanomaterials and Spectroscopy (NMS) group at the Department of Engineering, University of Cambridge [116].

3.2.2 Kelvin Probe

The Kelvin probe method measures the contact potential difference (c.p.d.) between the surfaces of two conductive materials. It is based on the measurement of the capacitive current generated by periodically varying the distance between the two surfaces with a certain frequency. An external voltage equal and opposite to the c.p.d. is then needed to set the capacitive current to zero. Fig. 3.1 shows the schematic of the Kelvin probe measurement apparatus.

By subtracting the work function of one of the two electrodes to the c.p.d. is possible to obtain the work function of the other electrode. The Kelvin Probe (KP) is an indirect measurement of the work function of the surface of a conducting material with respect to a reference material. Freshly cleaved HOPG was used as reference in air with a work function of $4.475 \pm 0.005 \; eV$ [106]. All measurements were performed in air.
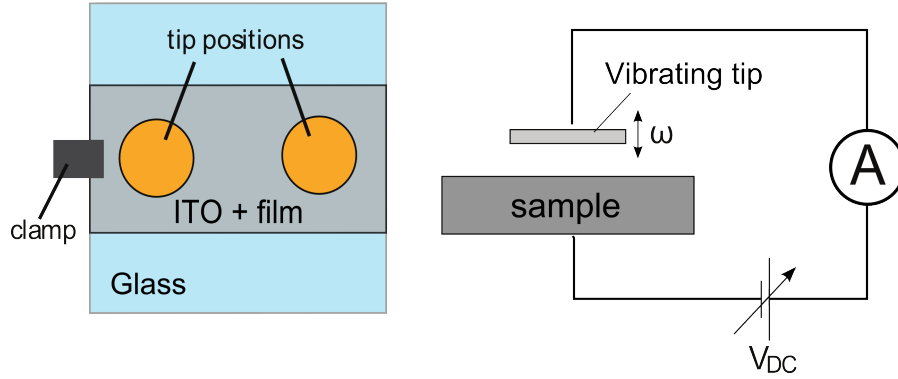
Figure 3.1: On the right the geometry of the two possible locations of the probe on the sample are illustrated. The picture on the left show the electrical schematic of the Kelvin probe measurement apparatus: the capacitive current generated by the vibration of the probe at close distance on the sample is set to zero by the variable voltage bias. The DC bias is then equal to the contact potential difference between the probe and the sample surfaces.

3.2.3 Electroabsorption spectroscopy

The electroabsorption signal $(\Delta T/T)$ is the ratio of the intensity of the light transmitted through the sample (T) and the modulation of that intensity (ΔT) due to an applied alternating electric field. The typical electric fields applied in EA experiments $(\sim 10^5 \ V cm^{-1})$ are such that the ΔT signal is of the order of $\sim 10^{-4}/10^{-5}$ times the transmitted intensity and hence a lock-in technique is required for the detection of ΔT. All measurements were carried out at room temperature by irradiating the sample with a monochromated beam from a Xe-lamp while applying a sinusoidal voltage $V_{AC} = 1 \ V$ at a frequency $f = 2 \ kHz$. A schematic of the electroabsorption (EA) setup is

110

shown in Fig. 3.2.
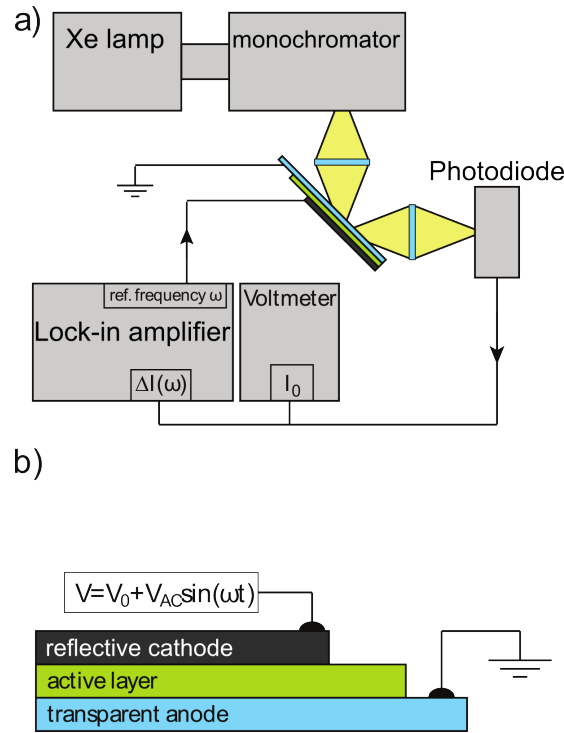
Figure 3.2: Schematic of the electroabsorption set-up used in this study (a) and scheme of a device for electroabsorption and how it is driven (b).

The monochromated and collimated beam coming out from the monochromator is focused on the pixel of interest, it passes through the anode and the active layer, is then reflected on the metallic cathode and emerging from the active layer and the anode is eventually detected by a photodetector. The alignment of the system is done in two steps: the different parts of the instrument were arranged first in order to maximize the average intensity of the transmitted light measured by the photodetector. In a second step the beam on the pixel of interest was focussed by maximizing the amplitude of

the alternate signal that is modulated at the same frequency f of the applied alternate voltage V_{AC}. This also allowed to set to zero the phase difference between the signal and the lock-in amplifier's reference frequency.

The charge density ρ in the polymeric active layer can be assumed low enough that the electric field across the bulk of the film can be considered uniform and thus [117]

$$F = \frac{V}{d} \tag{3.1}$$

$$F_0 + F_{AC}\sin(\omega t) = \frac{V_0 + V_{AC}\sin(\omega t)}{d}. \tag{3.2}$$

In these hypothesis, given that the EA signal is proportional to the squared electric field, the first harmonic of the EA signal, $EA(1\omega)$, can be written as [118]

$$\Delta T/T(h\nu, 1\omega) \propto \chi(h\nu)V_0 V_{AC}\sin(\omega t) \tag{3.3}$$

where ω and V_{AC} are the angular frequency and the amplitude, respectively, of the AC voltage. V_0 is the electrostatic potential across the absorbing layer and it is the sum of the applied DC voltage V_{DC} and the built-in potential V_{BI}

$$\Delta T/T(h\nu, 1\omega) \propto \chi(h\nu)(V_{DC} - V_{BI})V_{AC}\sin(\omega t) \tag{3.4}$$

it is therefore possible to deduce V_{BI} by extracting the applied DC voltage (V_{null}) needed to set $\Delta T/T(h\nu, 1\omega)$ equal to 0.

3.2.4 Devices preparation for the electroabsorption measurement

The devices are prepared by spin coating (1800 rpm for 120 sec under N_2 atmosphere) a solution 2% w/w in toluene of the polymer F8BT (poly[(9,9-di-

n-octylfluorenyl-2,7-diyl)-alt-(benzo[2,1,3]thiadiazol-4,8-diyl)]) (see Fig. 3.3) with a M_W of 73000 $g\ mol^{-1}$ obtaining a film approximately 100 nm thick.
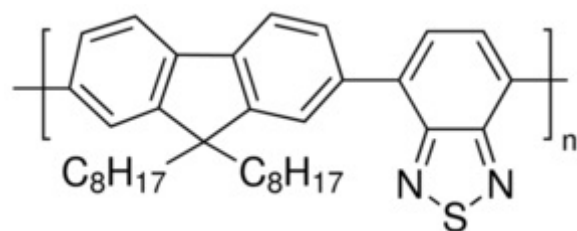
Figure 3.3: Molecular structure of the photoluminescent polymer F8BT.

A metallic calcium cathode 30 nm thick is evaporated on the active layer and is subsequently covered with a layer of 150 nm of aluminium. A schematic of the devices is described in Fig. 3.4.
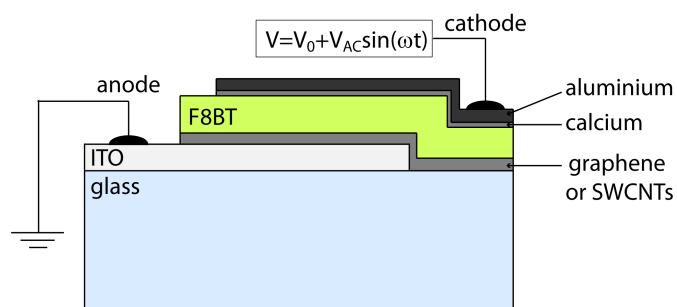
Figure 3.4: Schematic of a device for electroabsorption spectroscopy.

3.3 Results and discussion

In Fig. 3.5 the work function values of the thin layers as measured with the Kelvin probe method are reported. Since the golden probe does not probe exactly the middle of the substrate, the average between the two sides is reported for each sample. The uncertainty associated with the measured values was estimated as the standard deviation of 5 repeated measurements on both side. The uncertainty cannot be lower than the instrumental error of $0.02 \ eV$. Fig. 3.5 reports the work functions measured with KP. The deposition of the films was carried out in air at room temperature.

For every sample the $EA(1\omega)$ spectrum was acquired in the wavelength range from $650 \ nm$ to $320 \ nm$ ($1.91 \ eV$ to $3.87 \ eV$) where the active layer F8BT has its main absorption peak. The scan was always done from high to low wavelength. In all the spectra the scan step is $2 \ nm$. An example of an electroabsorption spectrum is reported in Fig. 3.6.

Then the $EA(1\omega)$ was measured as a function of V_{DC} at a wavelength $10 \ nm$ higher than that of the most intense peak in the EA spectrum. This is done in order to avoid the absorption peak of the polymer and to find the best compromise between high sensitivity and low absorbance of light. In fact, a high absorption condition may generate significant PL and may also increase the charge density in the active layer. The V_{DC} was scanned between $-2.0 \ V$ and $+1.5 \ V$ with scan steps of $0.1 \ V$. Each point was obtained by the average of 4 measured values. Then the data was fitted in the range of reverse bias ($V_{DC} < 0$) between $-1.5 \ V$ and $0.0 \ V$ in order to avoid any deviation from the linearity due to dark currents across the polymer layer or to the emission of light at the turning on of the pixel.
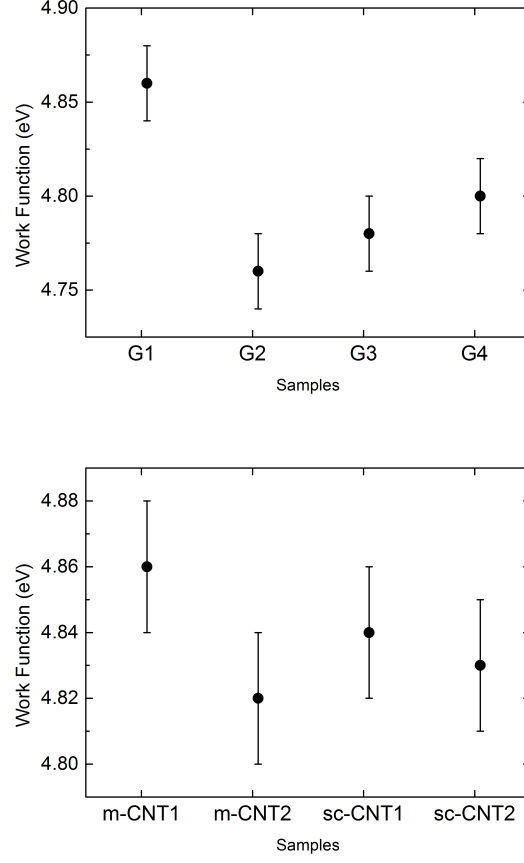
Figure 3.5: Work functions values of Graphene (A) and of metallic and semiconducting SWNTs (B) deposited with the filtration and transfer method on a layer of ITO (150 nm thick) on a glass slide.

The V_{BI} is obtained as

$$V_{BI} = -\frac{m}{q} \qquad (3.5)$$

where m and q are the parameters of the linear fitting function

$$EA(1\omega) = mV_{DC} + q. \qquad (3.6)$$

The V_{BI} values are obtained as the average between three repeated voltage scans and the errors are estimated as the standard deviation of the three
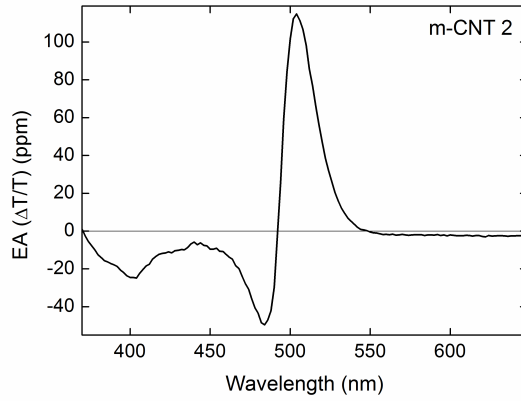
Figure 3.6: Electroabsorption spectrum of a sample of metallic SWNTs deposited on ITO by means of filtration and transfer method (in particular this is m-CNT2). The spectrum is acquired with a scan step of 2 nm. Each point is the average of 6 measured values.

values.
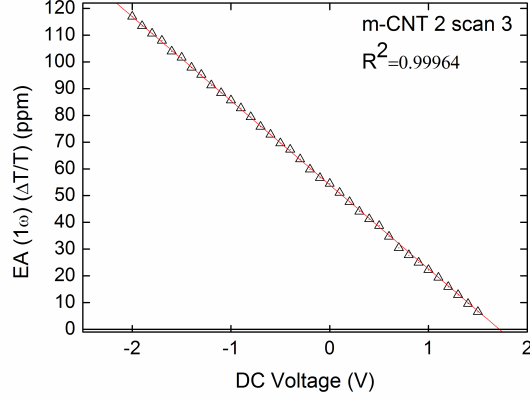
Figure 3.7: Voltage scan of a sample of metallic SWNTs deposited on ITO by means of a filtration and transfer method (in particular this is m-CNT1). The scan is acquired with a scan step of 0.1 V, each point is the average of 4 measured values.

The work functions of the electrodes can be obtained from the measured built-in voltages values. The Schottky model has been demonstrated to provide a good description of the energy line up between a metal and a conjugated polymer semiconductor [93, 36, 38]. In the case of reverse to weak forward bias regime the space charge inside the polymer layer is small enough that the electric field can be considered uniform and hence the built-in potential V_{BI} in the metal-polymer-metal structure can be considered equal to the difference in the work functions of the two metal contacts

$$V_{BI} = \frac{\Delta\phi}{e} = \frac{\phi(anode) - \phi(cathode)}{e} \qquad (3.7)$$

for this reason is possible to obtain the work function value of one of the electrodes when that of the other one is already known.

The work function of the cathode (calcium) is pinned by the LUMO of

117

the polymer layer for it has lower energy with respect to the work function of calcium [36, 37, 39, 40]. Therefore the V_{BI} is determined by the difference between the LUMO and the work function of the anode under test. The energy of the LUMO level was determined to be $-3.3\ eV$ for the batch of F8BT polymer used (Dr. Charlotte Fléchon unpublished data). This value has been obtained as the difference between the energy of the HOMO, calculated from the oxidation peak energy of a cyclic voltammetry experiment, and the band gap energy defined as the lowest energy peak of UV-visible absorption spectra of the polymer [119].

The work functions obtained using this method are reported in Fig. 3.8. The error bar associated with the work functions measured via EA is given by the linear fitting of the voltage scan.
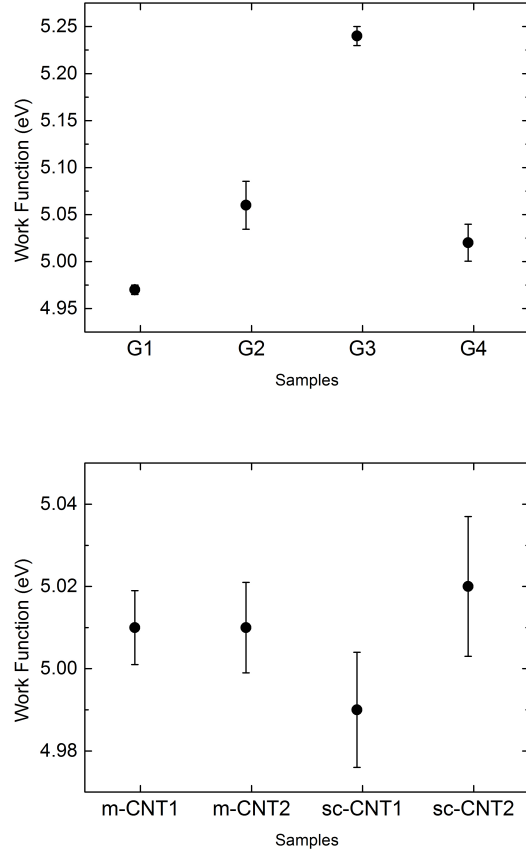
Figure 3.8: Work function values of the samples with the graphene film (A) and carbon nanotubes film (B) deposited on ITO measured with the electroabsorption method and with Kelvin probe.

In Fig. 3.9 the work function values measured for all the samples are compared. The values measured for reference samples with only ITO are also reported.

The work function values of the metallic and of the semiconductor SWNTs are very close to each other, both with Kelvin probe and with EA. A similar work function value for metallic and semiconductor SWNTs has been
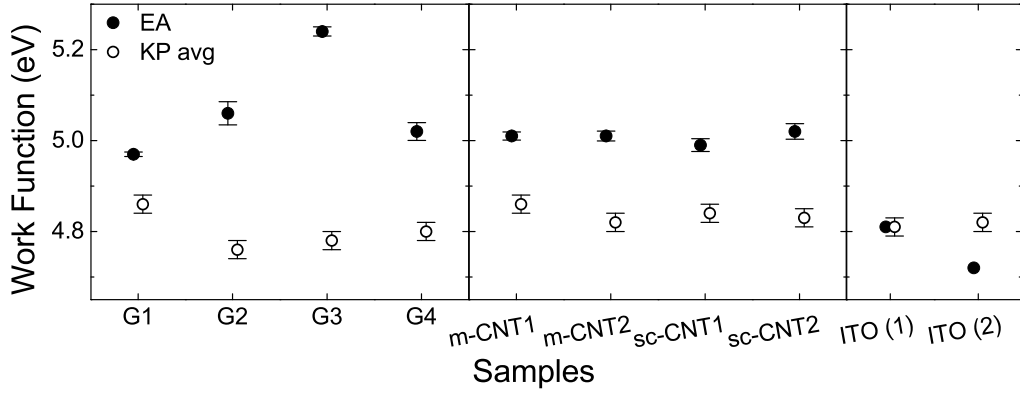
Figure 3.9: In this figure all the work function values measured both with kelvin probe and electroabsorption are compared. Reference values measured on ITO substrates are also reported.

reported in the literature for diameters above $\sim 1\ nm$ [120, 121]. In the case of smaller diameters these results could be explained as due to unwanted doping of the semiconductor SWNTs via charge transfer form the ITO surface to some localised inter-bandgap states [122]. This effect needs to be investigated further and a possible experiment could involve the deposition of the semiconductor SWNTs layers on an insulating substrate to avoid charge transfer doping.

The work function of the reference samples of ITO covered with F8BT measured via electroabsorption is equal or lower than that measured in air with the Kelvin probe method. This result is consistent with the previous literature [34]. It is very interesting to note, instead, that for all samples containing graphene or carbon nanotubes films the values of work function measured with electroabsorption are always higher than those measured with Kelvin probe.

The data suggests a possible reorganization of the charge distribution

during the formation of an interface between the carbon-based films and the polymer. The fact that this difference disappears on samples without graphene and CNTs (see reference ITO samples) suggest this effect is genuine.

3.4 Conclusions

In this chapter the work function values of graphene and of SWNT semitransparent layers deposited on top of ITO as surface modifiers were determined. In particular an increase of the work function was reported after the deposition of a layer of conjugated polymer F8BT. This increase was determined comparing the work function of the bare films in air measured using the Kelvin probe method and the work function of the same films inside a PLED device obtained from the built-in voltage measured via electroabsorption.

As a reference, the same comparison was reported for the case of two ITO surfaces without graphene and CNT films showing no increase of the work function between Kelvin probe and electroabsorption. The results suggest a reorganisation of the charge at the interface between the graphene or SWNTs layer and the conjugated polymer. The formation of an interface dipole can be also taken into account.

The results reported in this chapter are very interesting for the development of carbon-based films as buffer layers in opto-electronic devices. The modulation of the work function can have a crucial impact on the correct functioning of the devices. These first results suggest that the electronic effects during to the formation of an interface between conjugated polymers and graphene or CNTs films need to be further investigated to use such promising materials in working optoelectronic devices.

Chapter 4

Molecular packing effects on the speed of polymer light emitting diodes

In recent years, for the first time, polymer light-emitting diodes (PLEDs) have been applied as signal transmission devices in visible light communications (VLC). The response speed of the devices is one of the most important characteristics of LED for their use in communications. In this work, a detailed analysis of the parameters that affect the response speed of PLEDs is proposed showing that the low pass filter generated by the relatively large capacitance of the planar electrodes in thin film devices is not always the limiting factor in the on-off switching speed. In particular, using an emissive layer of poly[2-methoxy-5(3',7'-dimethyloctylocy)-1,4-phenilenevinylene] (MDMO-PPV), a processing treatment for the production of PLEDs was demonstrated to increase their response speed by more than two times, from $\sim 116\ kHz$ up

to ~ 260kHz. The treatment is based on the thermal annealing of the devices before the evaporation of the metallic cathode. The mechanism underlying this process was investigated via a structural, electrical and photophysical characterization of the polymer layer at different annealing temperatures: 80°C, 100°C and 150 °C. Surprisingly, even if the thermal treatment increases the crystallinity of the polymer layer, the mobility drops significantly. However, the thin film transistor threshold voltage follows the same trend as the device bandwidth, and they can be explained with the presence of lower band gap crystalline domains. The increase in the speed of the devices can be explained taking into account a trap-assisted injection model. The variation in the energy distribution is also seen in the absorption spectra. The PL spectra show the comparison of an excimer emission after annealing due to the more interacting molecules in the crystalline domains. An interpretation to the variation of the PL peaks intensity based on the increase in the crystallinity of MDMO-PPV is described also showing a clear analogy in the PL variation between the thin films upon annealing and the polymer solution at increasing concentration.

4.1 Introduction

The main strengths of polymer light-emitting diodes (PLEDs) include reduced production costs, large photoactive areas, increased colour contrast and lightweight, robust and flexible devices. The most promising applications are (i) new displays technology, thanks to higher colour contrast, lower power consumption and larger viewing angle with respect to LCDs or (ii) as innovative solid-state lighting devices in the form of large photoactive area

124

light-emitting tiles, wearable flexible lightings or printable LEDs, to give several examples.

In recent years, the first reports on the use of PLEDs as transmission devices in visible light communication (VLC) technology have emerged in [123, 124, 12, 15, 13]. VLC is a new access network developed over the last decade [125, 126, 127, 10] and is based on the intensity modulation of visible light at high speeds that are imperceptible to the human eye. The most common modulation format used in VLC is on-off keying (OOK) modulation for signal transmission while the device is being simultaneously driven as a normal light source with a DC bias. VLC was developed as an alternative wireless communications method to traditional radio frequency methods such as Wi-Fi also motivated by the problems due to the highly congested radio frequency spectrum with premium license fees [128]. The use of the visible part of the electromagnetic spectrum presents a good integration with existing infrastructures for a new range of possibilities including indoor localization systems, underwater communications, and vehicle to vehicle communications for intelligent transport systems (ITS). VLC can be used for wireless communications in situations where RF interferences are a serious problem such as on commercial flights or in hospitals where radio wave links can disrupt life support equipment [129].

Interestingly, the use of organic semiconductor based light sources for VLC poses a number of significant challenges that must be addressed in order to compete with the more established inorganic semiconductor technologies. The key challenge is related to (i) the relatively low charge carrier mobility in organic semiconductors and (ii) the increased number of charge

carrier traps in comparison with the more crystalline inorganic semiconductors. The combination of these two effects causes a significant decrease in the response speed of PLED devices which in turn reduces the available transmission speed [124]. A further fundamental limit present in the on-off switching speed of PLEDs is caused by the common geometry of the devices where a thin film (generally $\sim 100\ nm$) of polymeric active layer is enclosed between two metallic electrodes with lateral dimensions in the order of several millimetres squared or larger (in any case much higher than the thickness). This geometry results in a significant capacitance, which, together with the intrinsic series resistance, gives rise to a low pass filter (LPF) characteristic transfer function. The cut off frequency of such a LPF is lower for large area devices due to a higher capacitance, thus, limiting the speed of light intensity modulation [123].

This work, however, demonstrates, for the first time that, even for relatively large area devices of $\sim 3\ mm^2$ the response speed is actually limited by the charge transport processes involved in the electroluminescent emission. Most importantly, also a low cost and easily scalable thermal treatment to increase the speed of PLEDs by more than two times is demonstrated for the first time. The underlying mechanism in this process was investigated confirming a strong relation between the molecular organization in the active layer and the response speed of the devices. In particular, the data show that the charge injection constitute a more determinant step to the device speed than the charge carrier mobility.

Unexpectedly, however, this work demonstrates that the increase in crystallinity of the polymer layer upon annealing results in the formation of

localized trap states that enhance the charge injection from the electrode by a trap assisted injection mechanism described in the literature [130, 131]. The peak fitting of the photoluminescence emission spectra of the polymer, both in film and in solution, confirmed the results and revealed an interesting vibronic structure evolution upon thermal annealing. The data shows that the polymer molecules deposited in the film 'freeze' in an amorphous state with very little electronic interaction between contiguous chromophore groups that behave as in a diluted solution. The annealing process instead promotes molecular rearrangement of the film with the formation of highly ordered domains where molecules are affected by a different electronic environment.

4.2   Experimental

4.2.1   Device preparation

A series of encapsulated PLEDs were prepared with an annealing treatment of the polymer active layer at increasing temperatures. For the production of the devices, a glass substrate covered with a patterned film of indium tin oxide (ITO) as the transparent anode (Ossila s103) was used. The ITO was deposited via sputtering to obtain a uniform layer about 110 nm thick. The anode surface was cleaned by sonication for 10 minutes in acetone and then for 10 minutes in isopropanol. It was followed by an oxygen plasma treatment for 10 minutes to remove any organic impurities, modify the surface morphology and improve the charge transport [35]. The treatment also temporarily increases the work function [34].

Immediately after the oxygen plasma, a 30 nm thick film of poly(3,4 ethylene dioxythiophene): poly(styrene sulphonate) (PEDOT:PSS) was deposited as a hole injection layer via spin coating (100 μL at 4000 rpm for 120 s followed by 5000 rpm for 10 s) from a water solution (Sigma-Aldrich) after filtration. After the deposition, the samples were immediately annealed at 180 $°C$ under nitrogen atmosphere to remove any water residues that can be detrimental to the lifetime of the device. All the remaining steps of the preparation in nitrogen atmosphere were carried out to avoid the presence of oxygen and water molecules inside the devices.

A layer of the emissive polymer poly[2-methoxy-5(3',7'-dimethyloctyl-oxy)-1,4-phenylenevinylene] (MDMO PPV) (Sigma-Aldrich 546461) ($Mn \sim$ 120000) was deposited via spin coating (80 μL at 1500 rpm for 60 s and 4000 rpm for 10 s) from a 0.5% w/w solution in toluene (4.33 $mg\ mL^{-1}$). To remove any large aggregates the polymer solution was filtered with a polytetrafluoroethylene syringe filter (0.45 μm pore size). The resulting film has a thickness of about 50 nm.

The samples were thermally annealed on a hot plate for 10 minutes in a nitrogen atmosphere and then cooled down to $\sim$ 30 $°C$ at a rate of approximately 2 $°C\ min^{-1}$ to let the polymer chain slowly rearrange towards a more ordered structure. The glass transition temperature of MDMO-PPV is about 50 $°C$ [132]. In order to study the effect of the annealing process three different annealing temperatures were used: 80 $°C$, 100 $°C$ and 150 $°C$. A reference sample with no annealing treatment was also prepared.

Subsequently, a metallic calcium cathode (30 nm) was deposited on top of the emissive layer via thermal evaporation in a high vacuum ($10^{-6}\ mbar$)

before covering it with a protective 120 nm thick aluminium layer.

The devices were encapsulated to protect them from contact with water and oxygen and to be able to use them in air, as mentioned. For the encapsulation, a drop of epoxy glue (Ossila) was deposited before a glass slide was placed on top to form a thin sealing film to cover the whole device. The glue was hardened by curing in UV light under nitrogen atmosphere and added metallic contact pins to the finished device as shown in Fig. 4.1.

The devices are composed of six independent pixels with an active area of 3 mm^2. To protect the calcium cathode from any exposure to air it was connected with the external pins via an ITO trace (see Fig. 4.1c). The encapsulation extends the lifetime of the device but, on the other hand, it increases its internal series resistance because the ITO resistivity ($\sim 4 \times 10^6 \ \Omega \ m$ [32]) is higher than the typical resistivity for a metal ($\sim 10^{-8} \ \Omega \ m$).

The J-V characteristics of the LEDs were determined by measuring the DC current density versus voltage with a Keithley 2400 source measure unit. The luminance versus voltage (L-V characteristics) was characterised also by using a calibrated silicon photodetector (with known responsivity) and a Keithley 2000 multi-meter.

The electroluminescence emission spectra of the devices was measured by using an Andor spectrophotometer (Shamrock 163 spectrograph with an Andor Newton EMCCD camera).

4.2.2 Dynamic response of the PLEDs

In this work, the effect of the annealing of the active layer on the on/off switching speed of the PLEDs was investigated. For this purpose, the band-
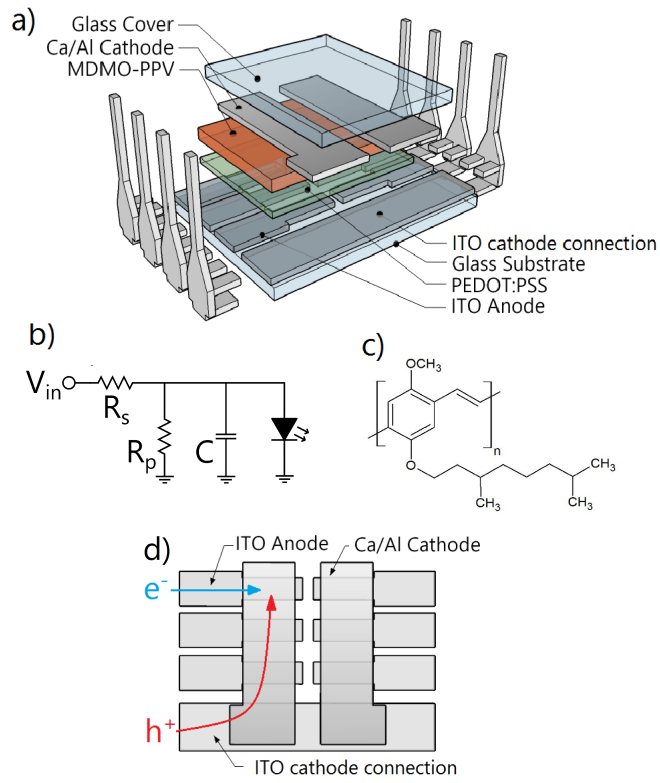
Figure 4.1: The device schematic (a), the device equivalent circuit (b), the molecular structure of MDMO-PPV (c) and the geometry of the contacts (d). In the equivalent circuit (b) the RS is the series resistance, the RP is the parallel resistance and C is the capacitance. In figure (d) the arrows describe the direction of electrons and holes along the electrodes to reach the active area.

width was determined by reporting the Bode plots of the devices (thanks to Dr. Paul Haigh for helping in the measurements).

To avoid clipping and non linear impairments to the transmitted signals, the PLEDs were driven with a sinusoidal AC current $I(t) = I_{bias} + I_{pp} \cdot \sin(\omega t)$ where $\omega = 2\pi f$. The current amplitude (peak to peak current I_{pp}) was increased within the linear range of the L-I characteristics from 0.5 mA to

4.5 mA (see Fig. 4.2). The current bias (I_{bias}) were also increased accordingly, in order to keep the current troughs always above 0.5 mA.

To avoid empting the charge carrier traps inside the polymer layer and enabling a higher turn on speed of the devices [133, 134]. A Tektronix AFG2022B arbitrary function generator (AFG), an Agilent MXA N9010A electrical spectral analyser and a current mirror circuit adopted from [135] were used to drive the LEDs.
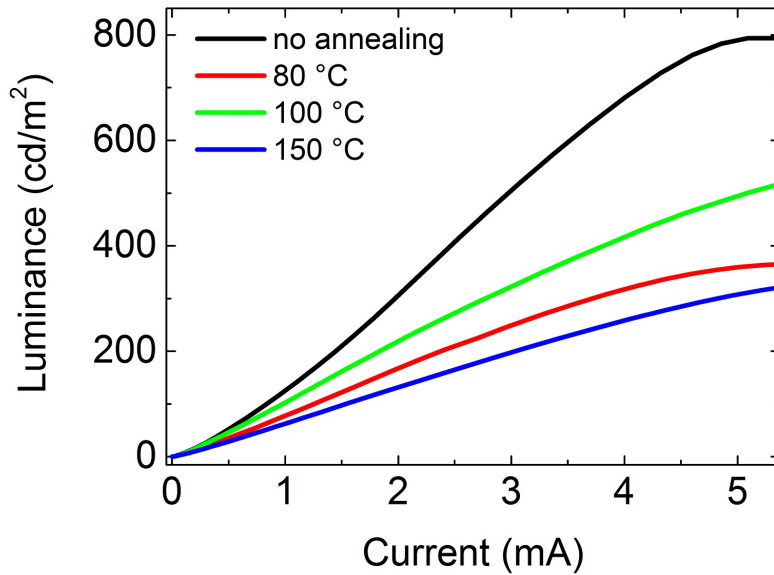
Figure 4.2: Luminance vs Current (L-I) characteristics of the PLEDs prepared with different annealing temperatures.

4.2.3 XRD characterization

The X-ray diffraction (XRD) spectrum of the polymer layer was measured in order to characterise the variation of the crystallinity upon each annealing treatment (thanks to Giuseppe Paternó for helping in the measurements).

Silicon substrates 1×1 cm^2 covered with a 230 nm layer of silicon oxide were used. The substrates were cleaned by sonication in acetone and in isopropanol for 15 minutes.

Layers of ~ 45 nm thick were obtained by spin coating 100 μL of a filtrated polymer solution (see above) (1500 rpm for 60 s followed by 4000 rpm for 10 s). The films were annealed for 10 minutes at the temperatures of 80 $°C$, 100 $°C$ and 150 $°C$ followed by slow cooling as described above. Both spin coating and annealing were carried out under inert atmosphere. For the XRD measurement a Rigaku Smartlab was used in a grazing angle configuration with $\omega = 0.5°$ and $\theta = 0° \rightarrow 35°$ scans.

4.2.4   Thin film transistors

Thin film transistors (TFT) were prepared to characterize the charge transport properties of MDMO-PPV thin films and how they are affected by the thermal annealing treatment (thanks to Ludovica Intilla for helping in the measurements). Bottom gate bottom contact configuration substrates were used with a size of 1.5×1.5 cm^2, n-doped silicon as gate electrode, silicon oxide (230 nm) dielectric and gold/ITO interdigitated source/drain contacts with a channel length of 5 μm. Polymer layers of ~ 45 nm thickness were prepared via spin coating of 80 μL of the 0.5% solution after filtration at 1500 rpm for 60 s and 4000 rpm for 10 s. The samples were annealed at 80 $°C$, 100 $°C$ and 150 $°C$ followed by slow cooling as described above. Both spin coating and thermal annealing were carried out under nitrogen atmosphere. The TFTs were characterised using a PM5 probe station (Cascade Microtech) under a nitrogen atmosphere controlled with a HP 4145B Semi-

conductor Parameter Analyzer.

4.2.5 Photo-physical characterisation

For the photophysical characterization of the MDMO PPV polymer films, $1.2 \times 1.2\ cm^2$ quartz substrates were used. The films were prepared via spin coating of 80 μL of a 0.5% w/w solution of MDMO-PPV in toluene after filtration as described above (1500 rpm for 60 s and 4000 rpm for 10 s). The absorption spectra were obtained with an Agilent UV vis NIR spectrophotometer. The PL spectra were recorded using an Andor spectrophotometer. To study the time resolved emission in the nanosecond regime a Time Correlated Single Photon Counting (TCSPC) spectrometer (Edinburgh Instruments) was used (thanks to Dr. Giulia Tregnago for helping in the measurements). The PL emission was also measured for MDMO-PPV in solution at different concentrations obtained by increasing dilution of a 0.5% w/w solution in toluene (4.33 $mg\ mL^{-1}$) after filtration with a PTFE filter (0.45 μm pore size). The concentration of the solution was progressively decreased by diluting $1:2$ for 8 times down to a concentration of $\sim 4\ \mu g\ mL^{-1}$.

4.3 Results and discussion

4.3.1 PLEDs electrical characterization

The Fig. 4.3 shows the JLV characteristics for the devices with the 4 different annealing treatments. The devices turn on at $\sim 2\ V$ corresponding to a current density of about 1 $mA\ cm^{-2}$. The dark current of the devices varies within three orders of magnitude in the four devices prepared with

different thermal annealing treatments, suggesting a variation in the charge carrier transport due to a molecular reorganization of the active layer. The current onset for the annealed devices appears to start at lower voltage than the non-annealed device, likely indicating an increase in the charge injection. Furthermore, the luminance of the annealed devices decreases with the annealing temperature, probably due to the formation of excimer that quench the electroluminescence emission (EL) [136]. The normalised electroluminescence emission spectra are reported in Fig. 4.4. The spectra show a clear red shift of the peak at lower wavelengths upon annealing, together with the progressive inversion in the intensity of the two main peaks and the progressive increase of a broader tail at higher wavelengths.
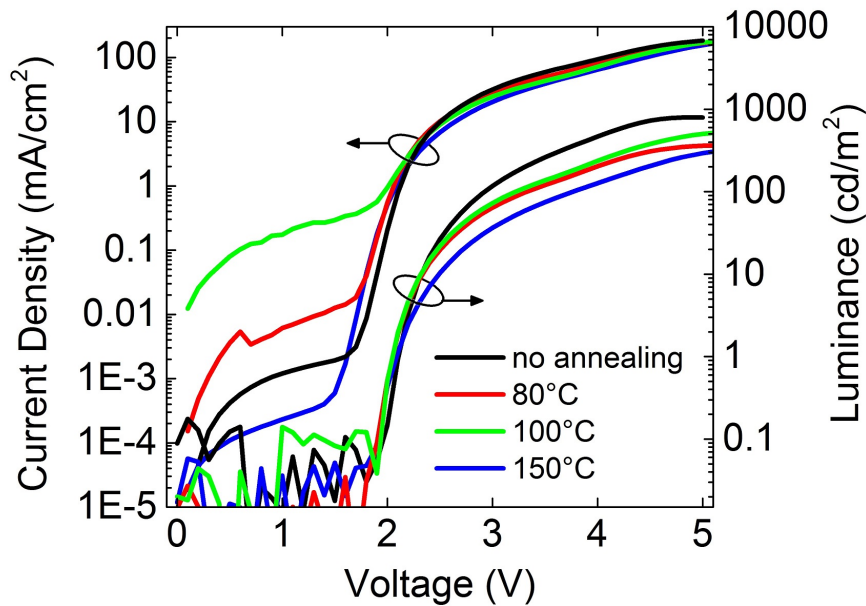
Figure 4.3: Current density and Luminance vs Voltage (JLV) characteristics of the PLEDs prepared with different annealing temperatures.
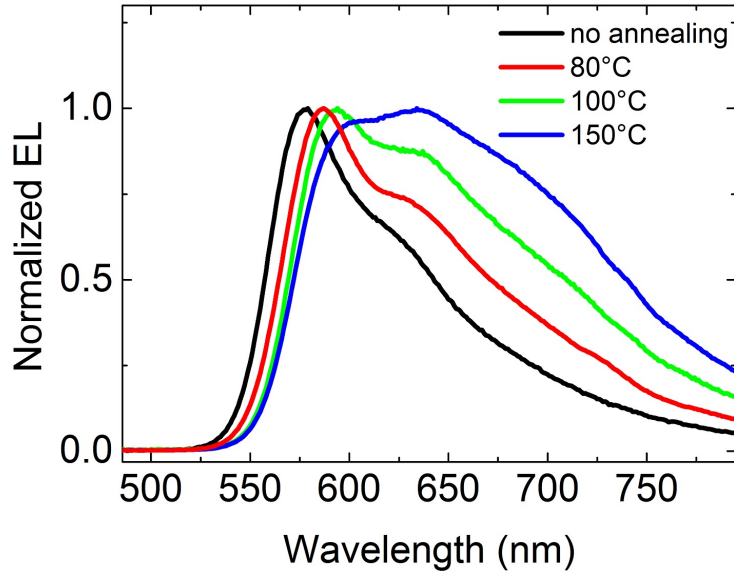
Figure 4.4: Electroluminescence (EL) emission spectra (normalized) of the PLEDs prepared with different annealing temperatures. The spectra were acquired at a bias voltage of 4.5 V.

These effects are reported in the literature as due to a structural reorganization of the polymer chains [132]. In particular, the red shift of the PL onset at low wavelengths indicates a possible bathochromic effect of the increased π-stacking interaction for the formation of crystalline domains, as a consequence of the annealing process, with a lower HOMO-LUMO gap [137].

4.3.2   Device bandwidth

In this work, PLEDs were studied as transmitter devices for applications in VLC technology. For this purpose, the investigation focuses particularly on increasing the dynamic response of the devices thus increasing their response speed to allow higher transmission rates.

All PLEDs are characterized by a particular structure where a low electrical permittivity thin film is enclosed between metallic plates as the two electrodes. The equivalent circuit representation of such devices (reported in Fig. 4.1b) shows an electronic RC LPF structure that attenuates the AC input above a $-3\ dB$ cut off frequency (f_c).

The transfer function $H(f)$ of an LPF, defined as the output to input ratio of the signal intensity, is generally reported in a Bode plot with dB-log scale. It is characterised by a flat passband shape low ripple at low frequencies followed by a fast attenuation ($\sim 20\ dB/decade$) above f_c defined as $20\log(H(f_c)) = -3\ dB$. For a LPF, the cut off frequency is given by $f_c = \tau^{-1} = (R_sC)^{-1}$ where R_s is the series resistance and C is the capacitance. Organic electronic devices have a relatively large intrinsic capacitance given by

$$C = \epsilon_0\epsilon_r A/d \qquad (4.1)$$

where ϵ_0 is the vacuum permittivity, ϵ_r is the relative permittivity of the polymer layer with thickness d and A is the photoactive area of the device.

A capacitance of about 1.6 nF was estimated for the devices considering a dielectric constant ϵ_r of about 3 for the polymer semiconductor [138], a thickness d of about $\sim 50\ nm$ and an area of about 3 mm^2 (the electrical permittivity in vacuum being $\epsilon_0 = 8.85 \times 10^{-12}\ F\ m^{-1}$).

The series resistance R_s is given by the contacts and wirings. The main contribution is due to the ITO connections both at the anode and at the cathode side and the resistance of the metal wirings can be considered negligible compared to it. A sheet resistance of 20 $\Omega/\square$ was measured for the 110 nm thick ITO layer and given the aspect ratio of the two contacts (see Fig. 4.1c)

136

an overall resistance of $\sim 100/150\Omega$ was estimated. The resulting LPF cut off frequency is given by $f_c = (2\pi R_s C)^{-1} \approx 1\ MHz$, which constitutes an intrinsic limit in the devices.

The transfer functions were measured at the different annealing temperatures as shown in Fig. 4.5. Bandwidths $(-3\ dB)$ of $\sim 116\ kHz$, $\sim 260\ kHz$, $\sim 206\ kHz$ and $\sim 232\ kHz$ were measured respectively for no annealing, 80 $^\circ C$, 100 $^\circ C$ and 150 $^\circ C$ samples. Very interestingly, the bandwidths more than double upon thermal treatment in particular for the annealing process at 80 $^\circ C$. Surprisingly, at higher temperatures, 100 $^\circ C$ and 150 $^\circ C$, the bandwidths decreases again gradually and the transfer functions become more strongly dependent on the driving current.

The measured bandwidths are all well below the given benchmark value of $\sim 1\ MHz$ estimated above based solely on the device geometry. This indicates that other effects come into play, which limit the bandwidth of the PLEDs. The data shows that the annealing treatment is effective in increasing the bandwidth of PLEDs bringing it closer to the intrinsic limit of $\sim 1\ MHz$ and hence improving the performance of the devices for VLC applications. These results suggest that some other physical processes must be involved which limit the bandwidth and that are linked to the molecular organization of the active layer.

To a first approximation, the light emission from an electroluminescent device can be considered as the result of a sequence of consecutive events including the injection of charge carriers at the electrodes, the charge transport inside the active layer, the electron hole recombination and the decay of the excited state with the emission of a photon. Each step has a characteristic
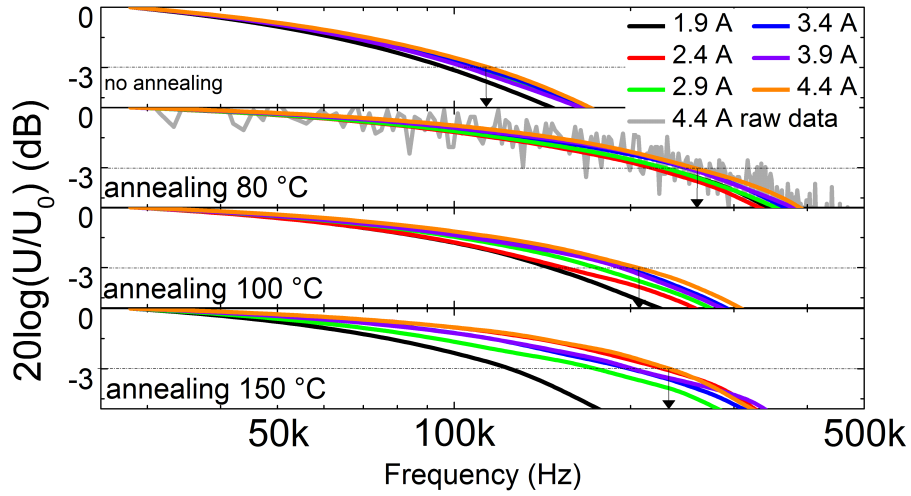
Figure 4.5: Frequency response of the PLEDs prepared with the different annealing temperatures. For each sample, the transfer function was recorded at increasing current bias as reported in the graphs modulating the light intensity with a sinusoidal AC current from 0.5 A to twice the DC bias. The low pass filter cut off frequency at $-3\ dB$ is highlighted in the diagrams. The curves reported are smoothed via a LOWESS method. An example of a row curve is reported for the sample annealed at 80 $°C$.

time constant (τ) and thus the whole system behaves as a sort of non-ideal LPF with a varying attenuation/decade. It is the step with the largest τ that determines the speed of the entire process and hence the bandwidth of a device. Actually, this is a very simplified description as a huge number of different possible paths are possible for electrons and holes. The result is that all the different steps mentioned above contribute to some extent to the overall speed of the EL emission.

One of the steps that limit the speed of the EL process the most, con-

tributing to the bandwidth of PLEDs, is the charge transport inside the polymer layer. In particular, the presence of charge carrier traps introduced at the processing time due to defects and impurities stop a significant portion of charge carriers as reported in the literature [30]. The first charges injected inside the active layer have a higher probability to fall into traps. The probability of being captured in a trap decreases drastically with the increasing of the trap occupation ratio so electrons and holes can travel across the semiconductor layer and, eventually, meet and recombine emitting a photon. For this reason, the time constant associated with the trap filling is proportional to the number of traps and inversely proportional to the injection current. This mechanism (in the reverse direction) has been described in the literature for organic photodetectors (OPDs) [134] but, to the best of the authors' collective knowledge, there are no equivalent reports for PLEDs. The dependence of the bandwidths with the current bias in the data (see Fig. 4.5) suggests the formation of an increasing number of charge carrier traps inside the polymer layer in particular upon annealing at higher temperature. In order to reduce the effect of the charge carrier trapping and increase the bandwidth of the devices, a DC bias was applied such that traps are always occupied.

4.3.3 Investigation of the molecular organization

To investigate the molecular mechanism that causes the bandwidth to increase upon thermal annealing the crystalline structure of the polymer layers was characterised. Fig. 4.6 reports the XRD spectra of thin polymer films annealed at different temperatures.
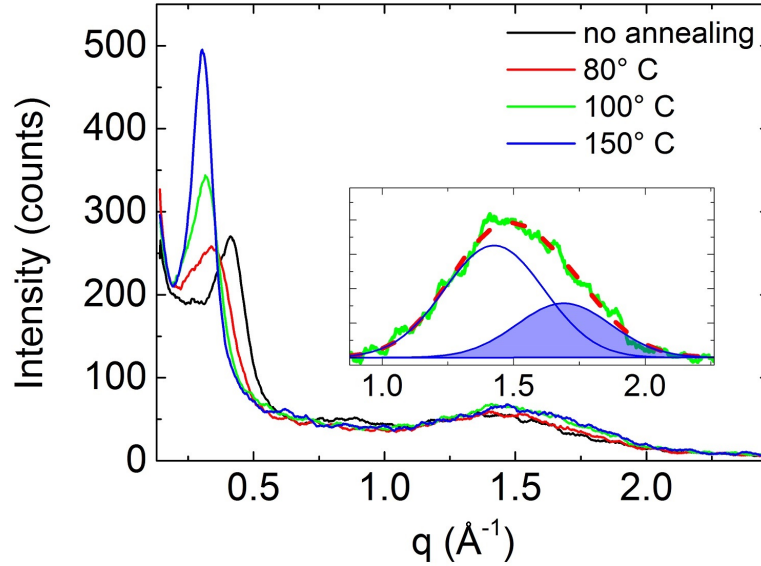
Figure 4.6: The X-ray diffraction (XRD) intensity versus the scattering vector q for the polymer films upon different annealing temperatures. The spectra were acquired at a grazing angle $\omega = 2\theta$ configuration with $\omega = 0.5°$ and $\theta = 0° \to 35°$. In the inset, the peak at large scattering vector for the sample annealed at $100°C$ is fitted qualitatively with two Gaussian curves showing that it is composed of two different contributions: the most intense peak is given by the 'amorphous halo' of the polymer while the highlighted peak represents a distance that can be assigned to the π-stacking of aromatic groups.

As reported in the literature, the main diffraction peak at low q is due to the crystal distance between different polymer backbones separated by the side chains [139, 140]. Upon annealing, this peak shifts from 0.4 Å^{-1} to 0.3 Å^{-1} corresponding to the expansion of the polymer chains from 1.5 nm

to 2.1 nm whereas the distance at full-extended side chains is 3.1 nm. Such expansion is probably driven by the increase in the lateral chain packing that causes them to elongate in a more straight conformation. The FWHM of the peaks also corresponds to an increase of the grain size of $\sim 20\%$ from 5.5 nm to 6.5 nm according to the Debye Sherrer equation.

The increase in the intensity of the peaks after annealing indicates that not only the size but also the number of crystalline grains increased upon annealing. Small peaks at ~ 0.8 Å^{-1} can be noted in the non-annealed sample and at ~ 0.6 Å^{-1} due to a second order peak of the edge-edge planes are visible in the diffractogram [141]. The broad peak at about ~ 1.5 Å^{-1} is generally referred to as the amorphous halo and it is due to characteristic distances of a disordered polymeric phase. It is very interesting to note that the tail of this peak increases slightly upon annealing revealing the presence of another small peak corresponding to a distance of about ~ 3.7 Å. This peak is assigned to the π stacking distance [141] and its increase indicates the formation of more compact crystalline structures.

4.3.4   TFT mobility and threshold voltage

An increase in the crystallinity is generally expected to result in a higher charge carrier mobility inside the polymer layer [141, 142] which would explain the higher bandwidth of the annealed samples. To verify this hypothesis, the polymer's mobility in thin film transistor (TFT) was characterised upon the different annealing treatments. Fig. 4.7 reports the transfer characteristic of the TFTs. In Tab. 4.1 the saturation mobility and threshold voltages are reported as obtained by fitting the curves in the saturation re-

Table 4.1: Mobility and threshold voltage values obtained from the thin film transistors in the saturation region at $V_{sd} = -80\ V$.

Sample	Mobility $(cm^2 s^{-1} V^{-1})$	Threshold Voltage (V)
no annealing	2.45×10^{-4}	-42.4
80 $°C$	9.22×10^{-5}	-24.0
100 $°C$	5.32×10^{-5}	-29.4
150 $°C$	1.92×10^{-5}	-28.9

gion.

Unexpectedly, the mobility is highest for the non annealed sample and decreases drastically upon thermal treatment. The annealing treatment was carried out in inert atmosphere to prevent oxidative degradation of the polymer and the absence of such degradation is confirmed by the UV-vis absorption spectra as shown later. In the XRD analysis the crystalline phase in the polymer matrix is not a continuous phase but is formed of a number of small crystal domains of $\sim 6.5\ nm$ in size embedded in an amorphous matrix. These domains are characterised by a more compact packing with a stronger π-stacking interaction between the molecules.

This change in morphology increases the size of delocalisation and consequently decreases the HOMO-LUMO energy gap of the polymer [143]. For this reason, the crystalline sites act as traps for both electrons and holes that travel in the amorphous polymer matrix. The overall effect is to decrease the mobility of the polymer layer even if the mobility inside the crystalline domains might be higher. The higher the annealing temperature the larger

the crystals and hence the deeper the trap levels causing a stronger decrease in the mobility as observed. In addition to this, the number of crystalline domains increase with annealing as shown in the XRD spectra.
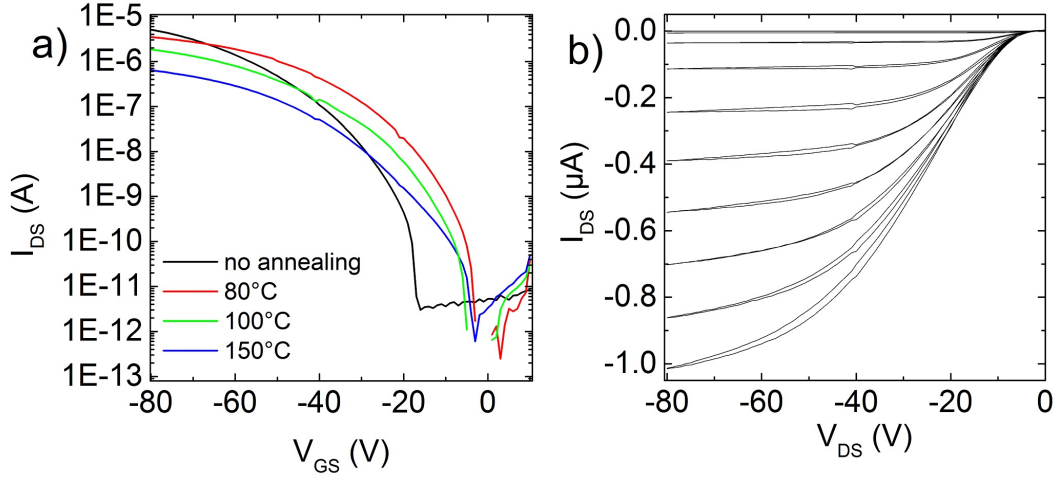
Figure 4.7: Transfer characteristics of the TFTs treated with different annealing temperatures recorded at $-80\,V - SD$ (a). Output characteristics for the sample without annealing treatment as an example (b). The curves in (b) were recorded at VGS from $-80\,V$ to $0\,V$ every $8\,V$.

It is worth noting that the hypothesis of crystal domains that act as charge carrier traps can also explain the trend in the threshold voltage (V_{th}). Surprisingly, the threshold voltage values of the TFTs show a good correlation with the bandwidth values of the PLEDs. Organic TFTs operate in accumulation regime: an electric field induces the accumulation of charge carriers in a very thin layer of the semiconductor at the insulator/semiconductor interface while the source and drain consist of simple Ohmic contacts [144]. In this type of structure, the presence of inter gap states, such as traps states

due to the crystalline domains, lowers the gate voltage needed for the formation of the conductive channel with respect to a purely amorphous phase (see Fig. 4.8). This reflects in a lower threshold voltage (absolute value) for the samples after annealing.
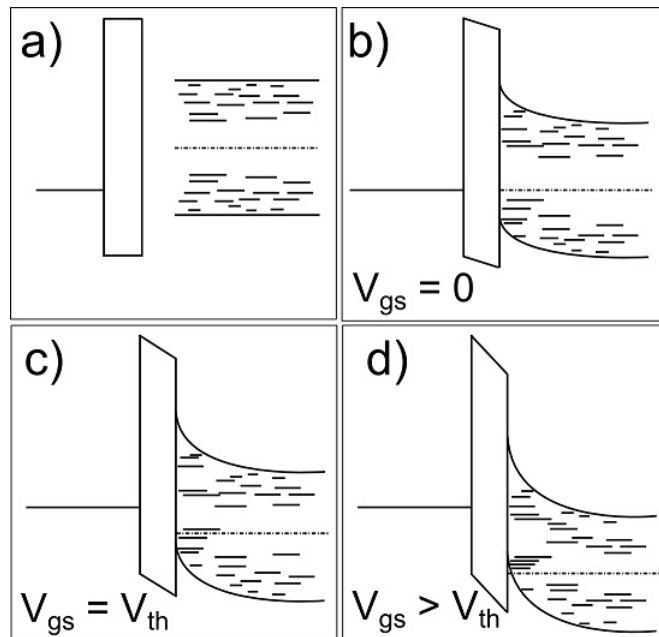
Figure 4.8: In figure (a) the energy diagram of the separated components (semiconductor and substrate) of a TFT are shown. In figures (b),(c) and (d) the energy diagram at the metal-oxide/polymer interface in an annealed TFT are reported at different values of the gate bias (V_{gs}). The figure (b) shows the band bending consequent to the equalisation of the Fermi levels. Interband localised states are due to crystalline domains embedded in an amorphous polymer matrix. According to the mechanism proposed here, the presence of such states lowers the threshold voltage of the TFT.

The mobility degradation cannot explain the devices' bandwidth increase and hence other important effects must be considered. One of the key steps in the electroluminescence process is the injection of charges from the electrodes into the active layer. In particular, the devices prepared here are characterised by a virtually zero energy barrier for the electron injection at the cathode. Instead, the injection of holes at the anode interface is limited by a larger barrier due to the energy mismatch between the HOMO of MDMO-PPV and the work function of PEDOT:PSS [36, 15].

As reported in the literature, the presence of inter band trap states is responsible for assisting and promoting the injection of charges inside the polymer across an energy barrier, when the work function of the electrode is higher (lower) than the valence (conducting) level of the semiconductor [130, 131, 145, 146, 72]. According to this mechanism, the energy distribution of the localized states in the samples after annealing creates a sort of energy ladder for the charges to reach the bulk energy level by cutting through the energy barrier. This description is in accordance with the data and it could explain the increase in the devices' bandwidth thanks to a faster injection at the electrode/polymer interface.

4.3.5 The UV-vis absorption

To confirm the presence of traps in the semiconducting layer due to crystallization the photophysics of the polymer was investigated.

The UV-vis absorption of the polymer was measured after the different annealing treatments. The spectra reported in Fig. 4.9 retain their shape even at high temperature annealing suggesting that no damage or degradation

145
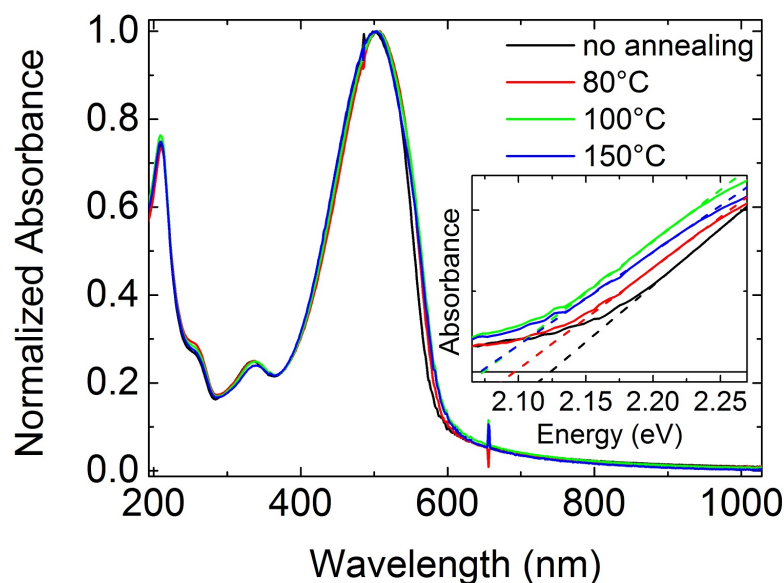
Figure 4.9: UV-vis absorption spectra (reported as -log of the transmittance) for the polymer films upon different annealing temperatures. In the inset the energy of the absorption onset via linear fitting was calculated.

is caused to the polymer. Interestingly, the onset of the main absorption peak is red shifted from 2.12 eV of the non annealed sample to 2.09 eV for annealing at 80 $°C$ and to 2.07 eV for high temperature annealing at 100 $°C$ and 150 $°C$ (see inset of Fig. 4.9). This effect indicates a decreasing of the average HOMO-LUMO gap in the polymer layer and accounts for the formation of trap states due to increased electron delocalisation via π-staking interaction. Since no peaks at higher wavelengths appear upon annealing and that no significant red-shift of the main peak is visible in the spectra with increasing annealing temperature, the possibility of the formation of ground state aggregates was discarded[147, 148, 149].

146

4.3.6 PL emission

The photoluminescence emission (PL) of the polymer films was measured using a laser excitation at 405 nm. As reported in Fig. 4.10, the annealing treatment causes a significant variation of the PL resulting in an overall redshift of the emission spectrum, a variation in the relative intensities of the vibronic spectrum components and the formation of a longer tail at higher wavelengths.
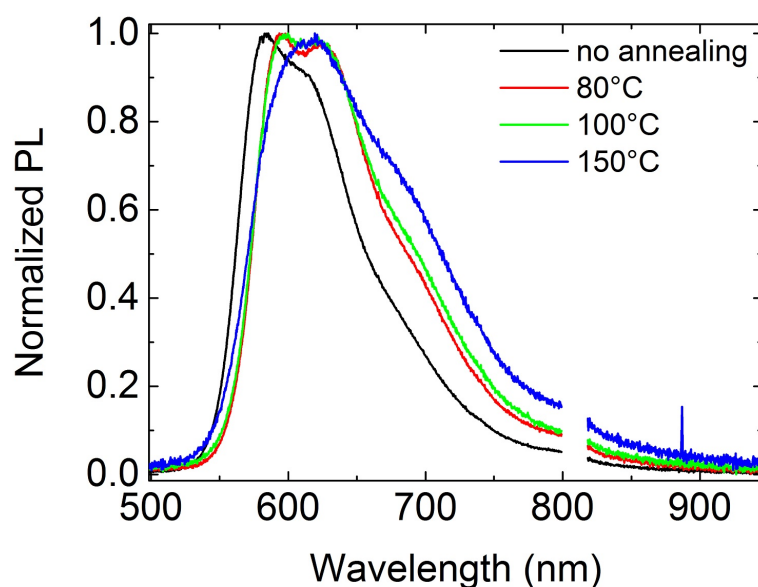
Figure 4.10: PL spectra for the polymer films upon different annealing temperatures obtained using a laser excitation source at 405 nm.

These results confirm the literature and suggest a supramolecular structural reorganization of the polymer [147, 139]. The low energy tail is generally attributed an increased molecular disorder in the literature [150]. The data shows that PL emission from excited state dimers (excimer) constitutes

an important contribution of the low energy tail in the PL. Due to the more compact packing of the polymer resulting from the increased molecular order, chromophores have a higher probability of interacting forming excimers.

4.3.7   Excited states lifetimes

To confirm the presence of excimer states the lifetimes of the excited states were determined via TCSPC spectroscopy. The lifetimes at two different wavelengths were measured: at 587 nm in correspondence of the main PL peak and at 672 nm closer to the tail emission.

In Fig. 4.11c the decay curves at the two wavelengths are reported for the samples annealed at the different temperatures. All the decays can be fitted with bi exponential curves resulting in two lifetimes $t_1 \approx 0.3$ ns and $t_2 \approx 1.0$ ns for both the wavelengths (see Fig. 4.11a).

In Fig. 4.11b it is interesting to note that, for both wavelengths, the contribution of the long lived excited state increases with the annealing temperature indicating an increase of the excimer formation upon annealing. Noteworthy, such a trend is visible also at higher energies (587 nm) suggesting a broadening of the excimer emission peak upon annealing. In other words, the thermal treatment causes the energy distribution of the trap states to spread out. It is also interesting to note that the lifetimes are slightly higher at 672 nm when compared to 587 nm. This is presumably due to the spectral diffusion effect with the migration of the excitons to longer chromophoric segments at lower energy and to a structural rearrangement of the more localized excimer states [151, 152].
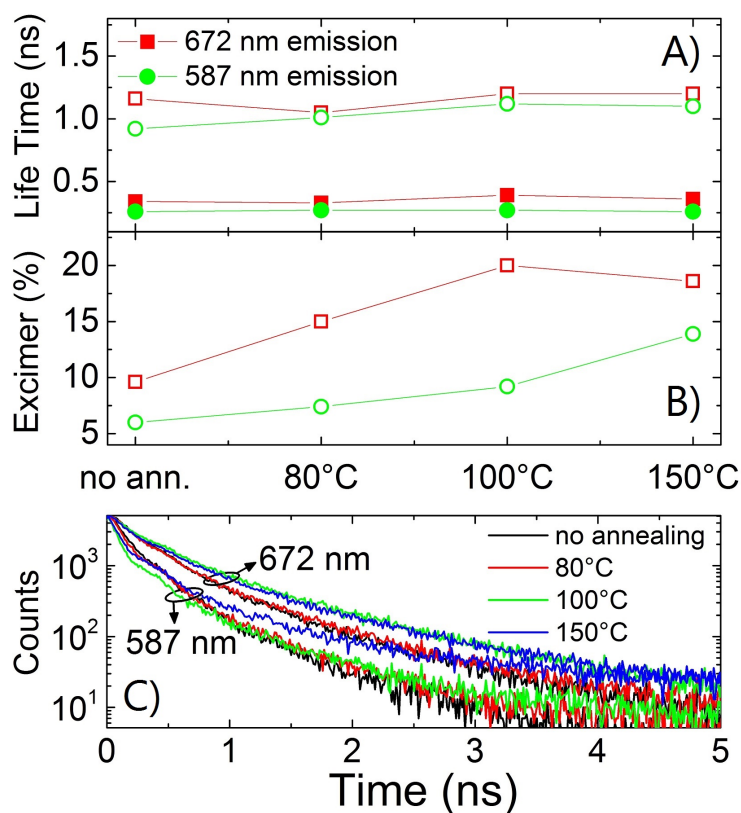
Figure 4.11: The photoluminescence decay for all samples measured at 672 *nm* and 587 *nm*. All the decays were fitted with bi-exponential curves. In A) the 2 lifetimes for each curve are shown: 2 lifetimes at 587 *nm* for the short-lived excited state (•) and for the long-lived excited state (∘) and 2 lifetimes at 672 *nm* for the short-lived excited state (■) and for the long-lived excited state (□). In B) only the percent contribution of the long-lived excited state was reported (the contributions of the short-lived excited state can be derived). In C) the two sets of experimental decay curves (at 587 *nm* and at 672 *nm*) are shown.

4.3.8 PL in solution and fitting of the spectra

To verify that the variation in the PL spectra is a consequence of molecular interaction, the PL emission of MDMO-PPV solutions was measured across a wide range of concentrations. As the number of molecules in the solution decreases, the intermolecular interaction is statistically less likely. The trend in the PL spectra with increasing concentrations is completely analogous to what happens in the case of the polymeric film with annealing at increasing temperatures.
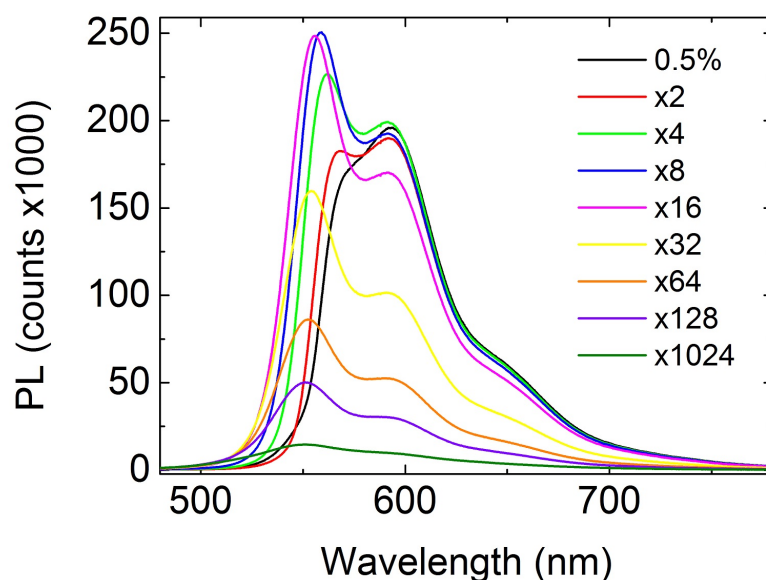
Figure 4.12: PL spectra for the polymer solution at 0.5% w/w concentrations and at the progressively more diluted concentrations. A laser excitation source at 405 nm was used.

As reported in Fig. 4.12, the spectra of polymer solutions at increasing concentrations show a red shift of the peak at the shortest wavelength, the inversion of the relative intensities of the two most intense peaks and the
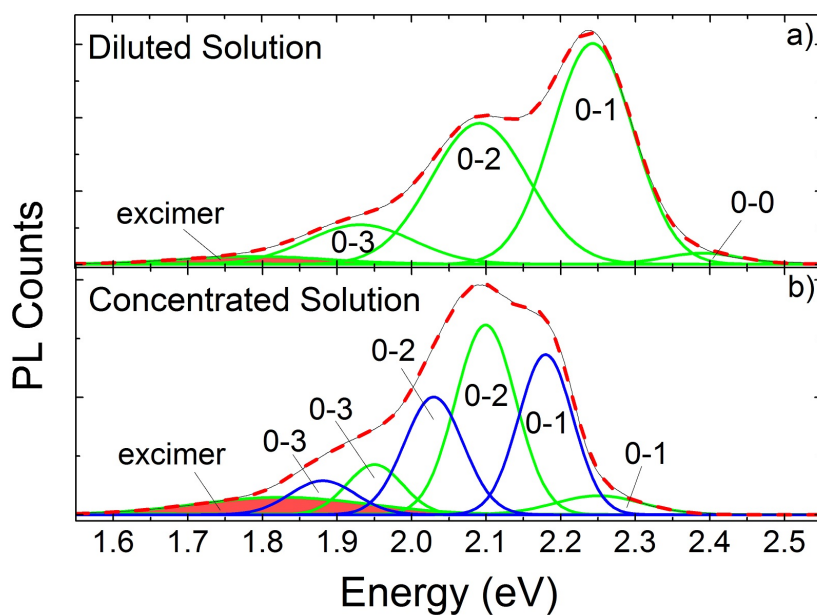
Figure 4.13: PL spectra of MDMO-PPV solutions fitted with Gaussian peaks. In a) the spectrum of the polymer solution at a concentration of 0.016% w/w is fitted with an exciton decay progression and a small contribution of excimer emission. In b) the spectrum of the polymer solution at a concentration of 0.5% w/w is fitted with 2 different exciton emission progressions due to decays from different excited states and a slightly stronger contribution of excimer emission.

progressive increase of a long and broad tail at longer wavelengths. These similarities suggest that in the film, during the spin coating deposition, the quick evaporation of the solvent 'freezes' the polymer molecules in a highly disordered morphology [141].

Surrounded by such an isotropic environment, the chromophore groups behave as if they were isolated due to no specific interaction. When the poly-

mer film is annealed, the thermal energy allows the molecules to rearrange towards lower energy conformations characterized by stronger inter and intra molecular interactions.

The PL spectra in the films are shifted at lower energy compared to the PL spectra in solution probably due to a higher conformational freedom in solution that decreases the energy of the fundamental electronic state [153]. The shape evolution of the peaks is shown very clearly in the spectra of the polymer solution.

The PL peaks of the polymer in solution were fitted using Gaussian peaks for simplicity as also reported in more detailed Frank-Condon analysis of PPV films reported in the literature [154]. The curves are shown in Fig. 4.13. At low concentrations (Fig. 4.13a) a clear progression of vibronic transitions is visible with the peaks equally spaced of about $0.15\ eV$. A small and broad peak is also present at lower energies, which was assigned to excimer emission. The vibronic structure at high concentrations is more complex. The fitting (see Fig. 4.13b) suggests the presence of a second emissive species with a distinct red shifted series of transitions, as is also reported in the literature [154].

This new series of peaks could account for the higher probability of molecules to interact specifically via π-stacking coupling between chromophoric centres. Their interaction lowers the gap between the fundamental and the excited electronic states thus lowering the energy of the PL emissions. The molecules not involved in specific interactions, instead, are only affected by the higher concentrations, whose main effect is to limit their conformational degrees of freedom. As a result, they are only subject to a variation in the
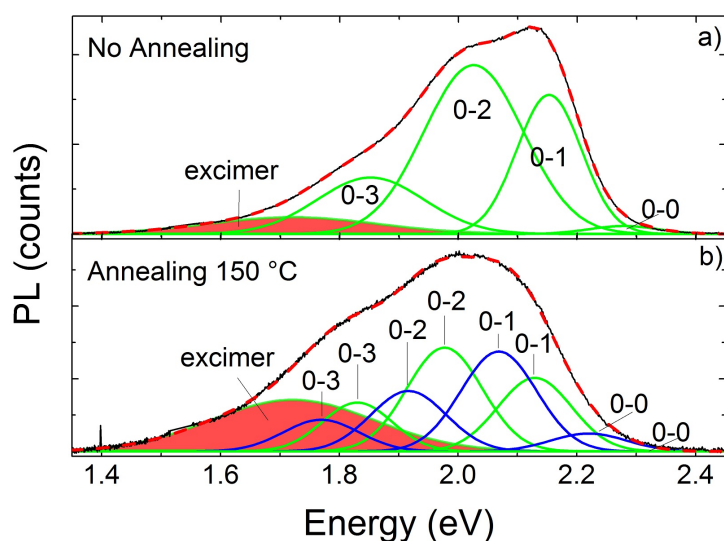
Figure 4.14: PL spectra of MDMO-PPV spin coated thin films fitted with Gaussian peaks. In a) the spectrum of the thin film as deposited is fitted using an exciton decay progression and a small contribution of excimer emission. In b) the spectrum of the thin film after thermal annealing at 150 $°C$ is fitted with 2 different exciton emission progressions due to decays from different excited states and a slightly stronger contribution of excimer emission.

relative intensities of the different vibronic peaks.

It is noteworthy that this interpretation of the PL spectra in solution can also describe perfectly the PL spectra of the films. Fig. 4.14 shows the fitting of the PL emission spectra in the film. In the solid state, the PL emission peaks are broader due to the stronger interaction between the molecules and the complexity of spectra is higher.

The spectra for the non annealed sample (see Fig. 4.14a) show only one series of vibronic peaks. The transitions $0-0$, $0-1$ and $0-2$ are spaced by $\sim$

$0.13 \, eV$. For the film annealed at $150 \, °C$ a second series of vibronic transition appears red shifted by $0.06 \, eV$ should be due to the molecules involved in the crystalline domains. This shift is in agreement with the decreasing of the average band gap that was measured with the UV-vis spectra in Fig. 4.9. This confirms the hypothesis proposed here that this new series of transitions is due exciton emission from the highly delocalised states in the crystalline domains. All the vibronic transitions in both the series are spaced by $0.15 \, eV$. The evolution of the excimer peak agrees perfectly with the evolution of the lifetimes measured with the TCSPC.

4.4 Conclusions

In this work the dynamic response of a PLED was investigated determining the main molecular mechanisms involved in the response speed. It was shown here that the molecular organization of the polymer in the active layer is a key factor that to control the dynamic characteristics of a device. The results demonstrated that a simple thermal annealing treatment during the preparation of the devices improves significantly the bandwidth of the light emitting devices. This is of fundamental importance in applications that require very fast modulation of the light output such as in communications technologies where high-speed link are necessary.

A thermal treatment was proposed here as a facile and scalable to increase the bandwidth of PLEDs by almost three times with the aim of using such devices for VLC applications. Very little is present in the literature regarding the dynamic properties of optoelectronic devices based on organic semiconductors and, in particular, polymer semiconductors, to the best of

our knowledge. Here, the morphology, the electronics properties and the photophysics of our devices were investigated upon thermal treatment to understand what processes are involved.

A significant increase in the crystallinity of the active layer was confirmed upon annealing. In particular, both the number and the size of crystal domains increases with the annealing temperature. The crystal domains are embedded in the amorphous polymer matrix. An increase of π-stacking is also evident in the polymer films after thermal annealing. The modification of the molecular organization and of the degree of aggregation is a key factor that affects the electronic properties of the devices.

Remarkably, the TFT mobility of the polymer films decreases drastically upon annealing. This can be explained considering that the formation and the growth of crystalline domain reflects in a rougher energy landscape across the polymer layer. In particular, even though larger crystalline domains are generally characterised by a higher charge mobility, nevertheless, they also have a lower band-gap and act as charge traps hampering the transport process. The larger the domains the smaller the energy gap as visible by comparing XRD and UV vis spectra for the different samples. In principle, the ideal situation would be either a large single crystal or, at the opposite, a large number of very small crystals, very close to each other inside an amorphous matrix, separated by an energy barrier smaller than the thermal energy.

However, the bandwidth of the devices increases upon thermal annealing although the mobility is drastically reduced. Unexpectedly, the mobility has such a small effect on the speed of the EL in the devices. Very interestingly,

155

the results show a good correlation between the devices' bandwidth and the threshold voltage of the TFT that suggests an important role of the energy level of aggregated states.

To identify the key factors that control the bandwidth the photophysics of the devices was investigated. The UV-vis absorption spectra showed no variation upon annealing, except for the red shift of the absorption onset that proves an average decrease of the HOMO-LUMO gap. By measuring the PL emission for the samples with the different annealing treatments and by studying the lifetimes of the excited states during the PL emission experiment the presence of polymer aggregates and the formation of localized states was confirmed with the consequent increase of emission from dimeric excited states (excimers). To explain the increased speed in the EL emission from the devices (higher bandwidth) resulting from the presence of localized trap states, a trap assisted injection mechanism was taken into account.

To confirm that the change in the PL emission upon annealing is due to molecular aggregation the PL of MDMO-PPV from a toluene solution was measured in a wide range of concentrations. The spectra show a very clear trend for the relative intensities of the peaks upon dilution. Interestingly, the trend is totally analogous to that resulting from thermal annealing treatment confirming that the molecular reorganization and aggregation is the key factor. The PL spectra in solution were fitted qualitatively using Gaussian distributions.

Very interestingly, the increase in the polymer concentration results in the comparison of a new Franck-Condon progression, shifted to lower energies. Such new progression can be explained with the presence of specific

π-stacking molecular interactions where the band gap of the chromophores is shifted to lower energies. The increase in concentration causes also a variation of the relative intensity of the peaks in the pre-existent progression probably due to a variation in the chain conformation.

Based on this interpretation also the PL spectra of the polymer films can be fitted, even if the peaks are broader and the vibronic structure is considerably less evident. It is noteworthy that the effects of thermal annealing in the solid state polymer film are analogous to the increase of concentration in a polymer solution. As deposited films are characterized by a more amorphous structure with little electronic interaction between the chromophore groups which are in a condition similar to a diluted solution. The thermal annealing causes the reorganization of the molecules towards a lower energy conformation with highly packed crystalline domains embedded in an amorphous matrix of disordered molecules. This results in a new progression of peaks in the PL spectrum as chromophores in the crystalline domains are subject to a different chemical environment.

The increased molecular packing also enhances the excimer emission in the tail at lower wavelengths. This effect is particularly visible in the EL spectra as the charges travel across the active layer before recombining and hence have a higher probability to fall into crystalline traps and form dimeric excites state (excimer).

In this work, a processing method was proposed to increase the response speed of PLEDs based on the thermal annealing of the devices during the preparation. This has important repercussions in the application of such devices as transmitter for wireless communication technologies. In this regard,

the results show that the capacitive effect is not always the main limit to the speed of thin film devices.

The effects of the thermal annealing of MDMO-PPV films were investigated for what concern the molecular organization of the polymer and the electronic and photophysical properties. In particular, the data suggests that the charge injection is the rate-limiting step in the EL process and that the thermal treatment enables a trap-assisted injection mechanism that has a fundamental impact on the dynamics of the PLEDs. A new interpretation on the variation of MDMO PPV photoluminescence upon thermal annealing based on the formation of crystalline domains was also proposed in this work. These results can be of critical importance for the designing of PLED devices for innovative applications such as VLC where the response speed is a stringent requirement.

Conclusions and outlook

The experiments described in this work aim to the optimisation of polymer light-emitting diodes by the use of innovative materials such as graphene-based layers or the development of processing methods for the preparation of devices with increased on/off speed for innovative applications.

In chapter 2 thin films were prepared on transparent substrates starting from graphene and graphene oxide liquid dispersions using different deposition methods. The films after the deposited were characterised studying the effects of a thermal treatment and of chemical doping in terms of morphology, electrical conductivity, work function and UV-visible light transmission.

The thermal treatment improved drastically the electrical conduction properties of both graphene oxide and LPE graphene films. The conductivity of such films was still not comparable with the standard reference of ITO for a same level of transparency mainly due to the fact that the preparation of the dispersions, the deposition of the films and the annealing treatment could be optimised even further.

In particular, for what concerns liquid-phase exfoliated graphene, more prolonged sonications for the exfoliation of graphite followed by a systematic centrifugation and filtration for the separation of highly monodisperse few-layer graphene can be explored. This approach could lead to a films with

lower surface roughness. An XRD analysis would be useful to determine the concentration of unexfoliated graphite crystals. A change in morphology after a thermal annealing process could be also analysed using XRD measurements. A Raman spectrum could confirm the presence of graphite from the shape of the 2D peak.

Chemical p-type doping has proven to raise the work function of the films by some electron volts units resulting in an appealing treatment of graphene surfaces. It would be interesting to explore further the hypothesis presented here regarding the interaction of TFSA with the C=O and C-OH groups on rGO. In particular, a systematic investigation using ATR-FTIR could reveal a shift to lower frequencies of the C=O peak upon interaction with TFSA. The intensity of TFSA S=O and C-F bands on annealed and not annealed graphene samples could suggest if oxidation increases the adsorption of TFSA via specific interactions. Graphene powder instead of a thin film could be used in order to increase the signal.

Next possible experiments involve the application of reduced GO and LPE graphene modified with TFSA as ITO surface modifier and hole-injection layers in polymer light-emitting diodes (PLEDs). Conductive AFM could be used to determine the deposition of a homogeneous film on top of ITO. Due to the roughness of ITO ($rms \sim 3\ nm$) the AFM morphology is not enough to determine the presence of a film only a few nanometres thick.

Chapter 3 focussed on the characterisation of the work function of LPE graphene and SWCNTs thin films deposited on ITO. The work function measured in air was compared with that measured inside a polymer light-emitting device (PLED) using two different measurement techniques. The

162

work function of graphene and CNTs appears to be very similar and this is in accordance with the values reported in the literature. The data showed that there is a shift between the mean values of work function of the films inside the device and the work function in air. Further investigations are needed to asses the nature of this difference.

A more extended characterisation of the film could also be beneficial to the analysis of the work function shift. In particular the films could be characterised in terms of sheet resistance, UV-vis light absorption, morphology (AFM), Raman and crystallinity (XRD). A thermal annealing process can improve the conductivity of the films for their application in PLEDs.

In chapter 4 a processing method for the emissive layer of PLEDs was proposed in order to increase the on/off switch speed of the devices. This is particularly interesting for the application of PLEDs as transmitter devices in VLC technology. The main speed limiting factors for PLEDs have been analysed. An emissive layer of poly[2-methoxy-5(3',7'-dimethyloctylocy)-1,4-phenilenevinylene] (MDMO-PPV) was used. The response speed of the PLEDs was increased by more than two times, from $\sim 116\ kHz$ up to $\sim 260 kHz$ with thermal annealing. The process was investigated via a structural, electrical and photophysical characterisation of the polymer layer.

As a further experiment the PL efficiency of the polymer can be measured upon thermal annealing to complete the characterisation of the emissive layer. Another experiment is to design a geometry for devices with a smaller area to confirm that the speed of the device cannot be increased any further. A faster heat dissipation of smaller area devices allows the use of pulsed higher currents to increase the light intensity.

Bibliography

[1] P. Haigh, F. Bausi, H. Minh, I. Papakonstantinou, W. Popoola, A. Burton, and F. Cacialli. Wavelength-Multiplexed Polymer LEDs: Towards 55 Mb/s Organic Visible Light Communications. *IEEE Journal on Selected Areas in Communications*, PP(99):1–1, 2015.

[2] W.R. Salaneck, R.H. Friend, and J.L. Brédas. Electronic structure of conjugated polymers: consequences of electron–lattice coupling. *Physics Reports*, 319(6):231–251, October 1999.

[3] Mikito Koshino. Stacking-dependent optical absorption in multilayer graphene. *New Journal of Physics*, 15(1):015010, January 2013.

[4] A. H. Castro Neto, F. Guinea, N. M. R. Peres, K. S. Novoselov, and A. K. Geim. The electronic properties of graphene. *Reviews of Modern Physics*, 81:109–162, January 2009.

[5] A. K. Geim and K. S. Novoselov. The rise of graphene. *Nat. Mat.*, 6(3):183–191, 2007.

[6] Masato Aoki and Hiroshi Amawashi. Dependence of band structures on stacking and field in layered graphene. *Solid State Communications*, 142(3):123–127, April 2007.

[7] Alexander J. Pearce, Fabio Cavaliere, and Eros Mariani. Conductance and shot noise in strained bilayer graphene. *J. Phys.: Condens. Matter*, 25(37):375301, September 2013.

[8] J.H. Burroughes, D.D.C. Bradley, A.R. Brown, R.N. Marks, K. Mackay, R.H. Friend, P.L. Burns, and A.B. Holmes. Light-emitting diodes based on conjugated polymers. *Nature*, 347:539–541, 1990.

[9] Paul Anthony Haigh, Zabih Ghassemlooy, Hoa Le Minh, Sujan Rajbhandari, Francesco Arca, Sandro Francesco Tedde, Oliver Hayden, and Ioannis Papakonstantinou. Exploiting Equalization Techniques for Improving Data Rates in Organic Optoelectronic Devices for Visible Light Communications. *Journal of Lightwave Technology*, 30(19):3081–3088, October 2012.

[10] P.A. Haigh, Z. Ghassemlooy, I. Papakonstantinou, and Hoa Le Minh. 2.7 Mb/s With a 93-kHz White Organic Light Emitting Diode and Real Time ANN Equalizer. *IEEE Photonics Technology Letters*, 25(17):1687–1690, September 2013.

[11] P.A. Haigh, Z. Ghassemlooy, S. Rajbhandari, and I. Papakonstantinou. Visible light communications using organic light emitting diodes. *IEEE Communications Magazine*, 51(8):148–154, August 2013.

[12] P.A. Haigh, F. Bausi, T. Kanesan, Son Thai Le, S. Rajbhandari, Z. Ghassemlooy, I. Papakonstantinou, W. Popoola, A. Burton, Hoa Le Minh, A.D. Ellis, and F. Cacialli. A 20-Mb/s VLC Link With a Polymer LED and a Multilayer Perceptron Equalizer. *IEEE Photonics Technology Letters*, 26(19):1975–1978, October 2014.

[13] P.A. Haigh, Z. Ghassemlooy, F. Bausi, I. Papakonstantinou, H. Le Minh, S.F. Tedde, O. Hayden, and F. Cacialli. Organic visible light communications: Recent progress. In *2014 16th International Conference on Transparent Optical Networks (ICTON)*, pages 1–5, July 2014.

[14] Paul A. Haigh, Francesco Bausi, Zabih Ghassemlooy, Ioannis Papakonstantinou, Hoa Le Minh, Charlotte Flechon, and Franco Cacialli. Next Generation Visible Light Communications: 10 Mb/s with Polymer Light-Emitting Diodes. In *Optical Fiber Communication Conference*, OSA Technical Digest (online), page Th1F.4. Optical Society of America, March 2014.

[15] Paul Anthony Haigh, Francesco Bausi, Zabih Ghassemlooy, Ioannis Papakonstantinou, Hoa Le Minh, Charlotte Flèchon, and Franco Cacialli. Visible light communications: real time 10 Mb/s link with a low bandwidth polymer light-emitting diode. *Optics Express*, 22(3):2830–2838, February 2014.

[16] Son T. Le, T. Kanesan, F. Bausi, P. A. Haigh, S. Rajbhandari, Z. Ghassemlooy, I. Papakonstantinou, W. O. Popoola, A. Burton, H. Le Minh, F. Cacialli, and A. D. Ellis. 10mb/s visible light transmission system using a polymer light-emitting diode with orthogonal frequency division multiplexing. *Optics Letters*, 39(13):3876–3879, July 2014.

[17] A. Bernanose. Electroluminescence of organic compounds. *British Journal of Applied Physics*, 6(S4):S54, January 1955.

[18] H. Kallmann and M. Pope. Positive Hole Injection into Organic Crystals. *The Journal of Chemical Physics*, 32(1):300–301, January 1960.

[19] H. Kallmann and M. Pope. Bulk Conductivity in Organic Crystals. *Nature*, 186(4718):31–33, April 1960.

[20] M. Pope, H. P. Kallmann, and P. Magnante. Electroluminescence in Organic Crystals. *The Journal of Chemical Physics*, 38(8):2042–2043, April 1963.

[21] R McNeill, R Siudak, JH Wardlaw, and DE Weiss. Electronic Conduction in Polymers. I. The Chemical Structure of Polypyrrole. *Australian Journal of Chemistry*, 16(6):1056–1075, January 1963.

[22] Mizuka Sano, Martin Pope, and Hartmut Kallmann. Electroluminescence and Band Gap in Anthracene. *The Journal of Chemical Physics*, 43(8):2920–2921, October 1965.

[23] W. Helfrich and W. G. Schneider. Recombination Radiation in Anthracene Crystals. *Physical Review Letters*, 14(7):229–231, February 1965. 232.

[24] Roger Hugh Partridge. Radiation sources, November 1976.

[25] Hideki Shirakawa, Edwin J. Louis, Alan G. MacDiarmid, Chwan K. Chiang, and Alan J. Heeger. Synthesis of electrically conducting organic polymers: halogen derivatives of polyacetylene, (CH)x. *Journal of the Chemical Society, Chemical Communications*, (16):578–580, January 1977.

[26] C. W. Tang and S. A. VanSlyke. Organic electroluminescent diodes. *Applied Physics Letters*, 51(12):913–915, September 1987. 6675.

[27] H. Koezuka, A. Tsumura, and T. Ando. Field-effect transistor with polythiophene thin film. *Synthetic Metals*, 18(1-3):699–704, February 1987. 202.

[28] Bengt Nordén and E. Krutmeijer. Conductive polymers. *The Royal Swedish Academy of Sciences, The Nobel Prize in Chemistry*, 2000.

[29] Sarah Schols. *Device Architecture and Materials for Organic Light-Emitting Devices: Targeting High Current Densities and Control of the Triplet Concentration.* Springer, May 2011.

[30] H. T. Nicolai, M. Kuik, G. a. H. Wetzelaer, B. de Boer, C. Campbell, C. Risko, J. L. Brédas, and P. W. M. Blom. Unification of trap-limited electron transport in semiconducting polymers. *Nature Materials*, 11(10):882–887, October 2012.

[31] P. W. M. Blom and M. C. J. M. Vissenberg. Charge transport in poly(p-phenylene vinylene) light-emitting diodes. *Materials Science and Engineering: R: Reports*, 27(3-4):53–94, May 2000.

[32] H. Kim, C. M. Gilmore, A. Piquè, J. S. Horwitz, H. Mattoussi, H. Murata, Z. H. Kafafi, and D. B. Chrisey. Electrical, optical, and structural properties of indium-tin-oxide thin films for organic light-emitting devices. *Journal of Applied Physics*, 86(11):6451–6461, December 1999.

[33] I. Hamberg and C. G. Granqvist. Evaporated sn-doped In_2O_3 films: Basic optical properties and applications to energyefficient windows. *Journal of Applied Physics*, 60(11):R123–R160, December 1986.

[34] T.M. Brown, G.M. Lazzerini, L.J. Parrott, V. Bodrozic, L. Burgi, and F. Cacialli. Time dependence and freezing-in of the electrode oxygen plasma-induced work function enhancement in polymer semiconductor heterostructures. *Organic Electronics*, 2011.

[35] JS Kim, M. Granström, RH Friend, N. Johansson, WR Salaneck, R. Daik, WJ Feast, and F. Cacialli. Indium-tin oxide treatments for single-and double-layer polymeric light-emitting diodes: The relation between the anode physical, chemical, and morphological properties and the device performance. *Journal of applied physics*, 84:6859, 1998.

[36] TM Brown, JS Kim, RH Friend, F. Cacialli, R. Daik, and WJ Feast. Built-in field electroabsorption spectroscopy of polymer light-emitting diodes incorporating a doped poly (3,4-ethylene dioxythiophene) hole injection layer. *Applied Physics Letters*, 75:1679, 1999.

[37] Y. Park, V. Choong, E. Ettedgui, Y. Gao, B. R. Hsieh, T. Wehrmeister, and K. Mullen. Energy level bending and alignment at the interface between Ca and a phenylene vinylene oligomer. *Applied Physics Letters*, 69(8):1080, 1996.

[38] I. H. Campbell, T. W. Hagler, D. L. Smith, and J. P. Ferraris. Direct measurement of conjugated polymer electronic excitation energies using metal/polymer/metal structures. *Physical review letters*, 76(11):1900–1903, 1996.

[39] D. Braun and A. J. Heeger. Visible light emission from semiconducting polymer diodes. *Applied Physics Letters*, 58(18):1982–1984, May 1991.

[40] Nurlan Tokmoldin, Nicholas Griffiths, Donal D. C. Bradley, and Saif A. Haque. A Hybrid Inorganic–Organic Semiconductor Light-Emitting Diode Using ZrO2 as an Electron-Injection Layer. *Advanced Materials*, 21(34):3475–3478, 2009.

[41] T. van Woudenbergh, P. W. M. Blom, M. C. J. M. Vissenberg, and J. N. Huiberts. Temperature dependence of the charge injection in poly-dialkoxy-p-phenylene vinylene. *Applied Physics Letters*, 79(11):1697, 2001.

[42] David Cohen. Earth audit. *New Scientist*, 194(2605):34–41, May 2007.

[43] Zhong Chen, Brian Cotterell, and Wei Wang. The fracture of brittle thin films on compliant substrates in flexible displays. *Engineering Fracture Mechanics*, 69(5):597–603, March 2002.

[44] Lewis Gomez De Arco, Yi Zhang, Cody W. Schlenker, Koungmin Ryu, Mark E. Thompson, and Chongwu Zhou. Continuous, highly flexible, and transparent graphene films by chemical vapor deposition for organic photovoltaics. *ACS Nano*, 4(5):2865–2873, May 2010.

[45] P. R. Wallace. The band theory of graphite. *Phys. Rev.*, 71(9):622–634, May 1947.

[46] R. Saito, Gene Dresselhaus, and Mildred S. Dresselhaus. *Physical Properties of Carbon Nanotube*. Imperial College Press, 1998.

[47] Phaedon Avouris. Graphene: Electronic and photonic properties and devices. *Nano Let.*, 10:4285–4294, November 2010.

[48] K. S. Novoselov. Electric field effect in atomically thin carbon films. *Science*, 306:666–669, October 2004.

[49] P. Blake, E. W. Hill, A. H. Castro Neto, K. S. Novoselov, D. Jiang, R. Yang, T. J. Booth, and A. K. Geim. Making graphene visible. *Applied Physics Letters*, 91(6):063124, 2007.

[50] Denis L. Nika and Alexander A. Balandin. Two-dimensional phonon transport in graphene. *J. Phys.: Condens. Matter*, 24(23):233203, June 2012.

[51] A. B. Kuzmenko, E. van Heumen, F. Carbone, and D. van der Marel. Universal optical conductance of graphite. *Phys. Rev. Lett.*, 100(11):117401, March 2008.

[52] R. R. Nair, P. Blake, A. N. Grigorenko, K. S. Novoselov, T. J. Booth, T. Stauber, N. M. R. Peres, and A. K. Geim. Fine structure constant defines visual transparency of graphene. *Science*, 320:1308–1308, June 2008.

[53] Li Yang, Jack Deslippe, Cheol-Hwan Park, Marvin L. Cohen, and Steven G. Louie. Excitonic effects on the optical response of graphene and bilayer graphene. *Phys. Rev. Lett.*, 103(18):186802, October 2009.

[54] Kin Fai Mak, Jie Shan, and Tony F. Heinz. Seeing many-body effects in single- and few-layer graphene: Observation of two-dimensional saddle-point excitons. *Phys. Rev. Lett.*, 106(4):046401, January 2011.

[55] V. G. Kravets, A. N. Grigorenko, R. R. Nair, P. Blake, S. Anissimova, K. S. Novoselov, and A. K. Geim. Spectroscopic ellipsometry of graphene and an exciton-shifted van Hove peak in absorption. *Physical Review B*, 81(15):155413, April 2010.

[56] Peter Blake, Paul D. Brimicombe, Rahul R. Nair, Tim J. Booth, Da Jiang, Fred Schedin, Leonid A. Ponomarenko, Sergey V. Morozov, Helen F. Gleeson, Ernie W. Hill, Andre K. Geim, and Kostya S. Novoselov. Graphene-based liquid crystal device. *Nano Lett.*, 8(6):1704–1708, June 2008.

[57] Junbo Wu, Mukul Agrawal, Héctor A. Becerril, Zhenan Bao, Zunfeng Liu, Yongsheng Chen, and Peter Peumans. Organic light-emitting diodes on solution-processed graphene transparent electrodes. *ACS Nano*, 4(1):43–48, January 2010.

[58] Jian-Hao Chen, W. Cullen, C. Jang, M. Fuhrer, and E. Williams. Defect scattering in graphene. *Physical Review Letters*, 102(23), June 2009.

[59] J. Hicks, M. Sprinkle, K. Shepperd, F. Wang, A. Tejeda, A. Taleb-Ibrahimi, F. Bertran, P. Le Fèvre, W. A. de Heer, C. Berger, and E. H. Conrad. Symmetry breaking in commensurate graphene rotational stacking: Comparison of theory and experiment. *Phys. Rev. B*, 83(20):205403, May 2011.

[60] Hongtao Liu, Yunqi Liu, and Daoben Zhu. Chemical doping of graphene. *Journal of Materials Chemistry*, 21(10):3335, 2011.

[61] K. S. Novoselov, V. I. Fal'ko, L. Colombo, P. R. Gellert, M. G. Schwab, and K. Kim. A roadmap for graphene. *Nature*, 490(7419):192–200, October 2012.

[62] Francesco Bonaccorso, Antonio Lombardo, Tawfique Hasan, Zhipei Sun, Luigi Colombo, and Andrea C. Ferrari. Production and processing of graphene and 2d crystals. *Materials Today*, 15(12):564–589, December 2012.

[63] Yenny Hernandez, Valeria Nicolosi, Mustafa Lotya, Fiona M. Blighe, Zhenyu Sun, Sukanta De, I. T. McGovern, Brendan Holland, Michele Byrne, Yurii K. Gun'Ko, John J. Boland, Peter Niraj, Georg Duesberg, Satheesh Krishnamurthy, Robbie Goodhue, John Hutchison, Vittorio Scardaci, Andrea C. Ferrari, and Jonathan N. Coleman. High-yield production of graphene by liquid-phase exfoliation of graphite. *Nature Nanotechnology*, 3:563–568, August 2008.

[64] Jonathan N. Coleman. Liquid-phase exfoliation of nanotubes and graphene. *Advanced Functional Materials*, 19(23):3680–3695, 2009.

[65] Mustafa Lotya, Yenny Hernandez, Paul J. King, Ronan J. Smith, Valeria Nicolosi, Lisa S. Karlsson, Fiona M. Blighe, Sukanta De, Zhiming Wang, I. T. McGovern, Georg S. Duesberg, and Jonathan N. Coleman. Liquid phase production of graphene by exfoliation of graphite in Surfactant/Water solutions. *Journal of the American Chemical Society*, 131(10):3611–3620, March 2009.

[66] T. Hasan, F. Torrisi, Z. Sun, D. Popa, V. Nicolosi, G. Privitera, F. Bonaccorso, and A. C. Ferrari. Solution-phase exfoliation of graphite

for ultrafast photonics. *physica status solidi (b)*, 247(11-12):2953–2957, December 2010.

[67] Zhong-Shuai Wu, Wencai Ren, Libo Gao, Bilu Liu, Chuanbin Jiang, and Hui-Ming Cheng. Synthesis of high-quality graphene with a predetermined number of layers. *Carbon*, 47(2):493–499, February 2009.

[68] H. A. Becerril, J. Mao, Z. Liu, R. M. Stoltenberg, Z. Bao, and Y. Chen. Evaluation of solution-processed reduced graphene oxide films as transparent conductors. *Acs Nano*, 2(3):463–470, 2008.

[69] Cristina Gomez-Navarro, Jannik C. Meyer, Ravi S. Sundaram, Andrey Chuvilin, Simon Kurasch, Marko Burghard, Klaus Kern, and Ute Kaiser. Atomic structure of reduced graphene oxide. *Nano Lett.*, 10(4):1144–1148, April 2010. WOS:000276557100008.

[70] Goki Eda, Giovanni Fanchini, and Manish Chhowalla. Large-area ultrathin films of reduced graphene oxide as a transparent and flexible electronic material. *Nature Nanotechnology*, 3:270–274, April 2008.

[71] Dan Li, Marc B. Müller, Scott Gilje, Richard B. Kaner, and Gordon G. Wallace. Processable aqueous dispersions of graphene nanosheets. *Nature Nanotechnology*, 3:101–105, January 2008.

[72] Z. B. Wang, M. G. Helander, S. W. Tsang, and Z. H. Lu. Abnormal charge injection behavior at metal-organic interfaces. *Physical Review B*, 78(19), November 2008.

[73] Toshiyuki Kobayashi, Masashi Bando, Nozomi Kimura, Keisuke Shimizu, Koji Kadono, Nobuhiko Umezu, Kazuhiko Miyahara, Shinji

Hayazaki, Sae Nagai, Yukiko Mizuguchi, Yosuke Murakami, and Daisuke Hobara. Production of a 100-m-long high-quality graphene transparent conductive film by roll-to-roll chemical vapor deposition and transfer process. *Applied Physics Letters*, 102(2):023112–023112–4, January 2013.

[74] Justin C. Koepke, Joshua D. Wood, David Estrada, Zhun-Yong Ong, Kevin T. He, Eric Pop, and Joseph W. Lyding. Atomic-scale evidence for potential barriers and strong carrier scattering at graphene grain boundaries: A scanning tunneling microscopy study. *ACS Nano*, December 2012.

[75] Sukang Bae, Hyeongkeun Kim, Youngbin Lee, Xiangfan Xu, Jae-Sung Park, Yi Zheng, Jayakumar Balakrishnan, Tian Lei, Hye Ri Kim, Young Il Song, Young-Jin Kim, Kwang S. Kim, Barbaros Özyilmaz, Jong-Hyun Ahn, Byung Hee Hong, and Sumio Iijima. Roll-to-roll production of 30-inch graphene films for transparent electrodes. *Nat Nano*, 5(8):574–578, August 2010.

[76] Claire Berger, Zhimin Song, Tianbo Li, Xuebin Li, Asmerom Y. Ogbazghi, Rui Feng, Zhenting Dai, Alexei N. Marchenkov, Edward H. Conrad, Phillip N. First, and Walt A. de Heer. Ultrathin epitaxial graphite: 2D electron gas properties and a route toward graphene-based nanoelectronics. *J. Phys. Chem. B*, 108(52):19912–19916, December 2004.

[77] C. Riedl, C. Coletti, T. Iwasaki, A. A. Zakharov, and U. Starke. Quasi-free-standing epitaxial graphene on SiC obtained by hydrogen interca-

lation. *Phys. Rev. Lett.*, 103(24):246804, December 2009.

[78] Xu Du, Ivan Skachko, Fabian Duerr, Adina Luican, and Eva Y. Andrei. Fractional quantum Hall effect and insulating phase of Dirac electrons in graphene. *Nature*, 462:192–195, October 2009.

[79] C. Lee, X. Wei, J. W. Kysar, and J. Hone. Measurement of the Elastic Properties and Intrinsic Strength of Monolayer Graphene. *Science*, 321:385–388, July 2008.

[80] F. Bonaccorso, Z. Sun, T. Hasan, and A. C. Ferrari. Graphene photonics and optoelectronics. *Nature Photonics*, 4(9):611–622, August 2010.

[81] A. W. Tsen, L. Brown, M. P. Levendorf, F. Ghahari, P. Y. Huang, R. W. Havener, C. S. Ruiz-Vargas, D. A. Muller, P. Kim, and J. Park. Tailoring Electrical Transport Across Grain Boundaries in Polycrystalline Graphene. *Science*, 336(6085):1143–1146, May 2012.

[82] Xuesong Li, Weiwei Cai, Jinho An, Seyoung Kim, Junghyo Nah, Dongxing Yang, Richard Piner, Aruna Velamakanni, Inhwa Jung, Emanuel Tutuc, Sanjay K. Banerjee, Luigi Colombo, and Rodney S. Ruoff. Large-Area Synthesis of High-Quality and Uniform Graphene Films on Copper Foils. *Science*, 324(5932):1312–1314, June 2009.

[83] Arlene O'Neill, Umar Khan, Peter N. Nirmalraj, John Boland, and Jonathan N Coleman. Graphene Dispersion and Exfoliation in Low Boiling Point Solvents. *The Journal of Physical Chemistry C*, 115(13):5422–5428, April 2011.

[84] Keith R. Paton, Eswaraiah Varrla, Claudia Backes, Ronan J. Smith, Umar Khan, Arlene O'Neill, Conor Boland, Mustafa Lotya, Oana M. Istrate, Paul King, Tom Higgins, Sebastian Barwich, Peter May, Pawel Puczkarski, Iftikhar Ahmed, Matthias Moebius, Henrik Pettersson, Edmund Long, João Coelho, Sean E. O'Brien, Eva K. McGuire, Beatriz Mendoza Sanchez, Georg S. Duesberg, Niall McEvoy, Timothy J. Pennycook, Clive Downing, Alison Crossley, Valeria Nicolosi, and Jonathan N. Coleman. Scalable production of large quantities of defect-free few-layer graphene by shear exfoliation in liquids. *Nature Materials*, 13(6):624–630, June 2014.

[85] Andrea Schlierf, Huafeng Yang, Elias Gebremedhn, Emanuele Treossi, Luca Ortolani, Liping Chen, Andrea Minoia, Vittorio Morandi, Paolo Samorì, Cinzia Casiraghi, David Beljonne, and Vincenzo Palermo. Nanoscale insight into the exfoliation mechanism of graphene with organic dyes: effect of charge, dipole and molecular structure. *Nanoscale*, 5(10):4205–4216, May 2013.

[86] Emanuele Treossi, Manuela Melucci, Andrea Liscio, Massimo Gazzano, Paolo Samorì, and Vincenzo Palermo. High-contrast visualization of graphene oxide on dye-sensitized glass, quartz, and silicon by fluorescence quenching. *J. Am. Chem. Soc.*, 131(43):15576–15577, November 2009.

[87] Lei Zhang, Hongtao Liu, Yan Zhao, Xiangnan Sun, Yugeng Wen, Yunlong Guo, Xike Gao, Chong-an Di, Gui Yu, and Yunqi Liu. Inkjet

Printing High-Resolution, Large-Area Graphene Patterns by Coffee-Ring Lithography. *Advanced Materials*, 24(3):436–440, January 2012.

[88] Felice Torrisi, Tawfique Hasan, Weiping Wu, Zhipei Sun, Antonio Lombardo, Tero S. Kulmala, Gen-Wen Hsieh, Sungjune Jung, Francesco Bonaccorso, Philip J. Paul, Daping Chu, and Andrea C. Ferrari. Inkjet-Printed Graphene Electronics. *ACS Nano*, 6(4):2992–3006, April 2012.

[89] Priyank V. Kumar, Neelkanth M. Bardhan, Sefaattin Tongay, Junqiao Wu, Angela M. Belcher, and Jeffrey C. Grossman. Scalable enhancement of graphene oxide properties by thermally driven phase transformation. *Nature Chemistry*, advance online publication, December 2013.

[90] Hannes C. Schniepp, Je-Luen Li, Michael J. McAllister, Hiroaki Sai, Margarita Herrera-Alonso, Douglas H. Adamson, Robert K. Prud'homme, Roberto Car, Dudley A. Saville, and Ilhan A. Aksay. Functionalized Single Graphene Sheets Derived from Splitting Graphite Oxide. *The Journal of Physical Chemistry B*, 110(17):8535–8539, May 2006.

[91] Jeffrey M. Mativetsky, Emanuele Treossi, Emanuele Orgiu, Manuela Melucci, Giulio Paolo Veronese, Paolo Samorí, and Vincenzo Palermo. Local Current Mapping and Patterning of Reduced Graphene Oxide. *Journal of the American Chemical Society*, 132(40):14130–14136, October 2010.

[92] Jeffrey M. Mativetsky, Andrea Liscio, Emanuele Treossi, Emanuele Orgiu, Alberto Zanelli, Paolo Samorì, and Vincenzo Palermo. Gra-

phene Transistors via in Situ Voltage-Induced Reduction of Graphene-Oxide under Ambient Conditions. *Journal of the American Chemical Society*, 133(36):14320–14326, September 2011.

[93] TM Brown and F. Cacialli. Contact optimization in polymer light-emitting diodes. *Journal of Polymer Science Part B: Polymer Physics*, 41(21):2649–2664, 2003.

[94] S Tongay, K Berke, M Lemaitre, Z Nasrollahi, D B Tanner, A F Hebard, and B R Appleton. Stable hole doping of graphene for low electrical resistance and high optical transparency. *Nanotechnology*, 22(42):425701, October 2011.

[95] Xiaochang Miao, Sefaattin Tongay, Maureen K. Petterson, Kara Berke, Andrew G. Rinzler, Bill R. Appleton, and Arthur F. Hebard. High Efficiency Graphene Solar Cells by Chemical Doping. *Nano Letters*, 12(6):2745–2750, June 2012.

[96] Youngsoo Kim, Jaechul Ryu, Myungjin Park, Eun Sun Kim, Je Min Yoo, Jaesung Park, Jin Hyoun Kang, and Byung Hee Hong. Vapor-Phase Molecular Doping of Graphene for High-Performance Transparent Electrodes. *ACS Nano*, December 2013.

[97] A. Schlierf, P. Samorì, and V. Palermo. Graphene–organic composites for electronics: optical and electronic interactions in vacuum, liquids and thin solid films. *Journal of Materials Chemistry C*, 2(17):3129–3143, April 2014.

[98] Sukanta De, Paul J. King, Mustafa Lotya, Arlene O'Neill, Evelyn M. Doherty, Yenny Hernandez, Georg S. Duesberg, and Jonathan N. Coleman. Flexible, Transparent, Conducting Films of Randomly Stacked Graphene from Surfactant-Stabilized, Oxide-Free Graphene Dispersions. *Small*, 6(3):458–464, 2010.

[99] Umar Khan, Arlene O'Neill, Harshit Porwal, Peter May, Khalid Nawaz, and Jonathan N. Coleman. Size selection of dispersed, exfoliated graphene flakes by controlled centrifugation. *Carbon*, 50(2):470–475, February 2012.

[100] Zhengtang Luo, Ye Lu, Luke A. Somers, and A. T. Charlie Johnson. High yield preparation of macroscopic graphene oxide membranes. *J. Am. Chem. Soc.*, 131(3):898–899, January 2009.

[101] Cristina Gomez-Navarro, Jannik C. Meyer, Ravi S. Sundaram, Andrey Chuvilin, Simon Kurasch, Marko Burghard, Klaus Kern, and Ute Kaiser. Atomic Structure of Reduced Graphene Oxide. *Nano Letters*, 10(4):1144–1148, April 2010. WOS:000276557100008.

[102] M. Acik, G. Lee, C. Mattevi, M. Chhowalla, K. Cho, and Y. J. Chabal. Unusual infrared-absorption mechanism in thermally reduced graphene oxide. *Nature Materials*, 9:840–845, September 2010.

[103] H. Yang, Y. Hernandez, A. Schlierf, A. Felten, A. Eckmann, S. Johal, P. Louette, J. J. Pireaux, X. Feng, K. Mullen, V. Palermo, and C. Casiraghi. A simple method for graphene production based on exfoliation of graphite in water using 1-pyrenesulfonic acid sodium salt. *Carbon*, 53:357–365, March 2013.

[104] Yuan-Zhi Tan, Bo Yang, Khaled Parvez, Akimitsu Narita, Silvio Osella, David Beljonne, Xinliang Feng, and Klaus Müllen. Atomically precise edge chlorination of nanographenes and its application in graphene nanoribbons. *Nature Communications*, 4, November 2013.

[105] G. Giovannetti, P. A. Khomyakov, G. Brocks, V. M. Karpan, J. van den Brink, and P. J. Kelly. Doping graphene with metal contacts. *Phys. Rev. Lett.*, 101(2):026803, July 2008.

[106] W. N. Hansen and G. J. Hansen. Standard reference surfaces for work function measurements in air. *Surface science*, 481(1):172–184, 2001.

[107] Xiaochen Dong, Dongliang Fu, Wenjing Fang, Yumeng Shi, Peng Chen, and Lain-Jong Li. Doping Single-Layer Graphene with Aromatic Molecules. *Small*, 5(12):1422–1426, 2009.

[108] Young-Jun Yu, Yue Zhao, Sunmin Ryu, Louis E. Brus, Kwang S. Kim, and Philip Kim. Tuning the Graphene Work Function by Electric Field Effect. *Nano Letters*, 9(10):3430–3434, October 2009.

[109] Hiroki Ago, Thomas Kugler, Franco Cacialli, William R. Salaneck, Milo S. P. Shaffer, Alan H. Windle, and Richard H. Friend. Work Functions and Surface Functional Groups of Multiwall Carbon Nanotubes. *The Journal of Physical Chemistry B*, 103(38):8116–8121, September 1999.

[110] Ross A. Hatton, N. P. Blanchard, Li Wei Tan, Gianluca Latini, Franco Cacialli, and S. Ravi P. Silva. Oxidised carbon nanotubes as solution processable, high work function hole-extraction layers for organic solar cells. *Organic Electronics*, 10(3):388–395, May 2009.

[111] Xiao-Yan Zeng, Qi-Kai Zhang, Rong-Min Yu, and Can-Zhong Lu. A New Transparent Conductor: Silver Nanowire Film Buried at the Surface of a Transparent Polymer. *Advanced Materials*, 22(40):4484–4488, October 2010.

[112] Francesco Bausi, Andrea Schlierf, Emanuele Treossi, Matthias Georg Schwab, Vincenzo Palermo, and Franco Cacialli. Thermal treatment and chemical doping of semi-transparent graphene films. *Organic Electronics*, 18:53–60, March 2015.

[113] J. Ouyang, C.-W. Chu, F.-C. Chen, Q. Xu, and Y. Yang. High-Conductivity Poly(3,4-ethylenedioxythiophene):Poly(styrene sulfonate) Film and Its Application in Polymer Optoelectronic Devices. *Advanced Functional Materials*, 15(2):203–208, 2005.

[114] M. P. de Jong, L. J. van IJzendoorn, and M. J. A. de Voigt. Stability of the interface between indium-tin-oxide and poly(3,4-ethylenedioxythiophene)/poly(styrenesulfonate) in polymer light-emitting diodes. *Applied Physics Letters*, 77(14):2255–2257, October 2000.

[115] Michael S. Arnold, Samuel I. Stupp, and Mark C. Hersam. Enrichment of Single-Walled Carbon Nanotubes by Diameter in Density Gradients. *Nano Letters*, 5(4):713–718, April 2005.

[116] F. Bonaccorso, T. Hasan, P. H. Tan, C. Sciascia, G. Privitera, G. Di Marco, P. G. Gucciardi, and A. C. Ferrari. Density Gradient Ultracentrifugation of Nanotubes: Interplay of Bundling and Surfactants

Encapsulation. *The Journal of Physical Chemistry C*, 114(41):17267–17285, October 2010.

[117] G. Greczynski, M. Fahlman, and W.R. Salaneck. Electronic structure of hybrid interfaces of poly(9,9-dioctylfluorene). *Chemical Physics Letters*, 321(5-6):379–384, May 2000.

[118] Thomas M. Brown. *Electroabsorption Investigation of Polymer Light-Emitting Diodes with Efficient Electrodes.* PhD thesis, St. John's College, Cambridge, May 2001.

[119] B. W. D'Andrade, S. Datta, S. R. Forrest, P. Djurovich, E. Polikarpov, and M. E. Thompson. Relationship between the ionization and oxidation potentials of molecular organic semiconductors. *Organic electronics*, 6(1):11–20, 2005.

[120] Satoru Suzuki, Yoshio Watanabe, Yoshikazu Homma, Shin-ya Fukuba, Stefan Heun, and Andrea Locatelli. Work functions of individual single-walled carbon nanotubes. *Applied Physics Letters*, 85(1):127–129, July 2004.

[121] Bin Shan and Kyeongjae Cho. First Principles Study of Work Functions of Single Wall Carbon Nanotubes. *Physical Review Letters*, 94(23):236602, June 2005.

[122] Arun K. Manna and Swapan K. Pati. Doping single-walled carbon nanotubes through molecular charge-transfer: a theoretical study. *Nanoscale*, 2(7):1190–1195, July 2010.

184

[123] Iain A. Barlow, Theo Kreouzis, and David G. Lidzey. A polymer light-emitting diode as an optical communication light source. *Organic Electronics*, 8(5):621–624, October 2007. 4.

[124] Iain A. Barlow, Theo Kreouzis, and David G. Lidzey. High-speed electroluminescence modulation of a conjugated-polymer light emitting diode. *Applied Physics Letters*, 94(24):243301, June 2009. 7.

[125] T. Komine and M. Nakagawa. Integrated system of white LED visible-light communication and power-line communication. *IEEE Transactions on Consumer Electronics*, 49(1):71–79, February 2003.

[126] T. Komine and M. Nakagawa. Fundamental analysis for visible-light communication system using LED lights. *IEEE Transactions on Consumer Electronics*, 50(1):100–107, February 2004.

[127] D. O'brien, L. Zeng, Hoa Le-Minh, G. Faulkner, J.W. Walewski, and S. Randel. Visible light communications: Challenges and possibilities. In *IEEE 19th International Symposium on Personal, Indoor and Mobile Radio Communications, 2008. PIMRC 2008*, pages 1–5, September 2008.

[128] Cisco Visual Networking Index: Global Mobile Data Traffic Forecast Update 2014–2019 White Paper.

[129] A. Cailean, B. Cagneau, L. Chassagne, S. Topsu, Y. Alayli, and J.-M. Blosseville. Visible light communications: Application to cooperation between vehicles and road infrastructures. In *2012 IEEE Intelligent Vehicles Symposium (IV)*, pages 1055–1059, June 2012.

[130] T. van Woudenbergh, P. W. M. Blom, M. C. J. M. Vissenberg, and J. N. Huiberts. Temperature dependence of the charge injection in poly-dialkoxy-p-phenylene vinylene. *Applied Physics Letters*, 79(11):1697, 2001. 57.

[131] J. Campbell Scott. Metal-organic interface and charge injection in organic electronic devices. *Journal of Vacuum Science & Technology A: Vacuum, Surfaces, and Films*, 21(3):521, 2003.

[132] Sabine Bertho, Griet Janssen, Thomas J. Cleij, Bert Conings, Wouter Moons, Abay Gadisa, Jan D'Haen, Etienne Goovaerts, Laurence Lutsen, Jean Manca, and Dirk Vanderzande. Effect of temperature on the morphological and photovoltaic stability of bulk heterojunction polymer:fullerene solar cells. *Solar Energy Materials and Solar Cells*, 92(7):753–760, July 2008.

[133] P. W. M. Blom, M. J. M. de Jong, and J. J. M. Vleggaar. Electron and hole transport in poly(p-phenylenevinylene) devices. *Applied Physics Letters*, 68(23):3308, 1996. 444.

[134] Francesco Arca, Sandro F. Tedde, Maria Sramek, Julia Rauh, Paolo Lugli, and Oliver Hayden. Interface Trap States in Organic Photodiodes. *Scientific Reports*, 3, February 2013.

[135] A. Burton, E. Bentley, Hoa Le Minh, Z. Ghassemlooy, N. Aslam, and Shien-Kuei Liaw. Experimental demonstration of a 10base-T Ethernet visible light communications system using white phosphor light-emitting diodes. *IET Circuits, Devices Systems*, 8(4):322–330, July 2014.

[136] Rachel Jakubiak, Christopher J. Collison, Wai Chou Wan, Lewis J. Rothberg, and Bing R. Hsieh. Aggregation Quenching of Luminescence in Electroluminescent Conjugated Polymers. *The Journal of Physical Chemistry A*, 103(14):2394–2398, April 1999.

[137] Franco Cacialli, Joanne S. Wilson, Jasper J. Michels, Clement Daniel, Carlos Silva, Richard H. Friend, Nikolai Severin, Paolo Samorì, Jürgen P. Rabe, Michael J. O'Connell, Peter N. Taylor, and Harry L. Anderson. Cyclodextrin-threaded conjugated polyrotaxanes as insulated molecular wires with reduced interstrand interactions. *Nature Materials*, 1:160–164, October 2002.

[138] A.c. Morteani, A.s. Dhoot, J.-S. Kim, C. Silva, N.c. Greenham, C. Murphy, E. Moons, S. Ciná, J.h. Burroughes, and R.h. Friend. Barrier-Free Electron-Hole Capture in Polymer Blend Heterojunction Light-Emitting Diodes. *Advanced Materials*, 15(20):1708–1712, 2003.

[139] A. J. Mozer, P. Denk, M. C. Scharber, H. Neugebauer, N. S. Sariciftci, P. Wagner, L. Lutsen, D. Vanderzande, A. Kadashchuk, R. Staneva, and R. Resel. Novel Regiospecific MDMO-PPV Polymers with Improved Charge Transport Properties for Bulk Heterojunction Solar Cells. *Synthetic Metals*, 153(1–3):81–84, September 2005.

[140] Yuya Suzuki, Kazuhito Hashimoto, and Keisuke Tajima. Synthesis of Regioregular Poly(p-phenylenevinylene)s by Horner Reaction and Their Regioregularity Characterization. *Macromolecules*, 40(18):6521–6528, September 2007.

[141] H. Sirringhaus, P. J. Brown, R. H. Friend, M. M. Nielsen, K. Bech-gaard, B. M. W. Langeveld-Voss, A. J. H. Spiering, R. a. J. Janssen, E. W. Meijer, P. Herwig, and D. M. de Leeuw. Two-dimensional charge transport in self-organized, high-mobility conjugated polymers. *Nature*, 401(6754):685–688, October 1999.

[142] H. Sirringhaus, R. J. Wilson, R. H. Friend, M. Inbasekaran, W. Wu, E. P. Woo, M. Grell, and D. D. C. Bradley. Mobility enhancement in conjugated polymer field-effect transistors through chain alignment in a liquid-crystalline phase. *Applied Physics Letters*, 77(3):406–408, July 2000. 416.

[143] L. G. Kaake, P. F. Barbara, and X.-Y. Zhu. Intrinsic Charge Trapping in Organic and Polymeric Semiconductors: A Physical Chemistry Perspective. *The Journal of Physical Chemistry Letters*, 1(3):628–635, February 2010.

[144] F. Mahrt, H. Kurz, H. Bässler, E. O. Göbel, P. Thomas, and others. Received: February 6, 1998 Final version: April 15, 1998. *Opt. Lett*, 22:172, 1997. 57.

[145] V. I. Arkhipov, U. Wolf, and H. Bässler. Current injection from a metal to a disordered hopping system. II. Comparison between analytic theory and simulation. *Physical Review B*, 59(11):7514, 1999.

[146] U. Wolf, V. I. Arkhipov, and H. Bässler. Current injection from a metal to a disordered hopping system. I. Monte Carlo simulation. *Physical Review B*, 59(11):7507, 1999.

[147] Attila J. Mozer, Patrick Denk, Markus C. Scharber, Helmut Neuge-
bauer, N. Serdar Sariciftci, Pawel Wagner, Laurence Lutsen, and Dirk
Vanderzande. Novel Regiospecific MDMOPPV Copolymer with Im-
proved Charge Transport for Bulk Heterojunction Solar Cells. *The
Journal of Physical Chemistry B*, 108(17):5235–5242, April 2004. 64.

[148] Carrie E. Halkyard, Mary E. Rampey, Lioba Kloppenburg, Shannon L.
Studer-Martinez, and Uwe H. F. Bunz. Evidence of Aggregate Forma-
tion for 2,5-Dialkylpoly(p-phenyleneethynylenes) in Solution and Thin
Films. *Macromolecules*, 31(25):8655–8659, December 1998.

[149] Donal D. C. Bradley, Martin Grell, Xiao Long, Helen Mellor, Alan W.
Grice, Michael Inbasekaran, and Edmund P. Woo. Influence of aggre-
gation on the optical properties of a polyfluorene spie. volume 3145,
pages 254–259, SPIE 1997.

[150] Sergio Brovelli and Franco Cacialli. Optical and Electroluminescent
Properties of Conjugated Polyrotaxanes. *Small*, 6(24):2796–2820, De-
cember 2010.

[151] John M. Lupton, Peter Schouwink, Panagiotis E. Keivanidis, An-
drew C. Grimsdale, and Klaus Müllen. Influence of dendronization on
spectral diffusion and aggregation in conjugated polymers. *Advanced
Functional Materials*, 13(2):154–158, 2003. 46.

[152] Sebastian T. Hoffmann, Heinz Bässler, Jan-Moritz Koenen, Michael
Forster, Ullrich Scherf, Esther Scheler, Peter Strohriegl, and Anna
Köhler. Spectral diffusion in poly(para-phenylene)-type polymers with

different energetic disorder. *Physical Review B*, 81(11), March 2010. 14.

[153] J. W. Blatchford, S. W. Jessen, L.-B. Lin, T. L. Gustafson, D.-K. Fu, H.-L. Wang, T. M. Swager, A. G. MacDiarmid, and A. J. Epstein. Photoluminescence in pyridine-based polymers: Role of aggregates. *Physical Review B*, 54(13):9180, 1996. 101.

[154] Peter K. H. Ho, Ji-Seon Kim, Nir Tessler, and Richard H. Friend. Photoluminescence of poly(p-phenylenevinylene)-silica nanocomposites: Evidence for dual emission by Franck-Condon analysis. *The Journal of Chemical Physics*, 115(6):2709–2720, August 2001. 60.

[155] D. Braun, D. Moses, C. Zhang, and A. J. Heeger. Nanosecond transient electroluminescence from polymer light-emitting diodes. *Applied Physics Letters*, 61(26):3092–3094, December 1992.

[156] Arno Kraft, Andrew C. Grimsdale, and Andrew B. Holmes. Electroluminescent conjugated polymers: seeing polymers in a new light. *Angew. Chem. Int. End Engl*, 37:402–428, 1998. 2635.

[157] R. H. Friend, R. W. Gymer, A. B. Holmes, J. H. Burroughes, R. N. Marks, C. Taliani, D. D. C. Bradley, D. A. Dos Santos, J. L. Brèdas, M. Lögdlund, and W. R. Salaneck. Electroluminescence in conjugated polymers. *Nature*, 397(6715):121–128, January 1999. 4332.

[158] D. J. Pinner, R. H. Friend, and N. Tessler. Analysis of the turn-off dynamics in polymer light-emitting diodes. *Applied Physics Letters*, 76(9):1137, 2000.

[159] J. Wang, R. G. Sun, G. Yu, and A. J. Heeger. Fast pulsed electroluminescence from polymer light-emitting diodes. *Journal of Applied Physics*, 91(4):2417–2422, February 2002.

[160] J. W. Park, D. C. Shin, and S. H. Park. Large-area OLED lightings and their applications. *Semiconductor Science and Technology*, 26(3):034002, March 2011.

[161] Jong Woon Park and Jeong Hwan Kim. Enhancement in response speed of OLEDs for visible light communications. In *Opto-Electronics and Communications Conference (OECC), 2012 17th*, pages 613–614, July 2012.

[162] Xiong Gong. Polymer Light-Emitting Diodes (PLEDs): Devices and Materials. In Wenping Hu, editor, *Organic Optoelectronics*, pages 277–336. Wiley-VCH Verlag GmbH & Co. KGaA, 2013.

[163] Çetin Kiliç and Alex Zunger. Origins of coexistence of conductivity and transparency in sno$_2$. *Phys. Rev. Lett.*, 88(9):095501, February 2002.

[164] Penglei Li, Oliver Fenwick, Seyfullah Yilmaz, Dietrich Breusov, Daren J. Caruana, Sybille Allard, Ullrich Scherf, and Franco Cacialli. Dual functions of a novel low-gap polymer for near infra-red photovoltaics and light-emitting diodes. *Chemical Communications*, 47:8820, 2011.

[165] Ellen Moons. Conjugated polymer blends: linking film morphology to performance of light emitting diodes and photodiodes. *Journal of Physics: Condensed Matter*, 14(47):12235–12260, December 2002.

[166] A. C. Morteani, R. H. Friend, and C. Silva. Electronic processes at semiconductor polymer heterojunctions. *Organic Light Emitting Devices*, pages 35–94, 2006.

[167] O. Mryasov and A. Freeman. Electronic band structure of indium tin oxide and criteria for transparent conducting behavior. *Physical Review B*, 64(23), December 2001.

[168] P. Nemes-Incze, Z. Osváth, K. Kamarás, and L.P. Biró. Anomalies in thickness measurements of graphene and few layer graphite crystals by tapping mode atomic force microscopy. *Carbon*, 46(11):1435–1442, September 2008.

[169] R. Riehn, R. Stevenson, D. Richards, D.-J. Kang, M. Blamire, A. Downes, and F. Cacialli. Local probing of photocurrent and photoluminescence in a phase-separated conjugated-polymer blend by means of near-field excitation. *Advanced Functional Materials*, 16:469–476, March 2006.

[170] Michele Sessolo and Henk J. Bolink. Hybrid Organic-Inorganic light-emitting diodes. *Advanced Materials*, 23(16):1829–1845, 2011.

[171] F.M. Smit. Measurement of sheet resistivities with the four point probe. *Bell Syst. Tech. J.*, 37:711–717, 1958.